NTNU – Trondheim
Norwegian University of
Science and Technology

Exploring the Properties of a Modular Multilevel Converter Based HVDC Link

With Focus on Voltage Capability, Power System Relations, and Control System

Elisabeth Nøkleby Abildgaard

Master of Energy and Environmental Engineering
Submission date: June 2012
Supervisor: Marta Molinas, ELKRAFT
Co-supervisor: Øyvind Rui, Statnett

Norwegian University of Science and Technology
Department of Electric Power Engineering

Problem description

The modular multilevel converter (MMC) is a new and promising technology for HVDC. It can be used with high voltage and power levels and has the same advantages as classical Voltage Source Converters (VSCs) in making independent control of active and reactive power possible. The topology was introduced by Marquardt in 2003, and the development towards a commercial technology has been very fast. The first MMC based HVDC connection, the Trans Bay Cable, was commissioned in 2010.

The implementation of MMCs in the grid requires good models of the converter itself and research on the characteristics of grid connected MMCs. Specifically, the stability limits for the grid connected MMC are important to identify.

A case with a MMC connected to a stiff grid through a filter and a transformer is to be investigated. A simulation model of a MMC with half-bridge cells in the software PSCAD/EMTDC is to be used. The MMC is modelled by using a time-varying Thévenin equivalent to reduce the number of nodes in the model and hence make possible simulations of MMCs with a high number of submodules, without a large computational effort. The task consists of three main parts:

- Investigate the available voltage at the converter terminal, including description of the modulation strategy. The contribution from third harmonic distortion should be considered.

- Derive and analyse the network equations valid for the connection between the converter and the stiff grid using a phasor approach. Relationships between active power, reactive power and voltage levels should be investigated. Simulation results should be compared with the analytical results. Further, the analysis should be used to evaluate the stable operation range for the converter connected to the stiff grid.

- Continue on the work from the specialization project where a mathematical model for the MMC was developed and the design and tuning of a control system for the MMC was outlined using space-vectors. The control system should control either active power and reactive power or active power and the rms value of the voltage at the converter terminal. The control system should be implemented in the simulation model and verified.

Assignment given: 30. January 2012
Supervisor: Marta Molinas, ELKRAFT

Preface

Throughout the work with the master thesis, I have learned a lot about power systems, power electronics, control systems, and simulations, but most of all about troubleshooting. This work has led to a deep understanding of the converter and its properties, but also a knowledge of how to attack a large and complex task.

There is a number of people that has been of great importance to me during this work, and that I would like to thank. First of all I would like to thank my two supervisors, Marta Molinas and Øyvind Rui. Marta has helped me gain understanding and encouraged me to work towards scientific achievements. This has resulted in two conference participations; EPE '11 in Birmingham right after the start-up of my specialization project and Tecnoport 2012 in April where I presented a paper. These two experiences have been great inspirations and I would like to thank the department of Electric Power Engineering at NTNU for making it possible for me to attend. Øyvind has been an inspiration and a motivator with good ideas on how to develop the PSCAD model. The PSACD model provided by Statnett has been an important premise for the work. I would also like to address a thank to Jon Are Suul for helping me find the numerous errors that prevented my results from converging. His contribution has been important both for my progress and motivation.

Socially I would like to thank my office mates Åshild, Johannes, and Christian, both for making the days with hard work more cheerful and for good Sunday dinners. I would like to thank my father for by example showing me what it means to be a scientist and for giving support through e-mails and phone calls. Last, but not least, I would like to thank my mother for useful discussions on how to proceed from day to day, proofreading, and encouragement along the way.

Elisabeth N. Abildgaard
Trondheim, June 2012

Summary

The properties of a Modular Multilevel Converter (MMC) are investigated. This is a new and promising converter type for High Voltage Direct Current (HVDC) applications. A case with a MMC connected to a stiff grid through a filter and a transformer is analysed both theoretically and in simulations, with focus on three main topics.

The first topic is the available voltage at the converter terminal and modulation strategies. Theoretical evaluations are compared with simulation results. Two different methods are used to analytically investigate the relationship between modulation index and terminal voltage. The effect of third harmonic distortion is also considered. Simulations proved that the converter followed the theoretical modulation curve. Qualitative comparisons of theoretically developed voltage wave shapes with simulation results with different modulation indexes were successful, but quantitative comparisons proved challenging. Modulation with third harmonic distortion showed very convincing results in the simulations.

The second topic is the power equations valid for the case circuit. Relations between active power, reactive power, grid angle, and converter voltage were investigated. A phasor approach was used in the deduction of the theoretical formulas, and these formulas were verified by the simulation results. The grid angle range giving stable operation was defined by the angle stability limit for power systems. The ratio between the resistance and the inductance in the connection was found to have a large influence on the characteristics of the connection, for instance by defining the stable operation conditions. In the theoretical analysis the magnetizing effects of the transformer were disregarded. Simulations showed that this approximation was appropriate. A surprising simulation result was that the terminal voltage of the converter was depending on the grid angle. Further investigations are needed to identify the cause and compensate for this effect.

The third topic is the converter control system. The converter was modelled in the dq reference frame, and the model was used to derive and tune the control system. The control system was made with a cascaded structure, controlling either active and reactive power at the grid or active power at the gird and the rms value of the voltage at the converter terminal. The inner loops controlling the currents were tuned with modulus optimum to achieve fastness. The outer loops for power were tuned to be somewhat slower than the inner loops, while the outer loop for rms value was tuned with symmetric optimum. All the control loops were

successfully implemented into the simulation model. This shows that it is possible to control parameters at two different locations in the network at the same time. Simulations showed that it is possible to change the control mode between reactive power control and rms value control, without making the control system unstable. This demonstrated both successful decoupling and a robust control system.

Sammendrag

En modulær multinivåomformer (MMC) er en ny og lovende omformertype til bruk i høyspente likestrømsforbindelser. Egenskapene til en MMC er undersøkt teoretisk og med simuleringer ved et tilfelle der en MMC er tilkoblet et stivt nett gjennom et filter og en transformator. Det er fokusert på tre hovedtemaer.

Det første temaet er den tilgjengelige spenningen på omformerterminalen og moduleringsstrategier. Teoretiske vurderinger er sammenlignet med simuleringsresultater. Det ble bruk to forskjellige analytiske metoder for å undersøke forholdet mellom moduleringsindeks og terminalspenning. Virkningen av tredjeharmonisk distorsjon er undersøkt. Kvalitative sammenligninger av teoretisk utviklede spenningsbølgeformer og simuleringsresultater med forskjellige modulasjonsindekser var vellykkede, men kvantitative sammenligninger viste seg å være vanskelige. Modulasjon med tredjeharmonisk distorsjon viste gode resultater i simuleringene.

Det andre temaet er effektligninger for den aktuelle kretsen. Sammenhenger mellom aktiv effekt, reaktiv effekt, nettvinkel og omformerspenning ble undersøkt. Et viserdiagram ble brukt som utgangspunkt for utledningen av de teoretiske formlene. Formlene ble bekreftet gjennom simuleringer. Nettvinkelintervallet som gir stabil drift ble definert ut fra vinkelstabilitetsbegrensningen for kraftsystemer. Forholdet mellom resistans og induktans i tilkoblingen viste seg å ha stor innvirkning på tilkoblingens egenskaper, for eksempel ved å avgjøre nettvinklene som gir stabil drift. I den teoretiske analysen ble magnetiseringseffektene i transformatoren sett bort fra. Simuleringene viste at denne modellen var en god tilnærming. Et overraskende resultat var at omformerens terminalspenning varierte med nettvinkelen. Videre undersøkelser er nødvendig for å finne årsaken til og om mulig kompensere for denne effekten.

Det tredje temaet er omformerens kontrollsystem. Omformeren ble modellert i dq-referanserammen, og modellen ble brukt til å utlede og tune kontrollsystemet. Kontrollsystemet ble laget med en kaskadestruktur, der aktiv og reaktiv effekt i nettet eller aktiv effekt i nettet og rms-verdien til terminalspenningen kan kontrolleres. De indre sløyfene som kontrollerer strømmene ble tunet med modulus optimum for å oppnå hurtighet. De ytre sløyfene for effekt ble tunet til å være noe langsommere enn de indre sløyfene, mens den ytre sløyfen for rms-verdi ble tunet med symmetrisk optimum. Alle komtrollsløyfene ble implementert i simuleringsmodellen og tester viste at de fungerte godt. Dette viser at det er mulig å kontrollere parametere på to forskjellige steder i nettverket. Simuleringer viste også at det er mulig å endre

kontrollmetoden mellom reaktiv effektkontroll og rms-verdikontroll underveis, uten at kontrollsystemet ble ustabilt. Dette indikerer at kontrollsystemet er robust og har en vellykket avkobling mellom d-aksen og q-aksen.

Contents

List of Figures

List of Tables

Terms Used in the Text

Subscripts and Superscripts Used in the Text

d	Real axis of the Park transformation
q	Imaginary axis of the Park transformation
abc	Phases of a three-phase system
0	Zero sequence component
$base$	Base value
pu	Per unit value
rms	Root mean square value
LL	Line to line voltage
$p-n$	Phase to neutral voltage
ref	Reference value
err	Error signal
*	Complex conjugate

Parameters Used in the Text

ϕ	Current angle
θ	Voltage space vector angle
δ	Grid angle
σ	Angle between the reference voltage and the grid voltage vector
U_D	DC voltage
f_{sw}	Switching frequency
m	Modulation index
ω	Angular frequency (rad/s)
T_a	Time constant converter
K_p	Proportional controller constant
T_i	Controller integration time
P	Active power
Q	Reactive power
S	Apparent power
E	Converter terminal voltage
V	Stiff grid voltage
e_V	Inner alternating converter voltage
i	Current from the converter to the grid

List of Abbreviations

AC	Alternating Current
DC	Direct Current
HVDC	High Voltage Direct Current
IGBT	Insulated Gate Bipolar Transistor
LCC	Line Commutated Converter
MMC	Modular Multilevel Converter
PI	Proportional Integrator
PLL	Phase Locked Loop
pu	Per Unit
PWM	Pulse Width Modulation
rms	Root Mean Square
THD	Total Harmonic Distortion
VSC	Voltage Source Converter

Chapter 1

Introduction

1.1 Background

With implementation of new renewable energy production, High Voltage Direct Current (HVDC) is more relevant than ever. More stochastic energy production calls for solutions that can transport power from areas with high generation to areas with lower generation. Offshore wind farms far from the coast require HVDC transmission to the shore and compact and reliable converter technology with large power capability. Connecting the converter to a DC grid should be feasible and the converter should be able to handle fault situations. To gain compactness, the need for filters should be minimized. The emerging topology Modular Multilevel Converter (MMC) might address these aims.

HVDC transmission through sea cables is used to connect the Norwegian grid with the grid at the European continent. The three Skagerrak cables connect Norway and Denmark, and the NorNed cable connects Norway and the Netherlands. This is beneficial as the Norwegian power production is mainly hydropower and therefore highly controllable, while the thermal power and wind power production at the continent is less controllable. At the same time, the Norwegian hydropower system has limited energy capacity, so cooperation with other countries is important to ensure enough electrical energy in years with limited rainfall. The controllability of the hydropower makes it possible to increase the wind power penetration in the network as energy balancing can be done in a fast and efficient way. A new interconnection between Norway and Denmark, Skagerrak 4, is to be commissioned in 2014 [1, 2]. The converters used in this project will be MMCs. This is the first time that a VSC type of converter is used at such a high voltage level. The converter will contribute in the power system stabilization in the Norwegian grid.

The MMC is a new and promising converter that can be used with high voltage and power levels. It has the same advantages as Voltage Source Converters (VSCs) in making independent control of active and reactive power possible, but the topology is utilized without series connections of Insulated Gate Bipolar Transistors (IGBTs). The MMC is the only multilevel converter commercially available

for HVDC applications. The first MMC based HVDC connection, the Trans Bay Cable [3], was commissioned in 2010. As the topology was introduced by Marquardt [4] in 2003, the development towards a commercial technology has been very fast.

The success of this novel topology makes it an important research object as its characteristics should be well known when it is implemented in the power system. This requires good models of the converter itself, but also knowledge of how the converter behaves when connected to a grid. Successful operation of the converter is depending on a well-functioning control system. It is important to explore which combinations of control parameters that can be used. Regarding both the control system and the grid connection, stability is a key objective. The motivation for this thesis is therefore an attempt to achieve such knowledge and document the results. This is done using analytical evaluations and a PSCAD model provided by Statnett.

Large parts of the material concerning converter technologies, modelling of the MMC, and the control system structure is based on the study performed in the specialization project [5]. When necessary to achieve completeness in this thesis, parts of the work presented in the specialization project is included.

1.2 The Case

Both in the theoretical parts and in the simulations a MMC connected to a stiff grid is investigated. The case circuit used is presented here. All circuit parameters are given in Appendix B.

Figure 1.1 shows the converter with a fixed DC voltage on one side and a gird connection on the AC side. Between the AC terminal of the converter and the stiff grid is a filter consisting of a resistance and an inductance, and transformer later modelled as an inductance. The high voltage side of the transformer is on the grid side. The converter terminal voltage, denoted E, is leading the stiff grid voltage, denoted V, with an angle δ, and the current going from the converter to the stiff grid is lagging the stiff grid with an angle ϕ. The reference direction for power is power delivered from the converter.

1.3 Outline

The work presented in this thesis can be divided into two main parts. The first part consists of analytical evaluations of the converter and case circuit. The second part consists of simulation results. The two parts are tightly connected as they investigate the same topics and hence deliver results that can advantageously be compared. The investigated topics are:

- Converter terminal voltage range and modulation strategies
- Relationships between active and reactive power, grid angle, and voltage level, including stability limitations

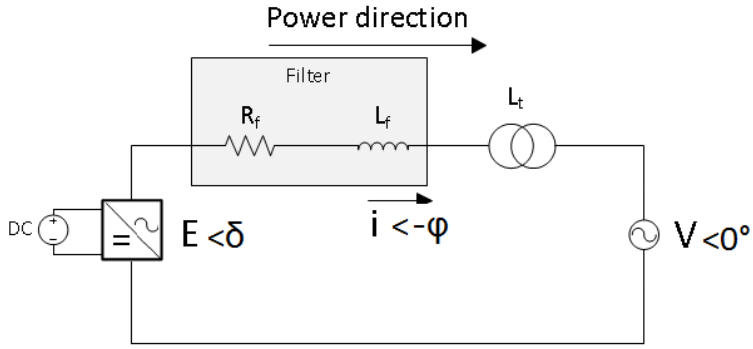

Figure 1.1: The case circuit

- Converter control system with tuning, implementation, and testing

Chapter 2 gives a background for understanding the rest of the work presented, introducing the most important definitions and methods used. It also introduces different converter technologies and the MMC in particular. The operation principle of the MMC is explained and the PSCAD model described.

The converter terminal voltage is examined in Chapter 3. This is done by considering modulation strategies and the resulting voltage. Both an analytical method and a semi-analytical method utilizing curve fitting are used. The effect of third harmonic distortion is investigated.

In Chapter 4 the power equations valid for the case circuit are presented and evaluated. The maximal power transfer is calculated by optimizing the grid angle and the inductance value. Finally the stability limits for the case circuit are investigated.

The control system is introduced in Chapter 5. To make it possible to develop and tune a control system properly, a mathematical model for the process that is to be controlled must exist. Chapter 5 therefore starts with the development of the mathematical model for the MMC. The control system is made with a cascaded structure consisting of inner loops for current control and outer loops for power and voltage control. The loops are derived and tuned, and the block diagrams are shown.

Chapter 6 shows the simulations corresponding to the analysis done in Chapter 3. The available voltage range for the converter model is shown in addition to voltage curves and rms values. The harmonic distortion for different modulation indexes is stated.

In Chapter 7 the power range for the simulation model of the converter is investigated. Simulations with different gird angle values are presented to illustrate how the different parameters depend on this angle. In addition, the effects of the transformer are investigated to verify that the simplified transformer model used in Chapter 4 is a good approximation to the simulation model.

The result of implementing the control system described in Chapter 5 is shown in Chapter 8. The resulting model is tested, and graphs showing the effectiveness of the control system are presented.

Finally the strengths, limitations, and consequences of the work are discussed in Chapter 9. This chapter is followed by a conclusion and suggestions for further work.

Chapter 2

Background and Theory

2.1 Park's Transformation

The stationary *abc* system is transformed into the rotating dq system in the control system development. The dq reference frame is rotating at synchronous speed ω with respect to the *abc* reference frame. The position of the d axis with respect to the a axis is given by $\theta = \omega t$. The reference frames are shown in Figure 2.1. The rotation matrix for the transformation is given in Appendix A.

The expressions for active and reactive power in the dq system are:

$$P = \frac{3}{2}(v_d i_d + v_q i_q) \tag{2.1}$$

$$Q = \frac{3}{2}(v_d i_q - v_q i_d) \tag{2.2}$$

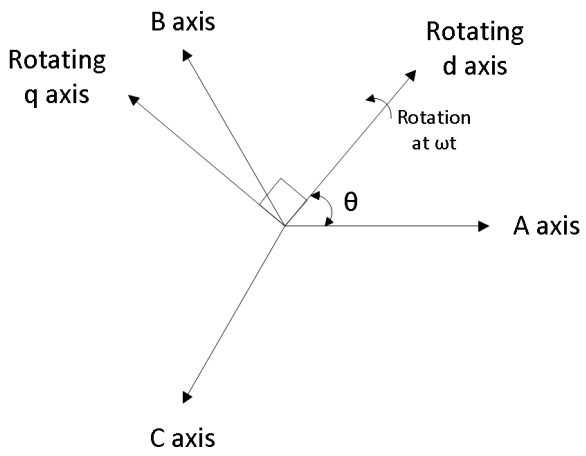

Figure 2.1: The stationary *abc* system and the rotating dq system

As the grid voltage vector is aligned with the d axis, the q axis voltage must be zero. Equations 2.1 and 2.2 can therefore be simplified:

$$P = \frac{3}{2} v_d i_d \tag{2.3}$$

$$Q = \frac{3}{2} v_d i_q \tag{2.4}$$

It can be seen from Equations 2.3 and 2.4 that active and reactive power can be controlled independently with this alignment.

The relation to the rms value is:

$$\sqrt{\frac{v_d^2 + v_q^2}{2}} = V_{\text{rms}} \tag{2.5}$$

All deductions are given in Appendix A.

2.2 Per Unit System

The definition of the pu system is done as in Kundur [6].

General Parameters

$S_{\text{base}} = 600$ MVA - rated power
$\omega_{\text{base}} = 2\pi f \frac{\text{rad}}{\text{s}}$ - base frequency, f=50Hz

Low Voltage Side of the Transformer

$V_{\text{base}} = \sqrt{\frac{2}{3}} 300 \text{ kV} = 244.95 \text{ kV}$ - nominal peak phase voltage
$I_{\text{base}} = \frac{2}{3} \frac{S_{\text{base}}}{V_{\text{base}}} = \frac{2}{3} \frac{600\text{MVA}}{\sqrt{\frac{2}{3}} 300\text{kV}} = \sqrt{\frac{2}{3}} 2000\text{A} = 1632.99 \text{ A}$ - nominal peak current
$Z_{\text{base}} = \frac{V_{\text{base}}}{I_{\text{base}}} = \frac{\sqrt{\frac{2}{3}} 300\text{kV}}{\sqrt{\frac{2}{3}} 2000\text{A}} = 150\Omega$ - base impedance
$L_{\text{base}} = \frac{Z_{\text{base}}}{\omega_{\text{base}}} = \frac{150\Omega}{2\pi f} = 0.4775 \text{ H}$ - base inductance
$C_{\text{base}} = \frac{\omega_{\text{base}}}{Z_{\text{base}}} = \frac{2\pi f}{150\Omega} = 2.094 \text{ F}$ - base capacitance

High Voltage Side of the Transformer

$V_{\text{base}} = \sqrt{\frac{2}{3}} 400 \text{ kV} = 326.60 \text{ kV}$ - nominal peak phase voltage
$I_{\text{base}} = \frac{2}{3} \frac{S_{\text{base}}}{V_{\text{base}}} = \frac{2}{3} \frac{600\text{MVA}}{\sqrt{\frac{2}{3}} 400\text{kV}} = \sqrt{\frac{2}{3}} 1500\text{A} = 1224.74 \text{ A}$ - nominal peak current
$Z_{\text{base}} = \frac{V_{\text{base}}}{I_{\text{base}}} = \frac{\sqrt{\frac{2}{3}} 400\text{kV}}{\sqrt{\frac{2}{3}} 1500\text{A}} = 266.67\Omega$ - base impedance
$L_{\text{base}} = \frac{Z_{\text{base}}}{\omega_{\text{base}}} = \frac{266.67\Omega}{2\pi f} = 0.8488 \text{ H}$ - base inductance
$C_{\text{base}} = \frac{\omega_{\text{base}}}{Z_{\text{base}}} = \frac{2\pi f}{266.67\Omega} = 1.178 \text{ F}$ - base capacitance

2.3 Control Theory

2.3.1 The PI Controller

The PI controller is a proportional and integral controller [7]. The aim of the integration term is to have amplification close to infinite at low frequencies and in this way to obtain zero steady-state deviation. At high frequencies the controller is close to a purely proportional controller.

The transfer function for the PI controller is:

$$H_r(s) = K_p\big(1 + \frac{1}{T_i s}\big) \tag{2.6}$$

where k_p is the proportional constant and T_i is the integration time.

To enable the use of the PI controller, the reference signal must be constant, to make it possible to obtain zero steady-state deviation. When the three-phase AC components are transformed into the dq reference frame, they become constant signals. This is one of the reasons why the dq transformation is used in the control system.

2.3.2 Feed-Forward

The aim of feed-forward is to generate a change in the control signal so that the control signal will suppress the effect of a disturbance on the process and thus reduce the effect of the disturbance on the output signal [7]. Feed-forward is most important when the impact of the feedback is reduced due to delays in the process.

In Figure 2.2 a general disturbance v is affecting the output signal y. Assuming that the feedback loop is disabled, that is $H_r(s) = 0$, the output signal y as a function of the disturbance is:

$$y(s) = H_{u2}(s)(H_{u1}(s)H_f(s) + 1)v(s) \tag{2.7}$$

The ideal feed-forward, $H_{fi}(s)$, is achieved if the expression in Equation 2.7 equals zero [7]. This gives:

$$H_{fi}(s) = -\frac{1}{H_{u1}(s)} \tag{2.8}$$

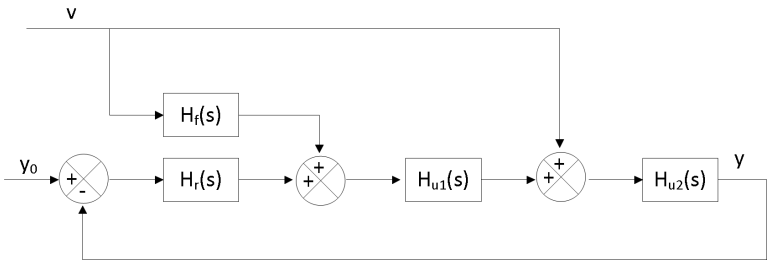

Figure 2.2: A general feedback system with feed-forward from the disturbance

The static feed-forward is defined as $H_f(0)$ and shows to which degree a constant disturbance will be suppressed.

The feed-forward ratio is defined as [7]:

$$L(s) = \frac{y(s)_{with}}{y(s)_{without}} = H_f(s)H_{u1}(s) + 1 \tag{2.9}$$

where $y(s)_{with}$ is $y(s)$ as a function of $v(s)$ with feed-forward and $y(s)_{without}$ is $y(s)$ as a function of $v(s)$ without feed-forward, that is $H_f(s) = 0$.

When the feed-forward is combined with a feedback, the total ability to suppress the disturbance in the system is given by the product of the feed-forward ratio and the regulation ratio. The regulation ratio is given as [7]:

$$N(s) = \frac{1}{1 + H_0(s)} \tag{2.10}$$

where $H_0(s)$ is the open loop transfer function.

The feed-forward should ensure that $|L(s)| < 1$ when $N(s) \approx 1$

2.3.3 Tuning

Modulus Optimum

The objective of modulus optimum is to maintain the magnitude response curve as flat and as close to unity for as large bandwidth as possible for a given system and controller combination [8]. This gives a loop with a fast response [9]. The tuning is done by making the zero in the PI controller cancel the pole from the largest time constant in the system transfer function. When using modulus optimum, all disturbances and feed-forwards can be neglected. This enables independent tuning of the d and q axis loops.

If the transfer function of the process can be written:

$$H_p(s) = \frac{K}{(1 + T_1 s)(1 + T_2 s)} \tag{2.11}$$

where $T_1 > T_2$, then the PI controller with transfer function:

$$H_c(s) = k_p \frac{1 + T_i S}{T_i s} \tag{2.12}$$

should have $T_i = T_1$. The required value for k_p is given as $k_p = \frac{T_1}{2T_2K}$ [8].

Symmetric Optimum

The objective of symmetric optimum is to give the system robustness against disturbances and to maximize the phase margin [9]. When tuning with symmetric optimum, the open loop transfer function is used and all disturbances and feed-forwards can be disregard. This enables independent tuning of the d and q axis loops.

If the transfer function of the process can be written:

$$H_p(s) = \frac{K}{T_1 s(1 + T_2 s)} \tag{2.13}$$

Then the PI controller with transfer function:

$$H_c(s) = k_p \frac{1 + T_i S}{T_i s} \tag{2.14}$$

should have $T_i = 4T_2$. The required value for k_p is given as $k_p = \frac{T_1}{2KT_2}$ [8].

2.4 Converter Technologies for HVDC

The Line Commutated Converter (LCC) was the first converter technology to be used in HVDC applications. In the late 1990s the Voltage Source Converter (VSC) was introduced for high voltage levels. The first Modular Multilevel Converter (MMC) HVDC scheme was commissioned in 2010. The MMC technology can be considered a further development of the classical VSC technology. The LCC technology and the VSC/MMC technology have different applications as the ratings and the characteristics of the technologies differ. The LCC can be built with very high ratings, but the VSC/MMC has better controllability and grid stabilizing ability. A trend in converter development is to avoid series and parallel connections used to increase the voltage and current capability and instead focus on modular structures. The aims are to get both higher voltage and current capability without series connections, reduce the need for filters, and limit the losses.

2.4.1 LCC

The thyristor based LCCs were introduced during the 1970s. LCC is still the converter that can be built with highest power rating and hence is the best solution for bulk power transmission. Another advantage of LCC is the low losses, typically 0.7 % per converter [10]. The largest disadvantage is that both the inverter and the rectifier absorb a varying amount of reactive power from the grid, and accordingly adjustable reactive compensation is needed [11]. The LCC will also need an AC voltage source at each terminal to be able to succeed with commutation. In order to minimize the harmonic content, the standard LCC design is made with two 6-pulse bridges in parallel on the AC side and in series on the DC side. The two bridges are phase shifted 30 degrees on the AC side, using transformers [12].

2.4.2 VSC

The classical VSC utilizing Insulated Gate Bipolar Transistors (IGBTs) for HVDC applications was introduced in 1997 by the ABB concept HVDC Light [13]. Classical VSCs for HVDC applications are based on two-level or three-level converters [13]. With this concept it is not possible to adjust the voltage magnitude at AC terminals, but the voltage can be $\pm V$ with two-level or $\pm V$ or zero voltage with

three-level VSCs [11]. Pulse Width Modulation (PWM) is used to approximate the desired voltage waveform. The difference between the desired and implemented waveform is an unwanted distortion which has to be filtered [11]. Because IGBTs have limited voltage blocking capability, they need to be connected in series in two-level and three-level VSCs [13]. In order to limit the voltage across each semiconductor, series connected IGBTs must be switched absolutely simultaneously. This requires sophisticated gate drive circuits to enforce voltage sharing under all conditions [14].

2.4.3 Comparison of LCC and VSC

With VSCs, both active power flow and reactive power flow can be controlled, independently [11], and accordingly no reactive compensation is needed. A VSC station is therefore more compact than a LCC station as the harmonic filters are smaller and no switch yards and capacitor banks are needed [13]. Other advantages with the VSC are that the converter can be connected to weak systems and even to networks lacking generation [13] and it has black start capability [12], meaning that the converter can be used to energize the grid after a blackout. As no phase shift is needed, the VSC can use ordinary transformers. A disadvantage is that the VSC has larger losses than LCC, typically 1.7 % per converter [10]. Using LCC, the current direction is fixed and power reversal is done by changing the voltage polarity. With VSCs power reversal is done by changing of the current direction. This makes the VSC technology more suitable for DC grid applications [12]. Cross-linked polyethylene cables can be used with VSCs, but cannot handle the stress from a polarity change. Cross-linked polyethylene cables are less costly, lighter, and smaller in diameter than traditional mass impregnated cables and therefore advantageous [15]. The power reversal with VSCs can be done gradually because the full range of active power is available. Even zero active power can be combined with a positive or negative reactive power. Because both active and reactive power can obtain positive and negative values, the converter is said operate in all four quadrants of the PQ plane [9]. LCCs normally have a minimum active power output 5% below rated power [16]. This makes VSCs more favourable for power transmission with varying power e.g. power generated from a wind farm. But an advantage with LCC HVDC is that DC pole to pole short circuit faults can be cleared in the converter station, because if no firing pulses are given, the thyristors will block. This is not the case with classical VSC HVDC as the freewheeling diodes can conduct even if the IGBTs are switched off. In most cases the fault currents must be suppressed by opening the AC breaker feeding the converter [14]. Hence, the absence of a reliable DC breaker capable of isolating DC faults restricts the practical application of VSC HVDC.

2.4.4 MMC

In 2010 the first Siemens HVDC PLUS system was commissioned, a multilevel VSC technology called MMC [11]. At the same time, ABB updated their HVDC Light product to make use of approximately the same technology [13]. MMCs

are built up by a number of identical, but individually controllable submodules, see Figure 2.3. The submodules in the MMC can either be two-level half-bridge converters, each capable of producing +V or zero voltage, or two-level full-bridge converters, producing $\pm V$ or zero voltage [14]. This means that the converter acts as a controllable voltage source with a high number of possible discrete voltage steps. The multilevel topology prevents generation of any major harmonic content [13].

The MMC is a scalable technology. The voltage level determines the number of submodules needed, and the technology can be used up to the highest transmission voltages [17]. The configuration is without series connection of semiconductor switches, and hence problems with simultaneous switching are irrelevant. Losses are lower than for two-level and three-level VSCs, about 1 % per converter [13]. The low losses are obtained by low switching frequency in each submodule and low voltage across each switch [17]. However, as the submodules are switched at different points in time, the effective switching frequency of the converter is high, giving a low harmonic distortion [13]. An advantage with MMCs compared to classical VSCs is that the $\frac{\mathrm{d}v}{\mathrm{d}t}$ is reduced as the voltage steps at the AC terminals are smaller. This enables the use of transformers with lower insulation requirement

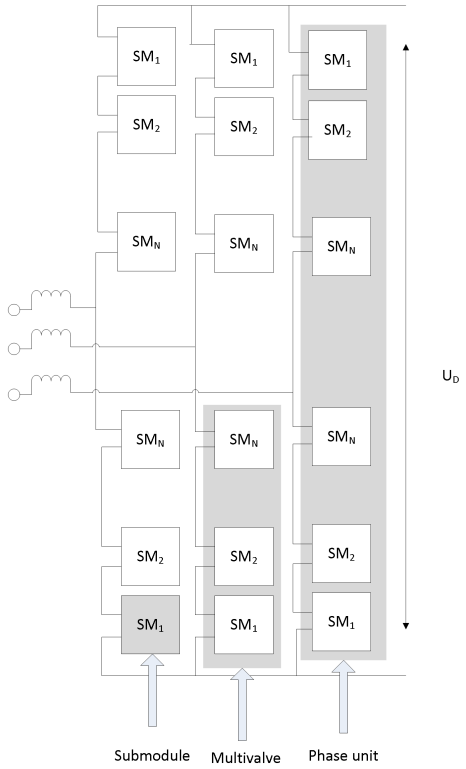

Figure 2.3: The MMC structure

[18]. Compared to LCC the MMC uses ordinary transformers, no phase shift is needed.

A MMC with two-level half-bridge submodules requires twice the number of IGBTs of to a two-level VSC with the same rating. For a MMC with two-level full-bridge submodules, the need for IGBTs is twice as high as with half-bridge submodules [14]. The MMC has no DC link capacitance, but one capacitor in each submodule. These capacitors require both large voltage capacity as the fundamental current is passing through them and large capacitance to avoid energy ripple. The result of many semiconductor switches and capacitors with high ratings is a heavy and bulky circuit, giving a converter that is less compact than the classical VSC, but still more compact than the LCC [14]. As the number of semiconductors is an important factor for the converter footprint, the full-bridge MMC is more bulky than the half-bridge MMC.

The MMC with two-level half-bridges cannot block fault currents during a DC pole to pole fault. As with the classical VSC, the freewheeling diodes can conduct fault current from the AC side and into the fault. With two-level full-bridge submodules the MMC is capable of suppressing the fault current, and therefore no AC breaker opening is needed [14]. By closing the switches in two equally directed valves, the current is trapped inside the submodule and no AC side current is fed into the DC fault. It can be discussed whether this advantage is large enough to defend the increased number of semiconductors. As both vendors delivering MMC solutions uses two-level half-bridges [13, 11], only this solution will be described in the following.

2.4.5 State of the Art

Planned installations in 2011 shows that LCC HVDC can be built with 7200 MW and ±800 kV (the Jinping-Sunan project), while MMC projects are planned with 1000 MW and ±320 kV (the INELFE project) [19, 20].

Capability defining products on the marked are ultra HVDC (UHVDC) converters using LCCs and MMCs, available as Siemens' HVDC PLUS and ABB's HVDC light. UHVDC is delivered with ±800 kV [21] and 8000 MW [22]. ABB describes the uppers range for HVDC Light as ±500 kV and 1200 MW [23].

2.4.6 Other Converter Technologies

A number of other possible converter topologies has been proposed, such as other multilevel converters and the hybrid converters. Among the most important multilevel topologies are the neutral-point clamped converter [24], the diode-clamped multilevel converter [25], and flying capacitor multilevel converter [26], in addition to the MMC. Hybrid converters can be constructed by combining the advantages of classical VSC and MMC [14]. The aim is to achieve a better output signal than with classical VSC combined with using fewer semiconductor devices than with MMCs. Small MMCs can be used as active filters or wave shaping circuits. Connections can be done in different manners. The MMC is the only one of these topologies used in commissioned HVDC projects.

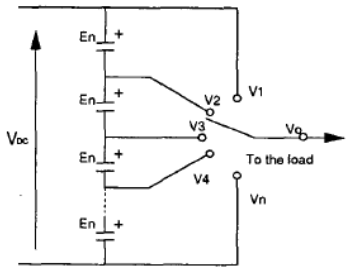

Figure 2.4: Single-pole multiple-throw switch

Multilevel converters are described by the number of different output voltage they can generate, n. For instance n=3 indicates that the converter can generate $\pm V$ in addition to zero voltage. The main idea can often be described by a single-pole multiple-throw switch (see Figure 2.4). As the figure indicates, different voltage values can be obtained at the output by changing the switch position. Most multilevel converters use capacitors to achieve different voltage levels. In many topologies capacitor voltage balancing is challenging.

2.5 The Operation Principle of the MMC

In a three-phase MMC, each of the phase units consists of two multivalves, and each multivalve consists of N submodules connected in series (Figure 2.3) [17]. With a DC voltage of $\pm$320 kV N=38 is typically required [13]. The half-bridge submodule consists of two valves (T_1 and T_2) and a capacitor, see Figure 2.5. The valves are made up of an IGBT and a freewheeling diode in antiparallel. In normal operation, only one of the valves is switched on at a given instant in time. Depending on the current direction the capacitor can charge or discharge [17].

When only one IBGT is switched on, either that IGBT or the freewheeling diode in the same valve will conduct, depending on the current direction, and for this reason it makes sense to define a valve as on, indicating that either the IGBT or the diode is conducting [17].

Three possible switching states can be defined [13]:

- In the ON or *inserted* state T_1 is on, and T_2 is off. The submodule output voltage, V_{SM}, equals the capacitor voltage, V_C, and the capacitor charges if the multivalve current, I_{SM}, is positive and discharges otherwise.
- In the OFF or *bypassed* state T_2 is on, and T_1 is off. The submodule output voltage is zero and the capacitor voltage is constant, i.e. the capacitor will not charge nor discharge.
- In the *blocked* state, both valves are off, and the current can only conduct through the freewheeling diodes. The capacitor will charge if the current is positive, but ideally it cannot discharge.

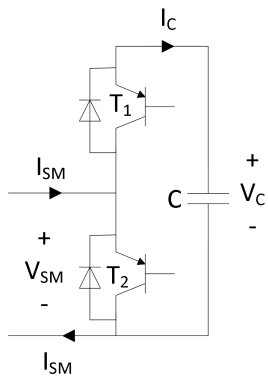

Figure 2.5: The submodule circuit

The blocking voltage in each phase unit is twice the DC voltage. This can be explained from the situation when all the submodules in the upper multivalve are bypassed, giving a phase voltage equal to the half DC voltage. The lower multivalve must be able to block the voltage across itself, i.e. the DC voltage. The result is that each switch must be able to block the DC voltage, U_D, divided by the number of submodules in each multivalve, N, giving $V_{block} = \frac{U_D}{N}$. The capacitors in the lower multivalve will also share the DC voltage and must be dimensioned in the same way as the IGBTs. Considering the same case and a negative I_{SM} relative to the reference direction in Figure 2.5, each IGBT in the upper valve must be able to block the voltage across the capacitor in the same submodule. This is one of the reasons why capacitor voltage balancing is important. From this reasoning it can be concluded that the blocking voltage in each of the 4N switches in a phase unit must be at least $\frac{U_D}{N}$. If the voltages are unevenly distributed, the requirement will increase.

The sum of inserted voltages in one multivalve should always have half the DC voltage as average value in order to get a phase output with zero DC offset. The sum may take any value between zero and the DC voltage, but in the ideal, perfectly balanced case the sum of the voltages in the inserted submodules in a phase should equal the DC voltage. Also the sum of capacitor voltages in each multivalve should equal the DC voltage. The sum of the inserted voltages is kept constant because inserting one submodule in one multivalve is done simultaneously with bypassing one submodule in the other multivalve of the same phase.

2.5.1 Mathematical Modelling of the MMC

Using thyristors, the only controllable parameter is the firing angle, and therefore modelling of the LCC is quite straight forward. For VSC schemes using series connected IGBTs, all the series connected switches are either conducting or blocking. This is utilized in the modelling by defining the share of time the switches are on, the duty ratio [27].

This method cannot be applied for MMCs as some submodules in the multivalve are inserted while others are bypassed. In the model presented in section 5.1.1 this is solved using dynamic insertion indexes describing the share of submodules that is inserted at every instant.

As for many other multilevel topologies, capacitor voltage balancing is a challenge with the MMC. The switching scheme must be implemented in such a way that the capacitor voltages are kept in the correct range. In the PSCAD model presented in section 2.6 this is done based on measurements of the capacitor voltages and the knowledge of whether a capacitor will charge or discharge given the present current direction [17].

2.6 The PSCAD Model

The PSCAD model is a model of a generic MMC. The firing pulses can be generated in two different ways, one corresponding to the control method used in HVDC PLUS and one corresponding to the method used in HVDC Light. The model is however not necessarily representative for these two topologies. Only the HVDC Light method for generation of firing pulses has been used in the simulations in this thesis.

As figure 2.6 shows, the model consists of three parts: the upper level control system, the lower level control system and the Thévenin equivalent. The upper level control system uses a dq reference frame to control the active power and the reactive power or rms value of the voltage at the converter terminal. The lower level control contains a capacitor voltage sorting algorithm and determines the firing pulses. The Thévenin equivalent represents the physical MMC and is developed to enable fast simulations of MMCs with many submodules.

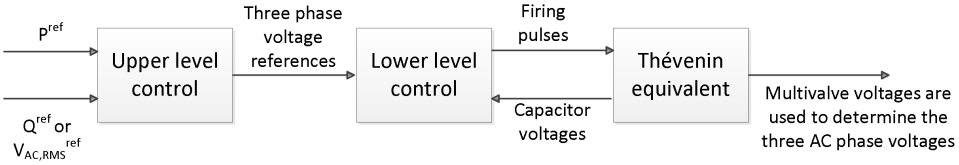

Figure 2.6: The three blocks in the PSCAD model

2.6.1 The Upper Level Control System

Into the upper level control system go references for active power and either reactive power or rms value. The upper level control system calculates three phase voltage references and feeds them into the lower level control system. A more detailed description of the upper level control system including control loops, is given in Chapter 5.

2.6.2 The Lower Level Control System

The lower level control system determines which submodules to insert and bypass. The number to insert or bypass is found by comparing the three phase voltage references with carrier waves. The selection of submodules is done based on capacitor voltage measurements delivered from the Thévenin equivalent. When the multivalve current direction is known, it can be predicted whether the capacitor will charge or discharge when inserted. This information is used to insert or bypass the submodules closest to the range limits and in this way to keep the voltages balanced. A positive current in Figure 2.5 will charge the inserted capacitors, while a negative current will discharge the capacitors. Examples on insertion curves made from reference voltage waves and carrier voltage waves are shown in section 3.1.1. The examples correspond to the phase shifted PWM control that is used in HVDC Light [28].

2.6.3 The Thévenin Equivalent

The Thévenin equivalents calculate the multivalve voltage using multivalve currents and resistance values. There is one Thévenin equivalent for each multivalve. The reason for using the Thévenin equivalent is that it reduces the computational effort [17]. The valves are modelled as resistive devices with low resistance when conducting and high resistance when blocking, and the capacitors are modelled as DC voltage sources. The result is a model with a reduced number of nodes compared to a model including all the switches. The calculated capacitor voltages are made available for the lower level control system. The switching states are known because the firing pluses are supplied from the lower level control system. The equations for the Thévenin equivalent are given in the Specialization project [5] and the paper in Appendix E. Even though this implementation reduces the computational effort, it is mathematically exactly equivalent to conducting a traditional simulation.

Chapter 3

Modulation

3.1 Firing Control and Voltage Range

The implemented method uses shifted carrier waves to enable PWM firing control [28]. The carrier waves are compared with the reference voltage and this is used to determine how many submodules to insert in the multivalve.

An insertion order is given whenever the reference voltage wave crosses a carrier wave. If the reference wave becomes greater than the carrier wave, a submodule is inserted in the lower multivalve. As the number of inserted submodules in a phase is constant, a submodule will be bypassed in the upper multivalve simultaneously. When the reference wave becomes smaller than a carrier wave the opposite action takes place: a submodule in the upper multivalve is inserted and a submodule in the lower multivalve is bypassed. This makes sense considering the case when the reference voltage wave reaches its peak and is greater than all the carrier waves. At this point all the submodules in the upper multivalve are bypassed and half the DC voltage is available at the AC terminals.

3.1.1 Semi-Analytical Method Using Matlab

Figures 3.1, 3.2, and 3.3 illustrate how the insertion orders are given. The upper part of the figures shows the reference voltage wave and the carrier waves for a case with 4 submodules in each multivalve. The lower part shows the number of inserted submodules in the lower multivalve. A case with 4 submodules gives 5 effective steps, as zero submodules inserted is a possible operation state. The carrier waves are shifted an angle α_{shift} given as:

$$\alpha_{\text{shift}} = \frac{360}{\text{number of submodules in each multivalve}} \tag{3.1}$$

Defining the modulation index:

$$m = \frac{\text{Reference voltage peak}}{\text{Carrier waves peak}} \tag{3.2}$$

Figure 3.1 shows the situation when the modulation index, m, is 1.0. This means that the peak value of the reference wave equals the peak value of the carrier waves. Figure 3.2 shows the situation with modulation index 0.8. Notice how this gives an increased number of insertion orders compared to the case with $m = 1.0$. Figure 3.3 shows the situation with modulation index 1.2. As expected this gives fewer insertion orders compared to the cases with $m = 0.8$ and $m = 1.0$.

The maximal phase to neutral voltage occurs when all submodules in the upper multivalve are bypassed and all the submodules in the lower multivalve are inserted. This voltage is equal to half the DC voltage. The line to line rms voltage is found by multiplying this voltage with $\frac{\sqrt{3}}{\sqrt{2}}$ [29]. For the case in Figures 3.1, 3.2, and 3.3, this means that four inserted submodules in the lower multivalve gives a phase voltage of 300 kV, using the DC voltage value in Appendix B. This peak value gives a rms line to line value of $\frac{\sqrt{3}}{\sqrt{2}} \cdot 300\text{KV} = 367.42$ kV, which corresponds to a per unit value of $\frac{300}{\sqrt{\frac{3}{2}}300} = \sqrt{\frac{3}{2}} = 1.22$ pu.

Curve fitting is used in Figure 3.5-3.7 to determine the peak value of the fundamental frequency component of the insertion curves. The curves are approximated to a Fourier function with 8 terms. The results are shown in Table 3.1.

Table 3.1: Values from curve fitting

Modulation index	Amplitude	Line to line rms voltage [kV]
0.8	1.55	284.75
1.0	1.98	363.75
1.2	2.15	394.98

Figure 3.4 shows the case with modulation index 1.0 and an angular displacement of 15° compared to Figure 3.1. Curve fitting in Figure 3.8 shows that this is equivalent to an amplitude of 1.99, which is close to the result for Figure 3.5 ($m = 1.0$ but no angular displacement). In the simulations the number of submodules in each multivalve, and hence the number of carrier waves, is 38, so a phase shift like this would have a smaller effect. However, the principle seen when comparing Figures 3.4 and 3.1 is valid: the same modulation index and different insertion curves should give the same effective amplitude and accordingly the same rms voltage output.

3.1.2 Analytical Method Using Mathematical Expressions

The available voltage can be calculated directly using the modulation index [29]. The modulation curve can be divided into two sections: linear modulation and over-modulation. Linear modulation is used for modulation indexes $m \leq 1.0$. Over-modulation is used with modulation indexes $m > 1.0$, and the upper limit of over-modulation is square-wave [29].

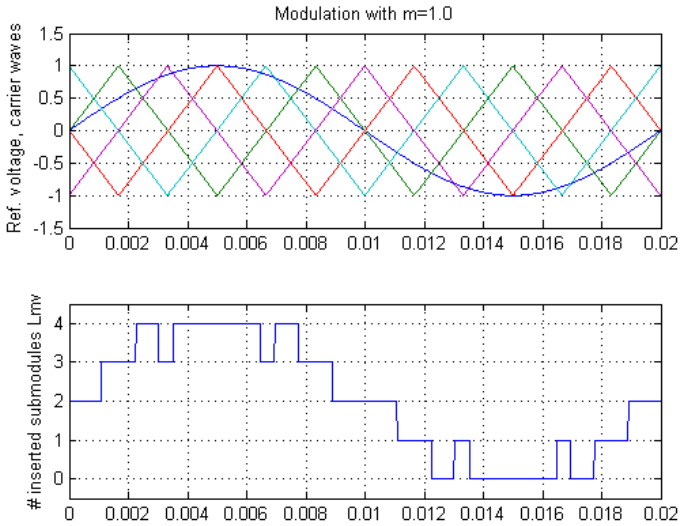

Figure 3.1: Reference wave, carrier waves, and number of inserted submodules in the lower multivalve with modulation index 1.0

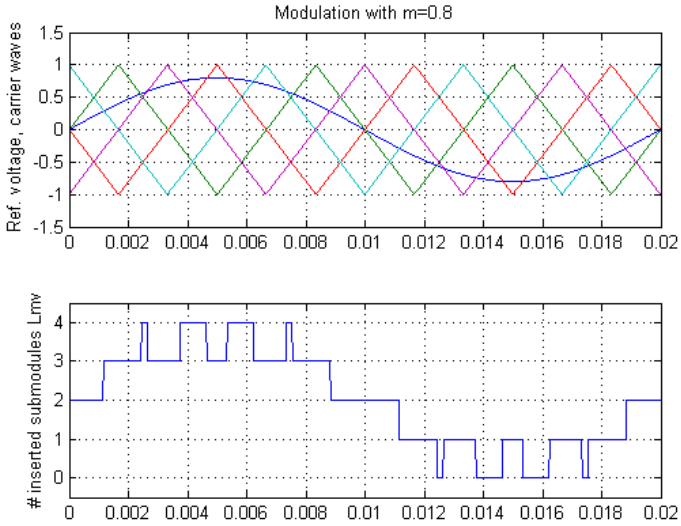

Figure 3.2: Reference wave, carrier waves, and number of inserted submodules in the lower multivalve with modulation index 0.8

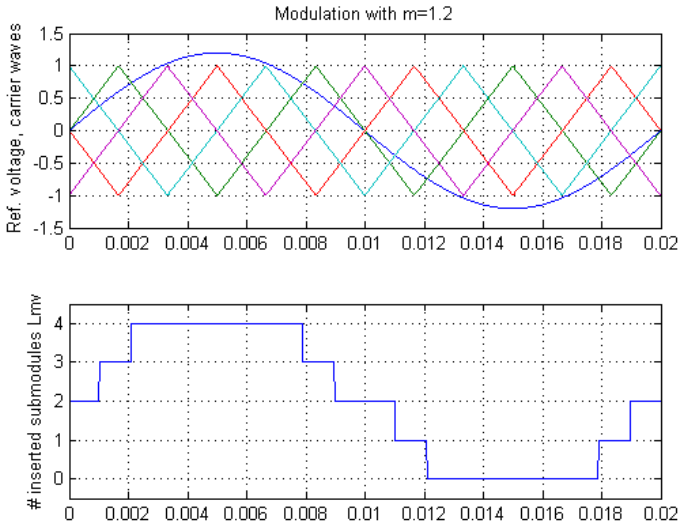

Figure 3.3: Reference wave, carrier waves, and number of inserted submodules in the lower multivalve with modulation index 1.2

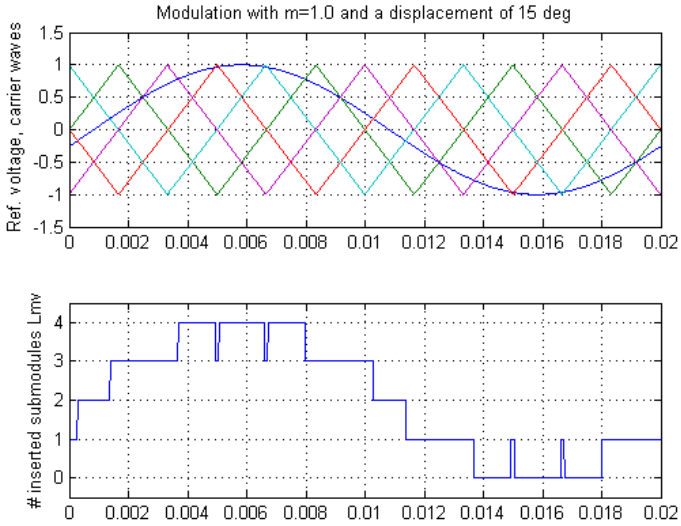

Figure 3.4: Reference wave, carrier waves, and number of inserted submodules in the lower multivalve with modulation index 1.0 and a displacement of 15°

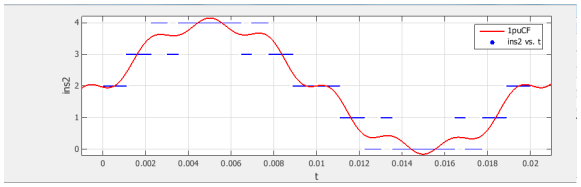

Figure 3.5: Curve fitting used on the insertion curve from Figure 3.1, $m = 1.0$. The approximation is a Fourier curve with 8 terms and gives fundamental frequency peak at 1.98.

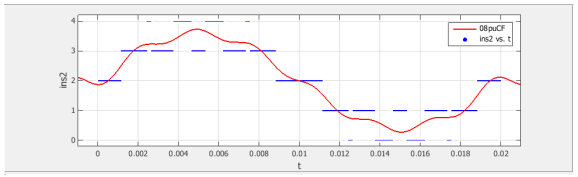

Figure 3.6: Curve fitting used on the insertion curve from Figure 3.2, $m = 0.8$. The approximation is a Fourier curve with 8 terms and gives fundamental frequency peak at 1.55.

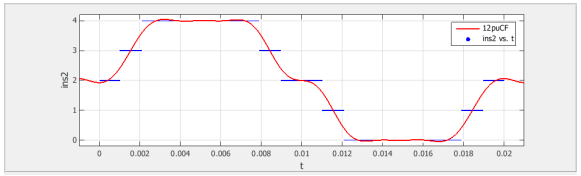

Figure 3.7: Curve fitting used on the insertion curve from Figure 3.3, $m = 1.2$. The approximation is a Fourier curve with 8 terms and gives fundamental frequency peak at 2.15.

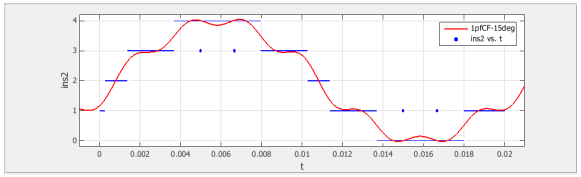

Figure 3.8: Curve fitting used on the insertion curve from Figure 3.4, $m = 1.0$ with a phase shift. The approximation is a Fourier curve with 8 terms and gives fundamental frequency peak at 1.99.

Linear modulation

Using linear modulation the voltage is proportional with the modulation index. The peak value of the fundamental frequency component in one phase is:

$$\hat{V}_{p-n} = m\frac{U_D}{2} \tag{3.3}$$

where the subscript p-n indicates phase to neutral and U_D is the total DC voltage.

Accordingly the line to line rms voltage can be written as:

$$V_{\text{LL-rms}} = \frac{\sqrt{3}}{\sqrt{2}}\hat{V}_{p-n} \tag{3.4}$$

$$V_{\text{LL-rms}} = \frac{\sqrt{3}}{\sqrt{2}}m\frac{U_D}{2} = \frac{\sqrt{3}}{2\sqrt{2}}mU_D \tag{3.5}$$

Inserting the DC voltage value from Appendix B:

$$V_{\text{LL-rms}} = \frac{\sqrt{3}}{2\sqrt{2}}m \cdot 600\text{kV} = m \cdot 367.42\text{kV} \tag{3.6}$$

Over-modulation

Using over-modulation the voltage does not vary linearly with the modulation index. The upper voltage limit is defined by square-wave modulation. Doing Fourier analysis on a square-wave gives the peak value of the fundamental frequency to be $\frac{4}{\pi}$ times the square-wave voltage level[29]. This value gives the upper limit for the peak phase to neutral voltage. Accordingly the voltage range in over-modulation is defined as:

$$\frac{U_D}{2} < \hat{V}_{p-n} < \frac{4}{\pi}\frac{U_D}{2} \tag{3.7}$$

$$\frac{\sqrt{3}}{\sqrt{2}}\frac{U_D}{2} < V_{\text{LL-rms}} < \frac{\sqrt{3}}{\sqrt{2}}\frac{4}{\pi}\frac{U_D}{2} \tag{3.8}$$

$$\frac{\sqrt{3}}{2\sqrt{2}}U_D < V_{\text{LL-rms}} < \frac{\sqrt{6}}{\pi}U_D \tag{3.9}$$

Inserting the DC voltage value from Appendix B:

$$367.42\text{kV} < V_{\text{LL-rms}} < 467.82\text{kV} \tag{3.10}$$

3.1.3 Comparison of the Values from the Semi-Analytical and the Analytical Method

Table 3.2 shows that the theoretical values are larger than the values gained from curve fitting. As the theoretical value is an idealistic case, this is no surprise. The limited number of submodules in the curve fitting plots leads to unsatisfactory voltage waveforms that are not representative for the simulations.

Table 3.2: Comparison of theoretical values and values from curve fitting for rms line to line voltage in the fundamental frequency

Modulation index	Theoretical value [kV]	Value from curve fitting [kV]
0.8	293.94	284.75
1.0	367.42	363.75
1.2	Over-modulation	394.98

3.2 Third Harmonic Distortion

The aim of adding third harmonic distortion to the reference voltage is to increase the AC voltage at the converter terminal without using over-modulation [30]. Over-modulation may lead to increased harmonic content and is therefore disadvantageous. Triplen harmonics can be added to the phase voltage waveform as these are cophasal, equal in the three phases, and therefore will be eliminated in the line to line voltage waveform.

The phase voltage waveform is assumed to be of this type [30]:

$$y = \sin(\theta) + a\sin(3\theta) \tag{3.11}$$

where $\theta = \omega t$ and a is a parameter.

In the following the value of a that gives the largest output voltage without going into over-modulation is determined. This means that the peak value of the reference voltage wave must be kept smaller than or equal to unity. At the same time the fundamental frequency component should be as large as possible. The reference voltage wave is proportional to the y function.

To find the turning points of the y function, y is differentiated with respect to θ and the result is equated to zero:

$$\frac{\mathrm{d}y}{\mathrm{d}\theta} = \cos(\theta) + 3a\cos(3\theta) = 0 \tag{3.12}$$

Using that $\cos(3\theta) = 4\cos^3(\theta) - 3\cos(\theta)$ gives:

$$\frac{\mathrm{d}y}{\mathrm{d}\theta} = \cos(\theta)[1 - 9a + 12a\cos^2(\theta)] = 0 \tag{3.13}$$

Equation 3.13 has two solutions:

$$\cos(\theta) = 0 \tag{3.14}$$

$$\cos^2(\theta) = \frac{9a - 1}{12a} \tag{3.15}$$

The solution in Equation 3.14 gives:

$$\sin(\theta) = \pm 1 \tag{3.16}$$

This corresponds to a peak in y at $\theta = 90°$ and $\theta = 270°$ independent of a.

The solution in Equation 3.15 gives:

$$\sin^2(\theta) = 1 - \cos^2(\theta) = 1 - \frac{9a-1}{12a} = \frac{3a+1}{12a} \tag{3.17}$$

With this solution the angle θ at which y reaches its peak is dependent on a.

Using that $\sin(3\theta) = 3\sin(\theta) - 4\sin^3(\theta)$ in Equation 3.11 leads to:

$$y = \sin(\theta)[1 + 3a - 4a\sin^2(\theta)] \tag{3.18}$$

Inserting the solution from Equation 3.14 that gives $\sin(\theta) = 1$ to find the peak value of y, $\hat{y}$ gives:

$$\hat{y} = 1 + 3a - 4a = 1 - a \tag{3.19}$$

As over-modulation is to be avoided, the peak values of y should be kept smaller than or equal to unity. It can be seen that this is not the case if $a < 0$.

Inserting the solution from Equation 3.15 to find $\hat{y}$ gives:

$$\hat{y} = \sqrt{\frac{3a+1}{12a}}[1 + 3a - 4a\frac{3a+1}{12a}] \tag{3.20}$$

$$\hat{y} = \sqrt{\frac{3a+1}{12a}}[\frac{2+6a}{3}] \tag{3.21}$$

To find the minimum value of $\hat{y}$, the function is differentiated with respect to a and the result is equated to zero:

$$\frac{\mathrm{d}\hat{y}}{\mathrm{d}a} = \frac{2+6a}{3}\frac{\mathrm{d}}{\mathrm{d}a}(\sqrt{\frac{3a+1}{12a}}) + \sqrt{\frac{3a+1}{12a}}\frac{\mathrm{d}}{\mathrm{d}a}(\frac{2+6a}{3}) = 0 \tag{3.22}$$

$$\frac{\mathrm{d}\hat{y}}{\mathrm{d}a} = \frac{1+3a}{3}\frac{-1}{12a^2}\sqrt{\frac{12a}{3a+1}} + 2\sqrt{\frac{3a+1}{12a}} = 0 \tag{3.23}$$

$$\sqrt{\frac{1+3a}{108a^3}} = \sqrt{\frac{3a+1}{3a}} \tag{3.24}$$

$$a = -\frac{1}{3} \qquad a = \frac{1}{6} \tag{3.25}$$

As a should not take on negative values, $a = \frac{1}{6}$ is the value to be used and y is given as:

$$y = \sin(\theta) + \frac{1}{6}\sin(3\theta) \tag{3.26}$$

Inserting $a = \frac{1}{6}$ into Equation 3.17 gives the sine value corresponding to the peak of the y function:

$$\sin(\theta) = \pm\sqrt{\frac{3\frac{1}{6}+1}{12\frac{1}{6}}} = \pm\frac{\sqrt{3}}{2} \tag{3.27}$$

This sine value appears at $\theta = 60°$, $\theta = 120°$, $\theta = 240°$, and $\theta = 300°$ and these are the angles at which y will reach its largest absolute value.

Inserting $a = \frac{1}{6}$ into Equation 3.21 gives the peak value of y:

$$\hat{y} = \sqrt{\frac{3\frac{1}{6}+1}{12\frac{1}{6}}}[\frac{2+6\frac{1}{6}}{3}] = \frac{\sqrt{3}}{2} \tag{3.28}$$

This will be the condition determining the upper value for the proportional constant between the y function and the reference voltage wave. Let K denote the proportional constant:

$$v_{\text{ref}} = Ky \tag{3.29}$$

The peak value of the reference voltage wave should be smaller than or equal to unity:

$$K\hat{y} = K\frac{\sqrt{3}}{2} \leq 1 \tag{3.30}$$

$$K \leq \frac{2}{\sqrt{3}} \approx 1.155 \tag{3.31}$$

The maximum corresponding voltage reference wave is then:

$$v_{\text{ref}} = \frac{2}{\sqrt{3}}[\sin(\theta) + \frac{1}{6}\sin(3\theta)] \tag{3.32}$$

This result shows that the fundamental frequency component magnitude can be increased with 15.5 % without going into over-modulation. The principle is shown in Figure 3.9.

The corresponding insertion curve from the reference voltage wave given by Equation 3.32 is shown in Figure 3.10. Curve fitting is used on the insertion curve as can be seen in Figure 3.11. The fundamental frequency component is found to have a peak at 2.15. This gives a rms voltage of 394.98 kV, the same result as for modulation index equal 1.2 and over-modulation in Table 3.1. The two curves shown in Figures 3.7 (modulation index 1.2) and 3.11 have quite similar shapes. However, the curve containing the third harmonic distortion has a lower magnitude at $\omega t = 90°$ and $\omega t = 270°$.

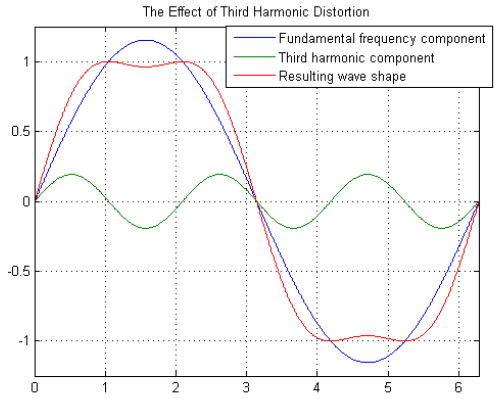

Figure 3.9: The effect of third harmonic distortion: When adding a third harmonic wave to the fundamental frequency wave, the peak value is reduced.

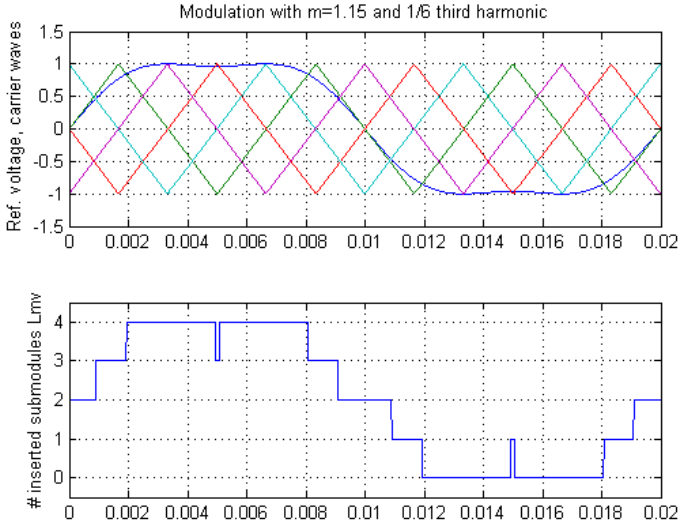

Figure 3.10: Reference wave, carrier waves, and number of inserted submodules in the lower multivalve with modulation index 1.15 in the fundamental frequency and $\frac{1}{6}$ third harmonic distortion

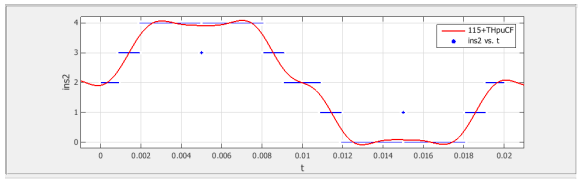

Figure 3.11: Curve fitting used on the insertion curve from Figure 3.10, $m = 1.15$ in the fundamental frequency and $\frac{1}{6}$ third harmonic distortion. The approximation is a Fourier curve with 8 terms and gives fundamental frequency peak at 2.15.

Chapter 4

Power Equations

4.1 Deduction of the Power Equations

Using Figure 4.1b to express currents and voltages [31]:

$$E\cos\delta = V + iR\cos\phi + iX\sin\phi \tag{4.1}$$

$$E\sin\delta = -iR\sin\phi + iX\cos\phi \tag{4.2}$$

Solving Equation 4.1 for $i\cos\phi$:

$$i\cos\phi = \frac{E\cos\delta - V - iX\sin\phi}{R} \tag{4.3}$$

Solving Equation 4.2 for $i\sin\phi$:

$$i\sin\phi = \frac{iX\cos\phi - E\sin\delta}{R} \tag{4.4}$$

Inserting Equation 4.4 into Equation 4.3:

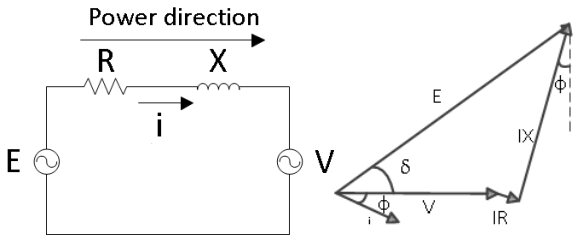

(a) The power system model (b) Phaser diagram

Figure 4.1: Network description for the case circuit

$$i\cos\phi = \frac{E\cos\delta - V - X\frac{iX\cos\phi - E\sin\delta}{R}}{R} \tag{4.5}$$

$$i\cos\phi = \frac{E(R\cos\delta + X\sin\delta) - VR}{R^2 + X^2} \tag{4.6}$$

Inserting Equation 4.6 into Equation 4.4:

$$i\sin\phi = \frac{X\frac{E(R\cos\delta + X\sin\delta) - VR}{R^2 + X^2} - E\sin\delta}{R} \tag{4.7}$$

$$i\sin\phi = \frac{E(X\cos\delta - R\sin\delta) - VX}{R^2 + X^2} \tag{4.8}$$

4.1.1 Power Delivered to the Stiff Grid

Expressing complex power:

$$\vec{S} = \vec{V}\vec{I}^* = P + jQ \tag{4.9}$$

$$\vec{I}^* = (i < -\phi)^* = i < \phi \tag{4.10}$$

$$\vec{S} = Vi(\cos\phi + j\sin\phi) = P + jQ \tag{4.11}$$

Using Equation 4.6 to express active power:

$$P = Vi\cos\phi = \frac{EV(R\cos\delta + X\sin\delta) - V^2R}{R^2 + X^2} \tag{4.12}$$

Using Equation 4.8 to express reactive power:

$$Q = Vi\sin\phi = \frac{EV(X\cos\delta - R\sin\delta) - V^2X}{R^2 + X^2} \tag{4.13}$$

4.1.2 Power Delivered from the Converter

Expressing complex power:

$$\vec{S} = \vec{E}\vec{I}^* = P + jQ \tag{4.14}$$

$$\vec{E} = E < \delta \tag{4.15}$$

$$\vec{I}^* = (i < -\phi)^* = i < \phi \tag{4.16}$$

$$\vec{S} = E(\cos\delta + j\sin\delta)i(\cos\phi + j\sin\phi) = P + jQ \tag{4.17}$$

Using Equations 4.6 and 4.8:

$$\vec{S} = E(\cos\delta + j\sin\delta)(\frac{E(R\cos\delta + X\sin\delta) - VR}{R^2+X^2} + j\frac{E(X\cos\delta - R\sin\delta) - VX}{R^2+X^2}) = P + jQ \quad (4.18)$$

$$\vec{S} = \frac{E^2(R\cos^2\delta + X\cos\delta\sin\delta) - VER\cos\delta}{R^2+X^2} + j\frac{E^2(X\cos^2\delta - R\cos\delta\sin\delta) - VEX\cos\delta}{R^2+X^2} + j\frac{E^2(R\cos\delta\sin\delta + X\sin^2\delta) - VER\sin\delta}{R^2+X^2} - \frac{E^2(X\cos\delta\sin\delta - R\sin^2\delta) - VEX\sin\delta}{R^2+X^2} = P + jQ \quad (4.19)$$

$$\vec{S} = \frac{VE(X\sin\delta - R\cos\delta) + E^2R}{R^2+X^2} + j\frac{-VE(X\cos\delta + R\sin\delta) + E^2X}{R^2+X^2} = P + jQ \quad (4.20)$$

$$P = \frac{VE(X\sin\delta - R\cos\delta) + E^2R}{R^2+X^2} \quad (4.21)$$

$$Q = \frac{-VE(X\cos\delta + R\sin\delta) + E^2X}{R^2+X^2} \quad (4.22)$$

4.1.3 Apparent Power Delivered to the Stiff Grid

Apparent power is given as:

$$S = \sqrt{P^2+Q^2} \quad (4.23)$$

Inserting from Equations 4.12 and 4.13:

$$S = \sqrt{(\frac{EV(R\cos\delta + X\sin\delta) - V^2R}{R^2+X^2})^2 + (\frac{EV(R\sin\delta - X\cos\delta) + V^2X}{R^2+X^2})^2} \quad (4.24)$$

$$S = \sqrt{\frac{E^2V^2(R^2+X^2) - 2EV^3[(R^2+X^2)\cos\delta] + V^4[R^2+X^2]}{(R^2+X^2)^2}} \quad (4.25)$$

$$S = \sqrt{\frac{V^2(E^2 - 2EV\cos\delta + V^2)}{R^2+X^2}} \quad (4.26)$$

4.1.4 Apparent Power Delivered from the Converter

Apparent power is given as:

$$S = \sqrt{P^2 + Q^2} \tag{4.27}$$

Inserting from Equations 4.21 and 4.22:

$$S = \sqrt{(\frac{VE(X\sin\delta - R\cos\delta) + E^2R}{R^2 + X^2})^2 + (\frac{-VE(X\cos\delta + R\sin\delta) + E^2X}{R^2 + X^2})^2} \tag{4.28}$$

$$S = \sqrt{\frac{E^2(V^2 + E^2 - 2VE\cos\delta)(X^2 + R^2)}{(R^2 + X^2)^2}} \tag{4.29}$$

$$S = \sqrt{\frac{E^2(V^2 - 2VE\cos\delta + E^2)}{R^2 + X^2}} \tag{4.30}$$

4.1.5 Inserting Values from the Simulation Model

The parameter values are stated in Appendix B, giving $R = R_f = 0.0015$ pu and $L = L_f + L_t$ where $L_f = 0.150$ pu, and $L_t = 0.1$ pu. Hence the total inductance is $L = 0.25$ pu. The stiff grid has a constant voltage $V = 1.0$ pu.

Active Power Inserting the values into Equation 4.12 gives:

$$P = \frac{E \cdot 1.0 \cdot (0.0015\cos\delta + 0.25\sin\delta) - 1.0^2 \cdot 0.0015}{0.0015^2 + 0.25^2} \tag{4.31}$$

$$P = \frac{E \cdot (0.0015\cos\delta + 0.25\sin\delta) - 0.0015}{0.0625} \tag{4.32}$$

This is illustrated in Figure 4.2.

Inserting the values into Equation 4.21 gives:

$$P = \frac{E \cdot 1.0 \cdot (0.25 \cdot \sin\delta - 0.0015 \cdot \cos\delta) + E^2 \cdot 0.0015}{0.0015^2 + 0.25^2} \tag{4.33}$$

$$P = \frac{E \cdot (0.25 \cdot \sin\delta - 0.0015 \cdot \cos\delta) + E^2 \cdot 0.0015}{0.0625} \tag{4.34}$$

This is illustrated in Figure 4.3.

In both Figure 4.2 and Figure 4.3 active power is positive for small values of angle δ and negative for large angle values. The active power is increasing with the terminal voltage E. The two curves are quite similar.

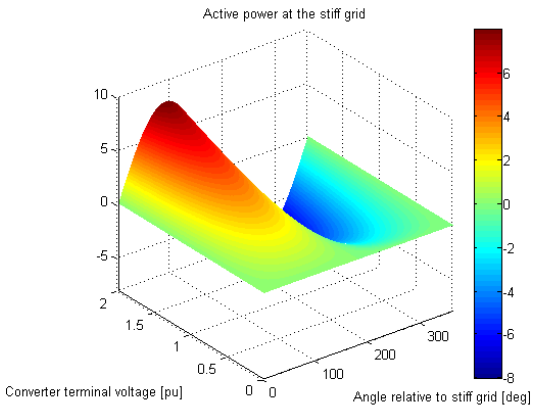

Figure 4.2: Active power [pu] at the stiff grid as a function of terminal voltage and grid angle δ

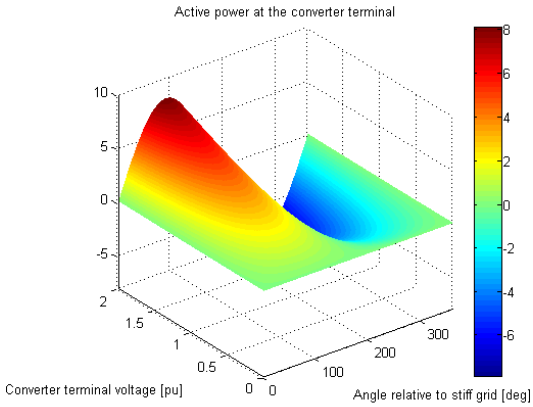

Figure 4.3: Active power [pu] at the converter terminal as a function of terminal voltage and grid angle δ

Reactive Power Inserting the values into 4.13 gives:

$$Q = \frac{E \cdot 1.0 \cdot (0.25 \cos\delta - 0.0015 \sin\delta) - 1.0^2 \cdot 0.25}{0.0015^2 + 0.25^2} \tag{4.35}$$

$$Q = \frac{E \cdot (0.25 \cos\delta - 0.0015 \sin\delta) - 0.25}{0.0625} \tag{4.36}$$

This is illustrated in Figure 4.4.

Inserting the values into Equation 4.22 gives:

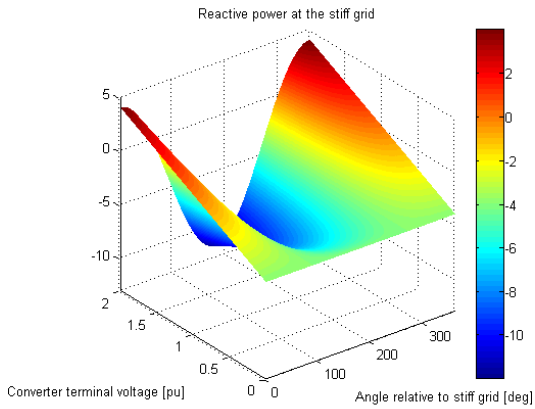

Figure 4.4: Reactive power [pu] at the stiff grid as a function of terminal voltage and grid angle δ

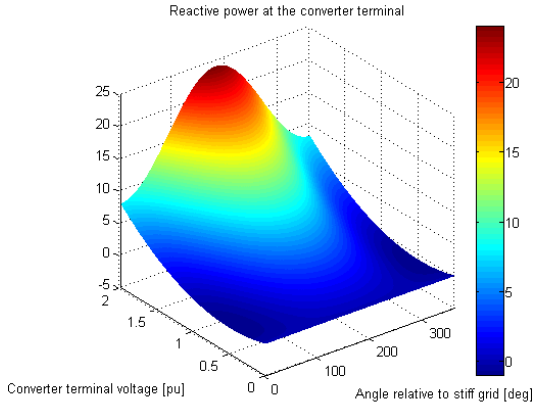

Figure 4.5: Reactive power [pu] at the converter terminal as a function of terminal voltage and grid angle δ

$$Q = \frac{-E \cdot 1.0 \cdot (0.25 \cos\delta + 0.0015 \sin\delta) + E^2 \cdot 0.25}{0.0015^2 + 0.25^2} \tag{4.37}$$

$$Q = \frac{-E \cdot (0.25 \cos\delta + 0.0015 \sin\delta) + E^2 \cdot 0.25}{0.0625} \tag{4.38}$$

This is illustrated in Figure 4.5.

Figures 4.4 and 4.5 show quite different results. While the reactive power at the stiff grid is almost always negative, and smallest for angle δ values around 180°, the reactive power at the converter terminal is mostly positive and peaks around angle δ equal 180°.

Apparent power Inserting the values into 4.26 gives:

$$S = \sqrt{\frac{E^2 \cdot 1.0^2 - 2 \cdot E \cdot 1.0^3 \cdot \cos\delta + 1.0^4}{0.0015^2 + 0.25^2}} \tag{4.39}$$

$$S = \sqrt{\frac{E^2 - 2 \cdot E \cdot \cos\delta + 1.0}{0.0625}} \tag{4.40}$$

This is illustrated in Figure 4.6.

Inserting the values into Equation 4.30:

$$S = \sqrt{\frac{E^2(1.0^2 - 2 \cdot 1.0 \cdot E\cos\delta + E^2)}{0.0015^2 + 0.25^2}} \tag{4.41}$$

$$S = \sqrt{\frac{E^2(1.0 - 2 \cdot E\cos\delta + E^2)}{0.0625}} \tag{4.42}$$

This is illustrated in Figure 4.7.

Both in Figure 4.6 and Figure 4.7 the apparent power peaks around angle δ equal 180°, but the magnitude is much larger at the converter terminal.

Further plots of active power, reactive power and apparent power as functions of angle δ at different terminal voltage levels are shown in section 4.4.

4.1.6 Positive Reactive Power Delivered to the Grid

The reactive power should be kept larger than zero to ensure voltage support to the grid. Using Equation 4.13:

$$Q = \frac{EV(X\cos\delta - R\sin\delta) - V^2X}{R^2 + X^2} > 0 \tag{4.43}$$

$$E(X\cos\delta - R\sin\delta) - VX > 0 \tag{4.44}$$

$$E(\cos\delta - \frac{R}{X}\sin\delta) > V \tag{4.45}$$

$$E\sqrt{\frac{R^2}{X^2} + 1}\cos(\delta - \arctan(-\frac{R}{X})) > V \tag{4.46}$$

Inserting values from Appendix B:

$$E\cos(\delta + 0.34°) > 0.9982 \tag{4.47}$$

To get a positive value of Q is only possible for E larger than 1. For larger voltages the δ angle must be kept in a certain range. This is shown in Table 4.1.

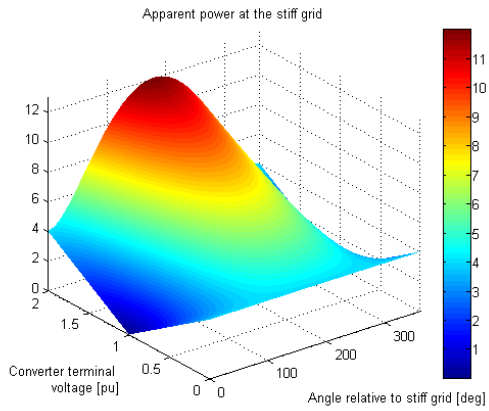

Figure 4.6: Apparent power [pu] at the stiff grid as a function of terminal voltage and grid angle δ

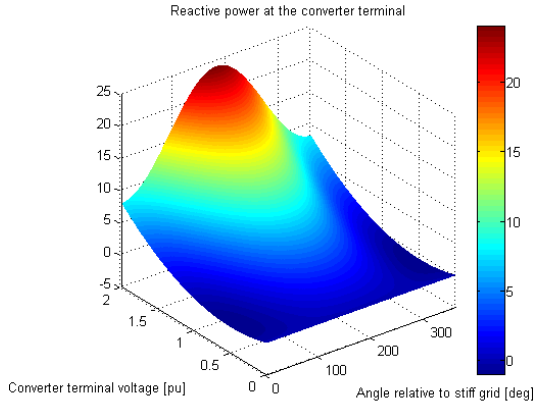

Figure 4.7: Apparent power [pu] at the converter terminal as a function of terminal voltage and grid angle δ

Table 4.1: Angle δ values that give positive reactive power at the grid for different converter terminal voltages

E [pu]	Angle δ giving Q>0
1.0	$0° \leq \delta \leq 0°$
1.1	$-24.97° < \delta < 24.28°$
1.2	$-33.90° < \delta < 33.22°$
1.3	$-40.06° < \delta < 39.37°$
1.4	$-44.76° < \delta < 44.07°$

4.2 Maximum Power Transfer

4.2.1 The Optimal Angle δ Value

Active power $\delta_{\mathbf{maxP}}$

The maximum active power transfer is given by the angle δ_{maxP} that gives the largest value for active power. The result is found by differentiating Equation 4.12

with respect to δ and equalize the equation to zero.

Differentiating of the active power function with respect to δ:

$$\frac{\mathrm{d}P}{\mathrm{d}\delta} = \frac{\mathrm{d}}{\mathrm{d}\delta}\left(\frac{EV(R\cos\delta + X\sin\delta) - V^2R}{R^2 + X^2}\right) \tag{4.48}$$

$$\frac{\mathrm{d}P}{\mathrm{d}\delta} = \frac{EV(X\cos\delta - R\sin\delta)}{R^2 + X^2} \tag{4.49}$$

Equalizing to zero to find the angle δ_{maxP} that gives the largest power transfer:

$$\frac{\mathrm{d}P}{\mathrm{d}\delta}|_{\delta=\delta_{\mathrm{maxP}}} = 0 \tag{4.50}$$

$$\frac{\mathrm{d}P}{\mathrm{d}\delta}|_{\delta=\delta_{\mathrm{maxP}}} = \frac{EV(X\cos\delta_{\mathrm{maxP}} - R\sin\delta_{\mathrm{maxP}})}{R^2 + X^2} = 0 \tag{4.51}$$

$$\frac{X}{R} = \frac{\sin\delta_{\mathrm{maxP}}}{\cos\delta_{\mathrm{maxP}}} \tag{4.52}$$

δ_{maxP} is found to be:

$$\delta_{\mathrm{maxP}} = \arctan\left(\frac{X}{R}\right) = \arctan\left(\frac{0.25}{0.0015}\right) \tag{4.53}$$

$$\delta_{\mathrm{maxP}} = 89.66^\circ \qquad \delta_{\mathrm{maxP}} = 269.66^\circ \tag{4.54}$$

The first value gives the positive maximum for the active power function. The second gives the negative maximum.

Inserting the value of δ_{maxP} into the original active power function:

$$P|_{\delta=\delta_{\mathrm{maxP}}} = \frac{EV(R\cos\delta_{\mathrm{maxP}} + X\sin\delta_{\mathrm{maxP}}) - V^2R}{R^2 + X^2} \tag{4.55}$$

Inserting the values from Appendix B:

$$P|_{\delta=\delta_{\mathrm{maxP}}} = \frac{E(0.0015\cos\delta_{\mathrm{maxP}} + 0.25\sin\delta_{\mathrm{maxP}}) - 0.0015}{0.0625} \tag{4.56}$$

Calculating the positive maximum:

$$P|_{\delta=\delta_{\mathrm{maxP}}} = \frac{E(0.0015\cdot 0.0060 + 0.25\cdot 1.0) - 0.0015}{0.0625} \tag{4.57}$$

$$P|_{\delta=\delta_{\mathrm{maxP}}} = \frac{E\cdot 0.25 - 0.0015}{0.0625} = 4E - 0.024 \tag{4.58}$$

Calculating the negative maximum:

$$P|_{\delta=\delta_{\mathrm{maxP}}} = \frac{E(0.0015\cdot(-0.0060) + 0.25\cdot(-1.0)) - 0.0015}{0.0625} \tag{4.59}$$

$$P|_{\delta=\delta_{\max P}} = -\frac{E \cdot 0.25 + 0.0015}{0.0625} = -(4E + 0.024) \tag{4.60}$$

Inserting the value of $\delta_{\max P}$ into the reactive power function from Equation 4.13:

$$Q|_{\delta=\delta_{\max P}} = \frac{EV(X\cos\delta_{\max P} - R\sin\delta_{\max P}) - V^2X}{R^2 + X^2} \tag{4.61}$$

Inserting the values from Appendix B:

$$Q|_{\delta=\delta_{\max P}} = \frac{E(0.25\cos\delta_{\max P} - 0.0015\sin\delta_{\max P}) - 0.25}{0.0625} \tag{4.62}$$

For both the positive and negative maximum:

$$Q|_{\delta=\delta_{\max P}} = \frac{E(0.25 \cdot (\pm 0.0060) - 0.0015 \cdot (\pm 1.0)) - 0.25}{0.0625} \tag{4.63}$$

$$Q|_{\delta=\delta_{\max P}} = \frac{-0.25}{0.0625} = -4 \tag{4.64}$$

Inserting the value of $\delta_{\max P}$ into the apparent power function from Equation 4.26:

$$S|_{\delta=\delta_{\max P}} = \sqrt{\frac{V^4 - 2EV^3\cos\delta_{\max P} + V^2E^2}{R^2 + X^2}} \tag{4.65}$$

Inserting the values from Appendix B:

$$S|_{\delta=\delta_{\max P}} = \sqrt{\frac{1.0 - 2E\cos\delta_{\max P} + E^2}{0.0625}} \tag{4.66}$$

For the positive maximum:

$$S|_{\delta=\delta_{\max P}} = 4\sqrt{1.0 - 0.012E + E^2} \tag{4.67}$$

For the negative maximum:

$$S|_{\delta=\delta_{\max P}} = 4\sqrt{1.0 + 0.012E + E^2} \tag{4.68}$$

Reactive power $\delta_{\max Q}$

The maximum reactive power transfer is given by the angle $\delta_{\max Q}$ that gives the largest value for reactive power. The result is found by differentiating Equation 4.13 with respect to δ and equalize the equation to zero.

Differentiating of the active power function with respect to δ:

$$\frac{\mathrm{d}Q}{\mathrm{d}\delta} = \frac{\mathrm{d}}{\mathrm{d}\delta}\frac{EV(X\cos\delta - R\sin\delta) - V^2X}{R^2 + X^2} \tag{4.69}$$

$$\frac{\mathrm{d}Q}{\mathrm{d}\delta} = \frac{EV(-X\sin\delta - R\cos\delta)}{R^2 + X^2} = \frac{-EV(X\sin\delta + R\cos\delta)}{R^2 + X^2} \tag{4.70}$$

Equalizing to zero to find the angle $\delta_{\max Q}$ that gives the largest power transfer:

$$\frac{\mathrm{d}Q}{\mathrm{d}\delta}|_{\delta=\delta_{\max Q}} = 0 \tag{4.71}$$

$$\frac{\mathrm{d}Q}{\mathrm{d}\delta}|_{\delta=\delta_{\max Q}} = \frac{-EV(X\sin\delta_{\max Q} + R\cos\delta_{\max Q})}{R^2+X^2} = 0 \tag{4.72}$$

$$-\frac{R}{X} = \frac{\sin\delta_{\max Q}}{\cos\delta_{\max Q}} \tag{4.73}$$

$\delta_{\max Q}$ is found to be:

$$\delta_{\max Q} = \arctan(-\frac{R}{X}) = \arctan(-\frac{0.0015}{0.25}) \tag{4.74}$$

$$\delta_{\max Q} = -0.34^\circ \qquad \delta_{\max Q} = 179.66^\circ \tag{4.75}$$

The first value gives the positive maximum for the reactive power function. The second gives the negative maximum.

Inserting the value of $\delta_{\max Q}$ into the original reactive power function:

$$Q|_{\delta=\delta_{\max Q}} = \frac{EV(X\cos\delta_{\max Q} - R\sin\delta_{\max Q}) - V^2X}{R^2+X^2} \tag{4.76}$$

Inserting the values from Appendix B:

$$Q|_{\delta=\delta_{\max Q}} = \frac{E(0.25\cos\delta_{\max Q} - 0.0015\sin\delta_{\max Q}) - 0.25}{0.0625} \tag{4.77}$$

Calculating the positive maximum:

$$Q|_{\delta=\delta_{\max Q}} = \frac{E(0.25\cdot 1.0 - 0.0015\cdot(-0.0060)) - 0.25}{0.0625} \tag{4.78}$$

$$Q|_{\delta=\delta_{\max Q}} = \frac{E\cdot 0.25 - 0.25}{0.0625} = 4(E-1) \tag{4.79}$$

Calculating the negative maximum:

$$Q|_{\delta=\delta_{\max Q}} = \frac{E(0.25\cdot(-1.0) - 0.0015\cdot 0.0060) - 0.25}{0.0625} \tag{4.80}$$

$$Q|_{\delta=\delta_{\max Q}} = -\frac{E\cdot 0.25 + 0.25}{0.0625} = -4(E+1) \tag{4.81}$$

Inserting the value of $\delta_{\max P}$ into the active power function from Equation 4.12:

$$P|_{\delta=\delta_{\max Q}} = \frac{EV(R\cos\delta_{\max Q} + X\sin\delta_{\max Q}) - V^2R}{R^2+X^2} \tag{4.82}$$

Inserting the values from Appendix B:

$$P|_{\delta=\delta_{\max Q}} = \frac{E(0.0015\cos\delta_{\max Q} + 0.25\sin\delta_{\max Q}) - 0.015}{0.0625} \tag{4.83}$$

For both the positive and negative maximum:

$$P|_{\delta=\delta_{\max Q}} = \frac{E(0.0015\cdot(\pm 1.0) + 0.25(\mp 0.0060)) - 0.0015}{0.0625} \tag{4.84}$$

$$P|_{\delta=\delta_{\max Q}} = -\frac{0.0015}{0.0625} = -0.024 \tag{4.85}$$

Inserting the value of $\delta_{\max Q}$ into the apparent power function from Equation 4.26:

$$S|_{\delta=\delta_{\max Q}} = \sqrt{\frac{V^4 - 2EV^3\cos\delta_{\max Q} + V^2E^2}{R^2+X^2}} \tag{4.86}$$

Inserting the values from Appendix B:

$$S|_{\delta=\delta_{\max Q}} = \sqrt{\frac{1.0 - 2\cdot E\cdot\cos\delta_{\max Q} + E^2}{0.0625}} \tag{4.87}$$

For the positive maximum:

$$S|_{\delta=\delta_{\max Q}} = \sqrt{\frac{1.0 - 2E + E^2}{0.0625}} = 4\sqrt{(1.0-E)^2} \tag{4.88}$$

For the negative maximum:

$$S|_{\delta=\delta_{\max P}} = \sqrt{\frac{1.0 + 2E + E^2}{0.0625}} = 4\sqrt{(1.0+E)^2} \tag{4.89}$$

4.2.2 The Optimal Inductance Value

Active Power $X_{\max P}$

The maximum active power transfer is given by the inductance value $X_{\max P}$ that gives the largest value for active power. Differentiating Equation 4.12 with respect to X:

$$\frac{\mathrm{d}P}{\mathrm{d}X} = \frac{\mathrm{d}}{\mathrm{d}X}\frac{EV(R\cos\delta + X\sin\delta) - V^2R}{R^2+X^2} \tag{4.90}$$

$$\frac{\mathrm{d}P}{\mathrm{d}X} = \frac{EV[(R^2-X^2)\sin\delta - 2XR\cos\delta] + 2V^2XR}{(R^2+X^2)^2} \tag{4.91}$$

Equalizing to zero:

$$\frac{\mathrm{d}P}{\mathrm{d}X}|_{X=X_{\max P}} = 0 \tag{4.92}$$

$$\frac{\mathrm{d}P}{\mathrm{d}X}|_{X=X_{\mathrm{maxP}}} = \frac{EV[(R^2 - X_{\mathrm{maxP}}^2)\sin\delta - 2X_{\mathrm{maxP}}R\cos\delta] + 2V^2X_{\mathrm{maxP}}R}{(R^2 + X_{\mathrm{maxP}}^2)^2} = 0 \tag{4.93}$$

$$X_{\mathrm{maxP}}^2 E\sin\delta + X_{\mathrm{maxP}}2R(E\cos\delta - V) - R^2E\sin\delta = 0 \tag{4.94}$$

$$X_{\mathrm{maxP}} = -\frac{R(E\cos\delta - V)}{E\sin\delta} \pm R\frac{\sqrt{E^2 - 2EV\cos\delta + V^2}}{E\sin\delta} \tag{4.95}$$

As X is a physical size the value must be larger than zero.

In the first and second quadrant with $0° < \delta < 180°$ $\sin\delta > 0$
$X_{\mathrm{maxP}} = R\frac{-(E\cos\delta - V) + \sqrt{E^2 - 2EV\cos\delta + V^2}}{E\sin\delta}$ is larger than zero as
$\sqrt{E^2 - 2EV\cos\delta + V^2} = \sqrt{(E\cos\delta - V)^2 + (E\sin\delta)^2} \geq |E\cos\delta - V|$. At $\delta = 0°$ and $\delta = 180°$ both the nominator and the denominator equal zero if $E \geq V$. L'Hôpitals rule is used:

$$\lim_{\delta\to 0°} X_{\mathrm{maxP}} = \lim_{\delta\to 0°} -\frac{R(E\cos\delta - V)}{E\sin\delta} + R\frac{\sqrt{E^2 - 2EV\cos\delta + V^2}}{E\sin\delta} \tag{4.96}$$

$$\lim_{\delta\to 0°} X_{\mathrm{maxP}} = \lim_{\delta\to 0°} \frac{RE\sin\delta}{E\cos\delta} + R\frac{1}{2}\frac{1}{\sqrt{E^2 - 2EV\cos\delta + V^2}}\frac{2EV\sin\delta}{E\cos\delta} = 0 \tag{4.97}$$

As $\sin 0° = 0$ the nominator is zero and $X_{\mathrm{maxP}} = 0$. The inductance expression is therefore not valid in this point.

$$\lim_{\delta\to 180°} X_{\mathrm{maxP}} = \lim_{\delta\to 180°} -\frac{R(E\cos\delta - V)}{E\sin\delta} + R\frac{\sqrt{E^2 - 2EV\cos\delta + V^2}}{E\sin\delta} \tag{4.98}$$

$$\lim_{\delta\to 180°} X_{\mathrm{maxP}} = \lim_{\delta\to 180°} \frac{RE\sin\delta}{E\cos\delta} + R\frac{1}{2}\frac{1}{\sqrt{E^2 - 2EV\cos\delta + V^2}}\frac{2EV\sin\delta}{E\cos\delta} = 0 \tag{4.99}$$

As $\sin 180° = 0$ the nominator is zero and $X_{\mathrm{maxP}} = 0$. The inductance expression is therefore not valid in this point.

In the third and fourth quadrant with $180° < \delta < 360°$ $\sin\delta < 0$
$X_{\mathrm{maxP}} = -R\frac{E\cos\delta - V + \sqrt{E^2 - 2EV\cos\delta + V^2}}{E\sin\delta}$ is larger than zero.

The value of X_{maxP} for different values of δ is shown in Figure 4.8.

Inserting the result from Equation 4.95 into Equation 4.12:

$$P|_{X=X_{\mathrm{maxP}}} = \frac{EV(R\cos\delta + X_{\mathrm{maxP}}\sin\delta) - V^2R}{R^2 + X_{\mathrm{maxP}}^2} \tag{4.100}$$

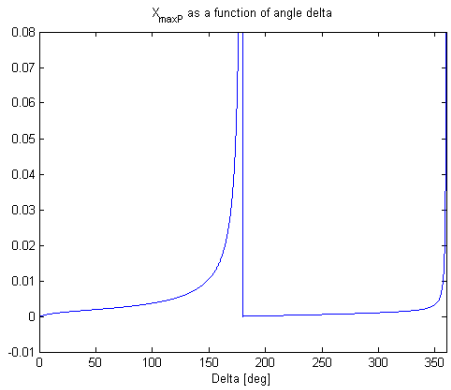

Figure 4.8: X_{maxP} [pu] as a function of δ with V=1.0 pu, E=1.2 pu, and R=0.0015 pu

$$P|_{X=X_{\text{maxP}}} = \frac{EV(R\cos\delta + (-\frac{R(E\cos\delta - V)}{E\sin\delta} \pm R\frac{\sqrt{E^2-2EV\cos\delta+V^2}}{E\sin\delta})\sin\delta) - V^2R}{R^2 + (-\frac{R(E\cos\delta - V)}{E\sin\delta} \pm R\frac{\sqrt{E^2-2EV\cos\delta+V^2}}{E\sin\delta})^2} \tag{4.101}$$

$$P|_{X=X_{\text{maxP}}} = \frac{\pm VE^2\sin^2\delta\sqrt{E^2-2EV\cos\delta+V^2}}{2R(E^2-2EV\cos\delta+V^2 \pm (V-E\cos\delta)\sqrt{E^2-2EV\cos\delta+V^2})} \tag{4.102}$$

$$P|_{X=X_{\text{maxP}}} = \frac{\pm VE^2\sin^2\delta}{2R(\sqrt{E^2-2EV\cos\delta+V^2} \pm (V-E\cos\delta))} \tag{4.103}$$

The first term in the denominator can be rewritten:

$$\sqrt{E^2-2EV\cos\delta+V^2} = \sqrt{(E\cos\delta - V)^2 + E^2\sin^2\delta} \geq \sqrt{(E\cos\delta - V)^2} = |E\cos\delta - V| \tag{4.104}$$

It can be seen that this term is always larger than or equal to the second term. Hence the denominator is always positive.

First solution valid for $0° < \delta < 180°$:

$$P|_{X=X_{\text{maxP}}} = \frac{VE^2\sin^2\delta}{2R(\sqrt{E^2-2EV\cos\delta+V^2}+V-E\cos\delta)} \tag{4.105}$$

Active power can only take on positive values in this angle range.

Second solution valid for $180° < \delta < 360°$:

$$P|_{X=X_{\text{maxP}}} = \frac{-VE^2\sin^2\delta}{2R(\sqrt{E^2-2EV\cos\delta+V^2}+E\cos\delta-V)} \tag{4.106}$$

This solution can only take on negative values.
$P|_{X=X_{\mathrm{maxP}}}$ as a function of δ is shown in Figure 4.9.

Reactive Power $X_{\mathbf{maxQ}}$

The maximum reactive power transfer is given by the inductance value X_{maxQ} that gives the largest value for reactive power. Differentiating Equation 4.13 with respect to X:

$$\frac{\mathrm{d}Q}{\mathrm{d}X} = \frac{\mathrm{d}}{\mathrm{d}X}\frac{EV(X\cos\delta - R\sin\delta) - V^2X}{R^2+X^2} \tag{4.107}$$

$$\frac{\mathrm{d}Q}{\mathrm{d}X} = \frac{(EV\cos\delta - V^2)(R^2-X^2) + 2EVRX\sin\delta}{(R^2+X^2)^2} \tag{4.108}$$

Equalizing to zero:

$$\frac{\mathrm{d}Q}{\mathrm{d}X}|_{X=X_{\mathrm{maxQ}}} = 0 \tag{4.109}$$

$$\frac{\mathrm{d}Q}{\mathrm{d}X}|_{X=X_{\mathrm{maxQ}}} = \frac{(EV\cos\delta - V^2)(R^2-X_{\mathrm{maxQ}}^2) + 2EVRX_{\mathrm{maxQ}}\sin\delta}{(R^2+X_{\mathrm{maxQ}}^2)^2} = 0 \tag{4.110}$$

$$X_{\mathrm{maxQ}}^2 - \frac{2ER\sin\delta}{E\cos\delta - V}X_{\mathrm{maxQ}} - R^2 = 0 \tag{4.111}$$

$$X_{\mathrm{maxQ}} = \frac{RE\sin\delta}{E\cos\delta - V} \pm R\frac{\sqrt{E^2 - 2EV\cos\delta + V^2}}{E\cos\delta - V} \tag{4.112}$$

Also in this case X must be larger than zero. The sign is determined by the sign of the denominator, which is positive when $E\cos\delta > V$ and otherwise negative.

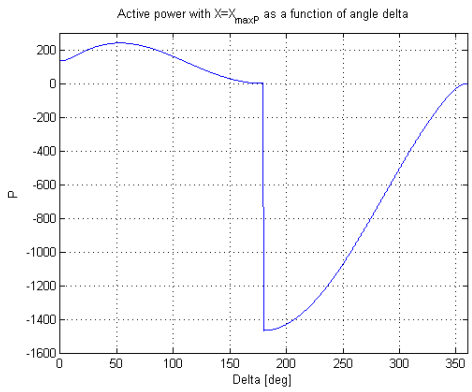

Figure 4.9: Active power [pu] with $X = X_{maxP}$ as a function of δ with V=1.0 pu, E=1.2 pu, and R=0.0015 pu

The positive region depends on the sizes of E and V, but will be located around $\delta = 0°$. Both terms in the denominator are negative for $90° < \delta < 270°$.

The ratio of the sizes between the two terms in the nominator is given from this expression:

$$\sqrt{E^2 - 2EV\cos\delta + V^2} = \sqrt{(E\cos\delta - V)^2 + E^2\sin^2\delta} \geq \sqrt{E^2\sin^2\delta} = |E\sin\delta| \tag{4.113}$$

It can be seen that the second term is always larger than or equal to the first term.

When the denominator is positive, the positive sign in the nominator must be used giving:

$$X_{\mathrm{maxQ}}|_{E\cos\delta > V} = R\frac{E\sin\delta + \sqrt{E^2 - 2EV\cos\delta + V^2}}{E\cos\delta - V} \tag{4.114}$$

Otherwise the negative sign must be used:

$$X_{\mathrm{maxQ}}|_{E\cos\delta < V} = R\frac{E\sin\delta - \sqrt{E^2 - 2EV\cos\delta + V^2}}{E\cos\delta - V} \tag{4.115}$$

The value of X_{maxQ} for different values of δ is shown in Figure 4.10.

Equations 4.95 and 4.112 show how the relation $\frac{X}{R}$ is an important system parameter. This can also be seen from Equations 4.54 and 4.75 as both angles are determined by this fraction. The fraction is given by the physical characteristics of the grid and cannot be easily changed. This however, does not make knowledge about its significance less important.

Inserting the result from Equation 4.112 into Equation 4.13:

$$Q|_{X=X_{\mathrm{maxQ}}} = \frac{EV(X_{\mathrm{maxQ}}\cos\delta - R\sin\delta) - V^2X_{\mathrm{maxQ}}}{R^2 + X_{\mathrm{maxQ}}^2} \tag{4.116}$$

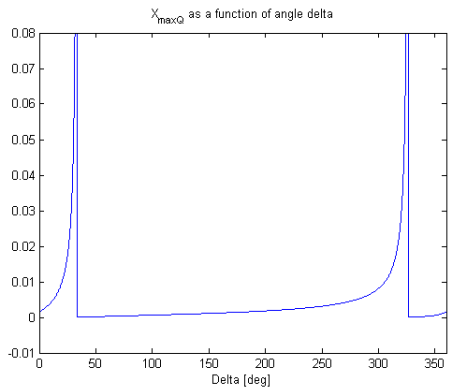

Figure 4.10: X_{maxQ} [pu] as a function of δ with V=1.0 pu, E=1.2 pu, and R=0.0015 pu

$$Q|_{X=X_{\mathrm{maxQ}}} = \frac{EV((\frac{RE\sin\delta}{E\cos\delta-V} \pm R\frac{\sqrt{E^2-2EV\cos\delta+V^2}}{E\cos\delta-V})\cos\delta - R\sin\delta)}{R^2+(\frac{RE\sin\delta}{E\cos\delta-V} \pm R\frac{\sqrt{E^2-2EV\cos\delta+V^2}}{E\cos\delta-V})^2} - \frac{V^2(\frac{RE\sin\delta}{E\cos\delta-V} \pm R\frac{\sqrt{E^2-2EV\cos\delta+V^2}}{E\cos\delta-V})}{R^2+(\frac{RE\sin\delta}{E\cos\delta-V} \pm R\frac{\sqrt{E^2-2EV\cos\delta+V^2}}{E\cos\delta-V})^2} \quad (4.117)$$

$$Q|_{X=X_{\mathrm{maxQ}}} = \frac{\pm V(E\cos\delta - V)^2}{2R(\sqrt{E^2-2EV\cos\delta+V^2} \pm E\sin\delta)} \quad (4.118)$$

When $E\cos\delta > V$ the first sign is used and $Q|_{X=X_{\mathrm{maxQ}}}$ can only take on positive values:

$$Q|_{X=X_{\mathrm{maxQ}}} = \frac{V(E\cos\delta - V)^2}{2R(\sqrt{E^2-2EV\cos\delta+V^2} + E\sin\delta)} \quad (4.119)$$

This fits well with the δ values that are known to give positive values of Q, for instance refer to Figure 4.4.

Otherwise, when $E\cos\delta < V$, the second sign is used:

$$Q|_{X=X_{\mathrm{maxQ}}} = \frac{-V(E\cos\delta - V)^2}{2R(\sqrt{E^2-2EV\cos\delta+V^2} - E\sin\delta)} \quad (4.120)$$

As the denominator is always positive:

$$\sqrt{E^2-2EV\cos\delta+V^2} - E\sin\delta \geq 0 \quad (4.121)$$

The solution can only give negative values.

$Q|_{X=X_{\mathrm{maxQ}}}$ as a function of δ is shown in Figure 4.11.

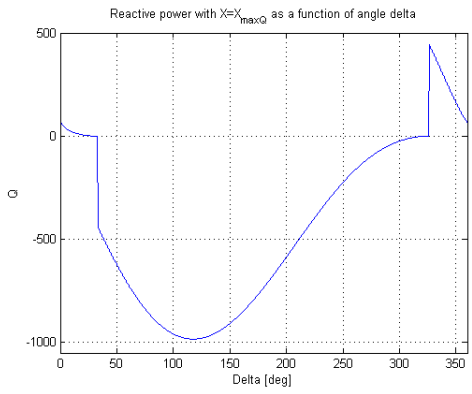

Figure 4.11: Reactive power [pu] with $X = X_{maxQ}$ as a function of δ with V=1.0 pu, E=1.2 pu, and R=0.0015 pu

It can be seen that both active power and reactive power are maximized for very small inductance values. On the other hand, these inductance values resulted in extremely high values for active and reactive power. In a circuit context this would result in damagingly high currents. The shapes of the power curves as functions of angle δ were also changed compared to the figures in section 4.1.5. The peaks of both active and reactive power were moved to lower angles. This would change the angle range defining stable operation. For reactive power it was seen that a decrease in the inductance would give a much larger value where $E\cos\delta > V$. This could give increased voltage support to the grid.

4.3 Stability Limitations

The angle stability limit in power systems is defining the stability limit [32]. That is:

$$\frac{\mathrm{d}P}{\mathrm{d}\delta} \geq 0 \tag{4.122}$$

For the power delivered to the stiff grid the angle stability limit gives:

$$\frac{\mathrm{d}P}{\mathrm{d}\delta} = \frac{\mathrm{d}}{\mathrm{d}\delta}\left(\frac{EV(R\cos\delta + X\sin\delta) - V^2R}{R^2+X^2}\right) \geq 0 \tag{4.123}$$

$$\frac{\mathrm{d}P}{\mathrm{d}\delta} = \frac{EV(X\cos\delta - R\sin\delta)}{R^2+X^2} \geq 0 \tag{4.124}$$

The angles at the stability limit are given by:

$$\delta = \arctan\left(\frac{X}{R}\right) = \arctan\left(\frac{0.25}{0.0015}\right) \tag{4.125}$$

The stable area is defined as:

$$-90.34^\circ \leq \delta \leq 89.66^\circ \tag{4.126}$$

For the power delivered from the converter the angle stability limit gives:

$$\frac{\mathrm{d}P}{\mathrm{d}\delta} = \frac{\mathrm{d}}{\mathrm{d}\delta}\left(\frac{VE(X\sin\delta - R\cos\delta) + E^2R}{R^2+X^2}\right) \geq 0 \tag{4.127}$$

$$\frac{\mathrm{d}P}{\mathrm{d}\delta} = \frac{\mathrm{d}}{\mathrm{d}\delta}\left(\frac{VE(X\cos\delta + R\sin\delta)}{R^2+X^2}\right) \geq 0 \tag{4.128}$$

The angles at the stability limit are given by:

$$\delta = \arctan\left(\frac{X}{R}\right) = \arctan\left(\frac{-0.25}{0.0015}\right) \tag{4.129}$$

The stable area is defined as:

$$-89.66^\circ \leq \delta \leq 90.34^\circ \tag{4.130}$$

The conservative solution must be chosen to ensure stability. Hence the stable area is:

$$-89.66^\circ \leq \delta \leq 89.66^\circ \tag{4.131}$$

Possible combinations of active and reactive power at different voltage levels are shown for the stiff grid in Figure 4.12 and for the converter terminal in Figure 4.13. Angle δ is limited to the values that give stable operation in the plots.

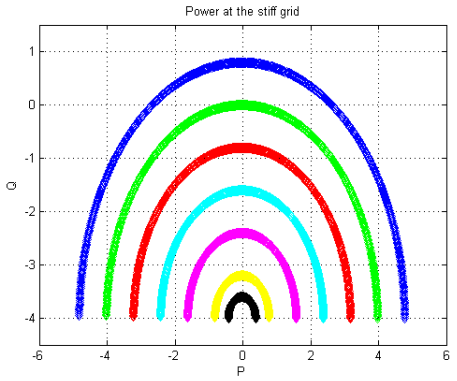

Figure 4.12: The possible combinations of active and reactive power [pu] at the stiff grid for different converter terminal voltages, where black is the lowest voltage and blue is the highest

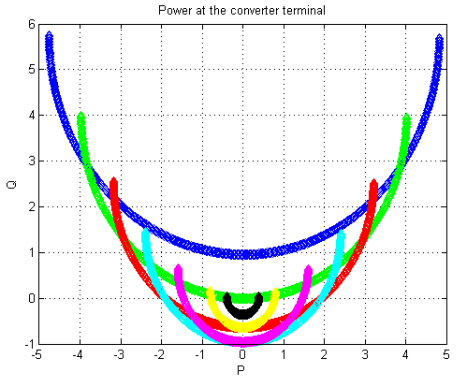

Figure 4.13: The possible combinations of active and reactive power [pu] at the converter terminal for different converter terminal voltages, where black is the lowest voltage and blue is the highest

4.4 Plots of Power at the Voltage Levels Used in the Simulations

Table 3.2 is used to find pu value of the theoretical terminal voltage for three modulation indexes. The theoretical value is given by the analytical value in the linear region and by the Matlab result in the over-modulation region. The result is shown in Table 4.2. From these voltage values, plots showing the power values as functions of angle δ are made.

Figure 4.14 and Figure 4.15 show that the active power magnitude is increasing with the terminal voltage and takes on both positive and negative values for every voltage value. The two plots are quite similar, but the active power at the converter terminal is slightly higher than the active power at the stiff grid for every angle δ. The two plots have zero crossing at different angle δ values. At the converter terminal, the zero crossing takes place for an angle larger than 180°, while at the stiff grid the angle is smaller than 180°.

Figure 4.16 and Figure 4.17 show that the magnitude of the reactive power is increasing with the terminal voltage. At the stiff grid, the reactive power is only positive for angle δ values close to 0° and larger terminal voltages. This is in accordance with the results found in section 4.1.6. The reactive power at the converter terminal is mostly positive. Comparing the two curves shows that a large amount of reactive power is consumed between the converter terminal and the stiff grid. This amount is increasing with terminal voltage.

Figure 4.18 indicates the possible operation states with $m = 1.0$. It can be seen that the values for active and reactive power cannot be chosen arbitrary, as they both depend on angle δ. However, positive and negative reactive power can be combined with either positive or negative active power at the stiff grid.

Figure 4.19 shows that the apparent power at the converter terminal is larger than the apparent power at the stiff grid. The difference is largest with angle δ close to 180°, where the apparent power is more affected by the reactive power value than the active power value, as the value for active power is quite small.

Table 4.2: Modulation index and theoretical terminal voltage

Modulation index	Theoretical voltage value [kV]	Theoretical voltage value [pu]
0.8	293.94	0.98
1.0	367.42	1.22
1.2	394.98	1.32

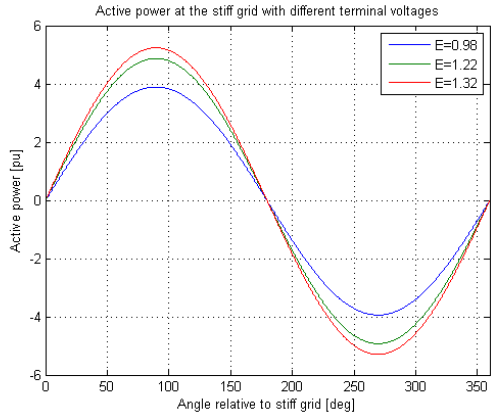

Figure 4.14: Active power [pu] at the stiff grid with terminal voltages corresponding to $m = 0.8$, $m = 1.0$, and $m = 1.2$

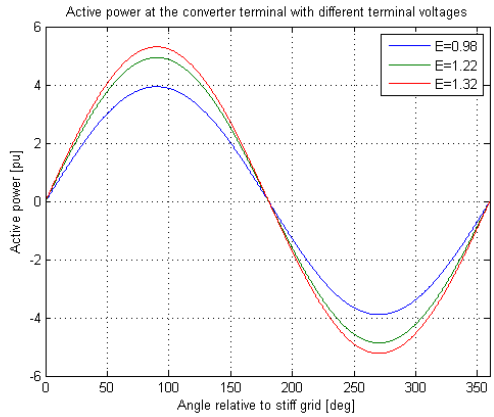

Figure 4.15: Active power [pu] at the converter terminal with terminal voltages corresponding to $m = 0.8$, $m = 1.0$, and $m = 1.2$

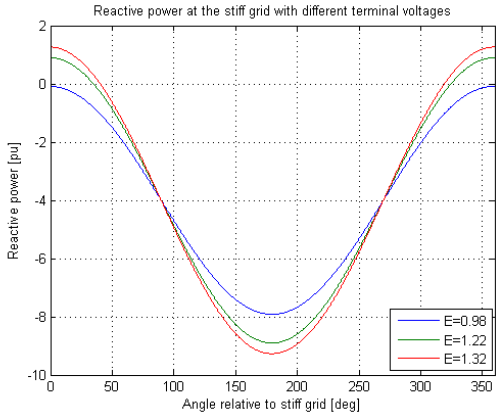

Figure 4.16: Reactive power [pu] at the stiff grid with terminal voltages corresponding to $m = 0.8$, $m = 1.0$, and $m = 1.2$

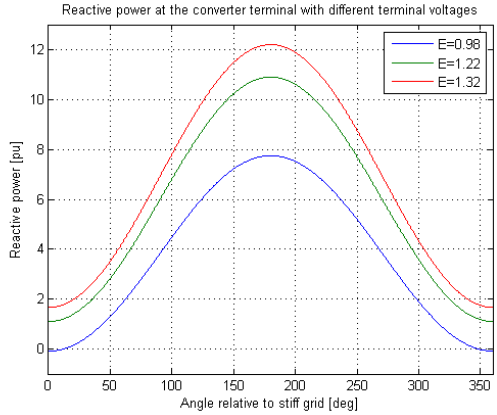

Figure 4.17: Reactive power [pu] at the converter terminal with terminal voltages corresponding to $m = 0.8$, $m = 1.0$, and $m = 1.2$

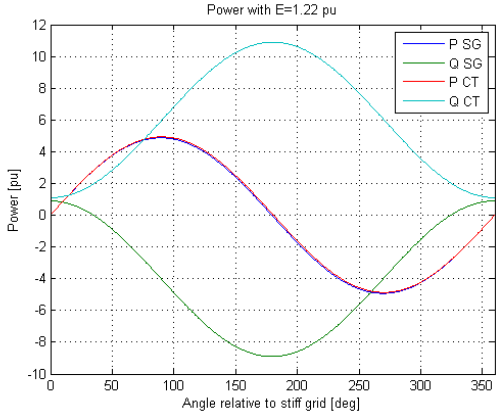

Figure 4.18: Active power at the stiff grid, reactive power at the stiff grid, active power at the converter terminal, and reactive power at the converter terminal, all in pu, with terminal voltages corresponding $m = 1.0$

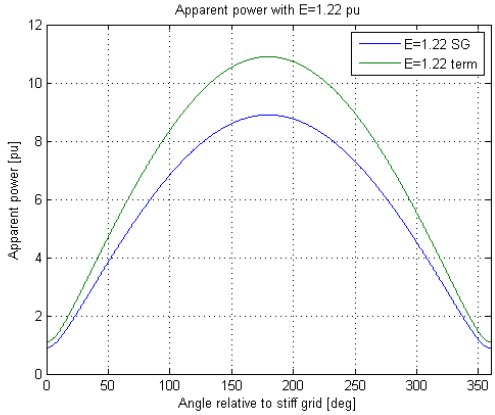

Figure 4.19: Apparent power at the stiff grid and the converter terminal, both in pu, with terminal voltages corresponding $m = 1.0$

Figures 4.20 and 4.21 show the possible combinations of active and reactive power with $-89.66° \leq \delta \leq 89.66°$ for the stiff grid and converter terminal respectively.

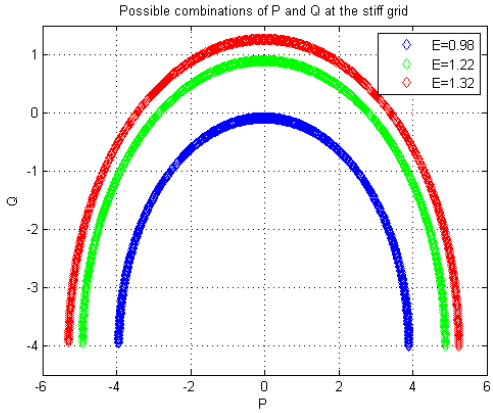

Figure 4.20: Possible combinations of active and reactive power [pu] at the stiff grid with terminal voltages corresponding to $m = 0.8$, $m = 1.0$, and $m = 1.2$ with $-89.66° \leq \delta \leq 89.66°$

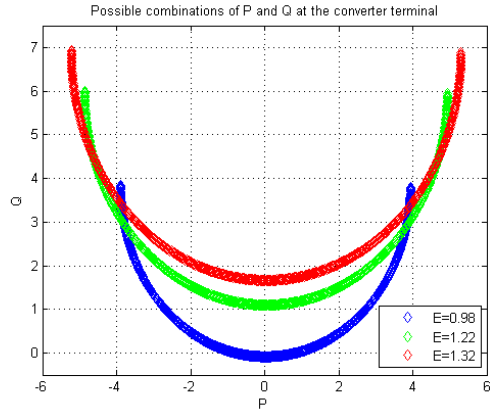

Figure 4.21: Possible combinations of active and reactive power [pu] at the converter terminal with terminal voltages corresponding to $m = 0.8$, $m = 1.0$, and $m = 1.2$ with $-89.66° \leq \delta \leq 89.66°$

Chapter 5

Control System Deduction and Tuning

5.1 The System Equations

5.1.1 The Mathematical Model

Parts of the mathematical model and control system structure are described in the specialization project [5], but important conclusions are included here for completeness.

Figure 5.1 shows a phase equivalent for the MMC circuit, the filter consist-

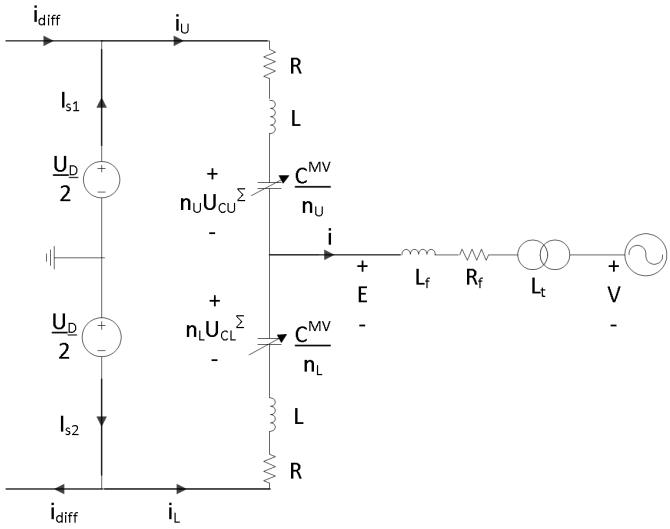

Figure 5.1: The MMC circuit and the connection to the stiff grid

Table 5.1: The parameters used in the mathematical model

U_D	DC pole to pole voltage
E	Converter terminal voltage
$U_{CU}^{\sum}$	Sum of capacitor voltages, upper multivalve
$U_{CL}^{\sum}$	Sum of capacitor voltages, lower multivalve
$e_V = \frac{n_L U_{CL}^{\sum} - n_U U_{CU}^{\sum}}{2}$	Inner alternating converter voltage
i_U	Current in the upper multivalve
i_L	Current in the lower multivalve
$i = i_U + i_L$	Output AC current
$i_{\text{diff}} = \frac{i_U - i_L}{2}$	Circulating current
n_U	Insertion index, upper multivalve, on interval [0,1]
n_L	Insertion index, lower multivalve, on interval [0,1]

ing of the inductance L_f and the resistance R_f, the transformer modelled as the inductance L_t, and the stiff grid. This corresponds to the case circuit in Figure 1.1.

E is the voltage at the converter terminal and V the voltage at the stiff grid. The current flowing from the converter toward the stiff grid is denoted i.

The continuous model is developed assuming infinite switching frequency in the converter and infinitive number of submodules per multivalve.

The converter consists of N submodules per multivalve, and $n_m = 0$ means that all the N submodules in multivalve m are bypassed, while $n_m = 1$ means that all N submodules are inserted. The available voltage in multivalve m, i.e. sum of all the inserted capacitor voltages, is given as:

$$U_{Cm} = n_m U_{\text{Cm}}^{\sum} \tag{5.1}$$

where $u_{\text{Cm}}^{\sum}$ is the total capacitor voltage in the multivalve and m=U for upper multivalve and m=L for lower multivalve.

The sum of the two insertion indexes should be kept equal to 1, so an insertion in one multivalve corresponds to a bypassing in the other multivalve in the phase, expressed mathematically as:

$$n_U + n_L = 1 \tag{5.2}$$

There are six currents in Figure 5.1. $I_{s1} = I_{s2} = \frac{i}{2}$ are the balanced currents delivered from the DC side. The circulating current, i_{diff}, represents all the imbalances in the phase. The multivalve currents are composed from these currents as $i_U = I_{s1} + i_{\text{diff}}$ for the upper multivalve and $i_L = I_{s2} - i_{\text{diff}}$ for the lower multivalve.

Using Kirchhoff's voltage law in Fingure 5.1:

$$\frac{U_D}{2} - Ri_U - L\frac{\mathrm{d}i_U}{\mathrm{d}t} - n_U U_{CU}^{\sum} = E \tag{5.3}$$

$$-\frac{U_D}{2} - Ri_L - L\frac{\mathrm{d}i_L}{\mathrm{d}t} + n_L U_{CL}^{\sum} = E \tag{5.4}$$

Combining Equations 5.3 and 5.4:

$$n_L U_{CL}^{\sum} - n_U U_{CU}^{\sum} - R(i_U + i_L) + L\frac{\mathrm{d}}{\mathrm{d}t}(i_U + i_L) = 2E \tag{5.5}$$

Using that $i_U + i_L = i$ and that $e_V = \frac{1}{2}(n_L U_{CL}^{\sum} - n_U U_{CU}^{\sum})$:

$$e_V - \frac{R}{2}i - \frac{L}{2}\frac{\mathrm{d}i}{\mathrm{d}t} = E \tag{5.6}$$

Calculating the voltage drop between the converter and the stiff grid:

$$V = E - R_f i - (L_f + L_t)\frac{\mathrm{d}i}{\mathrm{dt}} \tag{5.7}$$

The total system description is given as:

$$e_V - (\frac{R}{2} + R_f)i - (\frac{L}{2} + L_f + L_t)\frac{\mathrm{d}i}{\mathrm{d}t} = V \tag{5.8}$$

To simplify the notation, R' and L' are defined:

$$R' = \frac{R}{2} + R_f \tag{5.9}$$

$$L' = \frac{L}{2} + L_f + L_t \tag{5.10}$$

e_v can be written as a function of the currents using the expression for voltage across a capacitor:

$$e_V = \frac{1}{2}(n_L U_{CL}^{\sum} - n_U U_{CU}^{\sum}) = \frac{1}{2}([-\frac{n_L}{C^{\mathrm{MV}}}\int_{t_0}^{t} i_L \mathrm{d}\tau + n_L(t_0)U_{CL}^{\sum}(t_0)] - [\frac{n_U}{C^{\mathrm{MW}}}\int_{t_0}^{t} i_U \mathrm{d}\tau + n_U(t_0)U_{CU}^{\sum}(t_0)]) \tag{5.11}$$

Using that $n_U + n_L = 1$, $i_L + i_U = i$, and $i_U - i_L = 2i_{\mathrm{diff}}$:

$$e_V = \frac{1}{2}(-\frac{n_L + n_U}{C^{\mathrm{MV}}}\int_{t_0}^{t} \frac{i}{2}\mathrm{d}\tau + \frac{n_L - n_U}{C^{\mathrm{MV}}}\int_{t_0}^{t} i_{\mathrm{diff}}\mathrm{d}\tau + n_L(t_0)U_{CL}^{\sum}(t_0) - n_U(t_0)U_{CU}^{\sum}(t_0)) \tag{5.12}$$

$$e_V = \frac{1}{2}(-\frac{1}{C^{\mathrm{MV}}}\int_{t_0}^{t} \frac{i}{2}\mathrm{d}\tau + \frac{n_L - n_U}{C^{\mathrm{MV}}}\int_{t_0}^{t} i_{\mathrm{diff}}\mathrm{d}\tau + 2e_V(t_0)) \tag{5.13}$$

Assuming a well-functioning control system giving $i_{\mathrm{diff}} \approx 0$:

$$e_V - e_V(t_0) = -\frac{1}{4C^{\mathrm{MV}}} \int_{t_0}^{t} i \mathrm{d}\tau \tag{5.14}$$

$$i = -4C^{\mathrm{MV}} \frac{\mathrm{d}}{\mathrm{dt}} e_V \tag{5.15}$$

5.1.2 The Circuit Description in the DQ Reference Frame

Equations 5.8 and 5.15 can be expressed in the dq reference frame using the transformation described in Appendix A. The equations are developed for one phase equivalent, and the relationships are valid for all three phases. T is the transformation matrix given by Equation A.1. The transformation of the voltage drop across the inductance is given by Equation A.25. The same relationship is valid for the derivative of the voltage in Equation 5.15.

$$\begin{bmatrix} v_d \\ v_q \\ v_0 \end{bmatrix} = T \begin{bmatrix} V_a \\ V_b \\ V_c \end{bmatrix} = T \begin{bmatrix} e_{\mathrm{Va}} \\ e_{\mathrm{Vb}} \\ e_{\mathrm{Vc}} \end{bmatrix} - R'T \begin{bmatrix} i_a \\ i_b \\ i_c \end{bmatrix} - L'T \begin{bmatrix} \frac{\mathrm{d}i_a}{\mathrm{dt}} \\ \frac{\mathrm{d}i_b}{\mathrm{dt}} \\ \frac{\mathrm{d}i_c}{\mathrm{dt}} \end{bmatrix} \tag{5.16}$$

$$\begin{bmatrix} v_d \\ v_q \\ v_0 \end{bmatrix} = \begin{bmatrix} e_{\mathrm{Vd}} \\ e_{\mathrm{Vq}} \\ e_{\mathrm{V0}} \end{bmatrix} - R' \begin{bmatrix} i_d \\ i_q \\ i_0 \end{bmatrix} - L' \begin{bmatrix} \frac{\mathrm{d}i_d}{\mathrm{dt}} - \omega i_q \\ \frac{\mathrm{d}i_q}{\mathrm{dt}} + \omega i_d \\ 0 \end{bmatrix} \tag{5.17}$$

$$\begin{bmatrix} i_d \\ i_q \\ i_0 \end{bmatrix} = T \begin{bmatrix} i_a \\ i_b \\ i_c \end{bmatrix} = -4C^{\mathrm{MV}} T \begin{bmatrix} \frac{\mathrm{d}e_{\mathrm{Va}}}{\mathrm{dt}} \\ \frac{\mathrm{d}e_{\mathrm{Vb}}}{\mathrm{dt}} \\ \frac{\mathrm{d}e_{\mathrm{Vc}}}{\mathrm{dt}} \end{bmatrix} \tag{5.18}$$

$$\begin{bmatrix} i_d \\ i_q \\ i_0 \end{bmatrix} = -4C^{\mathrm{MV}} \begin{bmatrix} \frac{\mathrm{d}e_{\mathrm{Vd}}}{\mathrm{dt}} - \omega e_{\mathrm{Vq}} \\ \frac{\mathrm{d}e_{\mathrm{Vq}}}{\mathrm{dt}} + \omega e_{\mathrm{Vd}} \\ 0 \end{bmatrix} \tag{5.19}$$

v_d and v_q are the d and q components of the voltage at the stiff grid, V. i_d and i_q are the d and q components of the current i. Also e_V is decomposed into d and q components, e_{Vd} and e_{Vq}.

Equation 5.17 can be rewritten in the Laplace domain:

$$v_d = e_{\mathrm{Vd}} - (R' + sL')i_d + L'\omega i_q \tag{5.20}$$

$$v_q = e_{\mathrm{Vq}} - (R' + sL')i_q - L'\omega i_d \tag{5.21}$$

Equation 5.19 can be rewritten in the Laplace domain:

$$i_d = -4C^{\mathrm{MV}}(se_{\mathrm{Vd}} - \omega e_{\mathrm{Vq}}) \tag{5.22}$$

$$i_q = -4C^{\mathrm{MV}}(se_{\mathrm{Vq}} + \omega e_{\mathrm{Vd}}) \tag{5.23}$$

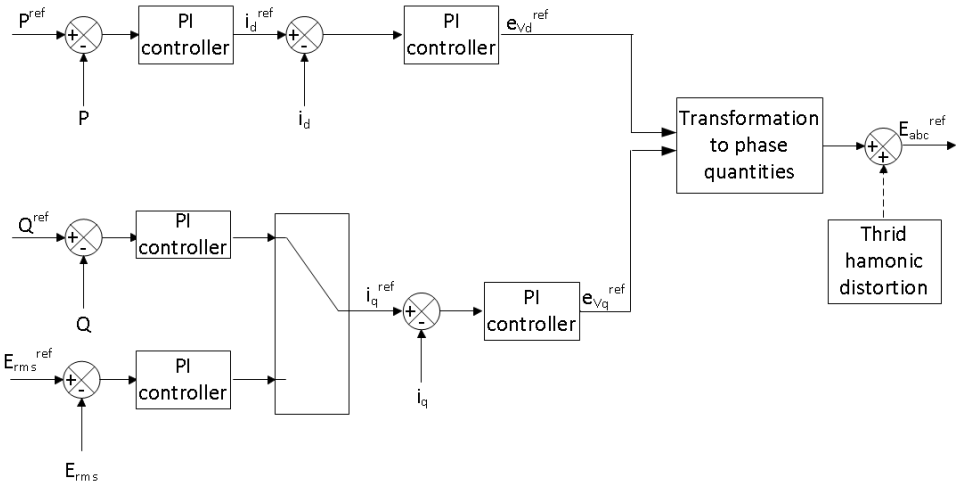

Figure 5.2: The stucture of the upper level control system

5.2 The Control Loops

The control system is made with a cascaded structure. The inner loops are the current controllers, while the outer loops can control active power and either reactive power or the rms value of the converter terminal voltage. The control system is done in the dq reference frame to enable independent control of active power and reactive power, and enable the use of PI controllers with zero steady-state error. The structure of the upper level control system is shown in Figure 5.2.

The references for active and reactive power are given for the point at the stiff grid. This requires that measurements are done at this place. If the point is far away from the converter in distance, the signal transmission can be challenging. The reference for rms value is given for the converter terminal.

5.2.1 The Current Control Loops

The current control loops will consist of a PI controller and blocks representing the process. The process consist of two elements; a time delay representing the converter and the electrical system described by Equations 5.20 and 5.21 for the d and q axis respectively. Into the PI controller goes the error between the reference signal and the feedback signal from the process blocks. The process blocks must therefore generate a value for the current that can be used as feedback signal. Each part of the control loops is described below.

The PI Controller The transfer function for the PI controller is given as:

$$H_{Cc}(s) = K_{pc}\frac{1 + T_{ic}s}{T_{ic}s} \tag{5.24}$$

where K_{pc} is the proportional gain and T_{ic} is the integral time constant.

The Converter The converter is modelled as a time delay. The time delay is calculated as 1.5 times the effective switching period. This calculation is done assuming that the switching frequency equals the sampling frequency, and considering the worst case [33].

If T_a is the time delay in the converter, the converter transfer function can be written as:

$$H_{\text{conv}}(s) = \frac{1}{1 + T_a s} \tag{5.25}$$

As each phase has $2N$ submodules switched at a frequency f_{carrier}, $T_a = \frac{1.5}{2N \cdot f_{\text{carrier}}}$ [33]. $f_{\text{carrier}} = 150$ Hz is a typical value [13]. A DC voltage between ± 200 kV and ± 400 kV gives N between 24 and 48 approximately. These values give T_a between $1 \cdot 10^{-4}$ and $2 \cdot 10^{-4}$. The case in the simulation model with $N = 38$ gives $T_a = 1.32 \cdot 10^{-4}$.

The Electrical System For simplification Equations 5.20 and 5.21 are written together:

$$v_{d/q} = e_{\text{Vd/q}} - (R' + sL')i_{d/q} \pm L'\omega i_{q/d} \tag{5.26}$$

As the electrical system model must generate a value for the current that can be used as feedback signal, Equation 5.26 is solved for $i_{d/q}$:

$$i_{d/q} = \frac{e_{\text{Vd/q}} - v_{d/q} \pm L'\omega i_{q/d}}{R' + sL'} \tag{5.27}$$

The inner alternating voltage, $e_{\text{Vd/q}}$, is the resulting signal from the converter block. $v_{d/q}$ and $L'\omega i_{q/d}$ are regarded as disturbances. To suppress the effect of the disturbances, feed-forward is used to manipulate the signal going into the converter block. This is beneficial due to the time delay in the process model delaying the feedback.

The transfer function for the electrical system is:

$$H_{el}(s) = \frac{1}{R' + sL'} = \frac{\frac{1}{R'}}{1 + s\tau_{el}} \tag{5.28}$$

where $\tau_{el} = \frac{L'}{R'}$.

The values for R' and L' are calculated using the values from the simulation model given in Appendix B, except for the multivalve resistance. Antonopoulos [34] assumes a resistance of 0.01Ω per submodule and this value will also be used here. With 38 submodules per multivalve this gives $R = 0.38\Omega = 0.0025$ pu. The filter resistance is $R_f = 0.0015$ pu and hence $R' = \frac{0.0025}{2} + 0.0015 = 0.00275$ pu. In the Thévenin equivalent in the simulation model each multivalve has a smoothing inductance of L_{MW}=0.01432 H = 0.030 pu. The filter inductance is $L_f = 0.15$ pu and the transformer leakage inductance is $L_t = 0.10$ pu. This gives $L' = \frac{0.030}{2} + 0.15 + 0.10 = 0.265$ pu.

The time constant τ_{el} is calculated based on the ratio of the physical values. That is: $\tau_{el} = \frac{L'}{R'} = \frac{L'_{pu}\frac{Z_{\text{base}}}{\omega_{\text{base}}}}{R'_{pu}Z_{\text{base}}} = \frac{L'_{pu}}{R'_{pu}\omega_{\text{base}}} = 0.3067$. The gain in the electrical system transfer function is $\frac{1}{R'} = 3633.64$ pu.

Tuning of the Current Control Loops

Tuning of the current control loops is done using modulus optimum. The largest time constant is identified as the time constant in the block representing the electrical system. This pole will therefore be cancelled by the zero in the PI controller. The proportional gain will be given as $K_{pc} = \frac{\tau_{el}}{2T_a\frac{1}{R'}} = 3.205$. The resulting open loop transfer function is:

$$H_{c,OL}(s) = H_{Cc}(s)H_{\text{conv}}(s)H_{el}(s) = K_{pc}\frac{1+T_{ic}s}{T_{ic}s}\frac{1}{1+T_as}\frac{\frac{1}{R'}}{1+s\tau_{el}} = \frac{\tau_{el}}{2T_a\frac{1}{R'}}\frac{1+\tau_{el}s}{\tau_{el}s}\frac{1}{1+T_as}\frac{\frac{1}{R'}}{1+s\tau_{el}} = \frac{1}{2T_as(1+T_as)} \approx \frac{1}{2T_as} \tag{5.29}$$

The closed loop transfer function is:

$$H_{c,CL}(s) = \frac{1}{1+2T_as(1+T_as)} \approx \frac{1}{1+2T_as} \tag{5.30}$$

The bode plots for the open current control loops in the original and simplified form are shown in Figure 5.3. At low frequencies at behaviours are quite similar, and the simplified loop is therefore used in the following. A difference is however

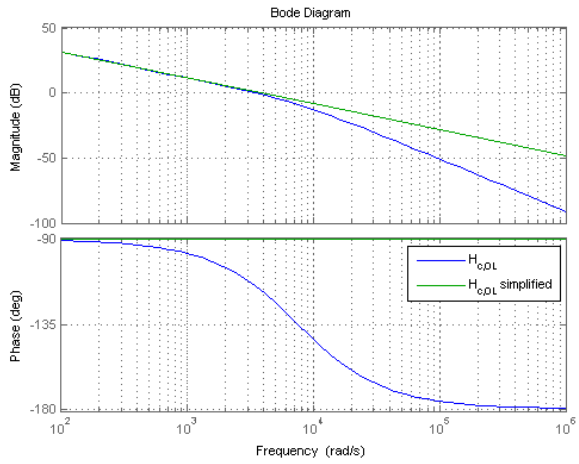

Figure 5.3: The bode plots for the open current loops, original and simplified.

the phase margins. With the simplified loop, the phase is constant at $-90°$ and the phase margin is therefore $90°$. With the proper expression the phase margin is $65.5°$. The crossover frequency is somewhat increased when the simplified expression is used.

Calculation of the Feed-forward Transfer Function

The disturbances $v_{d/q}$ and $L'\omega i_{q/d}$, respectively $-v_d + L'\omega i_q$ in the d axis and $-v_q - L'\omega i_d$ in the q axis, are considered in the same way as the general disturbance v in Figure 2.2 in section 2.3.2.

In this case $H_{u1}(s)$ in Equation 2.8 corresponds to the converter model that is:

$$H_{u1}(s) = H_{\text{conv}}(s) = \frac{1}{1 + T_a s} \tag{5.31}$$

And the ideal feed-forward is:

$$H_{fi}(s) = -\frac{1}{H_{u1}(s)} = -(1 + T_a s) \tag{5.32}$$

This is an unlimited differentiation effect, which is not possible to realize practically. It would also lead to high frequency noise in the measurement [7].

A realistic feed-forward transfer function could be:

$$H_f(s) = -\frac{1 + T_a s}{1 + \alpha T_a s} \tag{5.33}$$

where $\alpha < 1$.

The static feed-forward is $H_f(0) = -1$. This equals the ideal static feed-forward, and it can be seen that a constant disturbance will be perfectly suppressed.

To determine the value of α, the regulation ratio, $N(s)$, and the feed-forward ratio, $L(s)$, are calculated and the magnitudes are plotted as functions of frequency with different values of α.

$$L(s) = H_f(s)H_{u1}(s) + 1 = -\frac{1 + T_a s}{1 + \alpha T_a s}\frac{1}{1 + T_a s} + 1 = \frac{\alpha T_a s}{1 + \alpha T_a s} \tag{5.34}$$

$$N(s) = \frac{1}{1 + H_{c,OL}} = \frac{2T_a s(1 + T_a s)}{1 + 2T_a s(1 + T_a s)} \tag{5.35}$$

Figure 5.4 shows that for instance $\alpha = 0.1$ gives an improvement for the system.

The Current Control Block Diagram

The block diagram for the current control loops is shown in Figure 5.5.

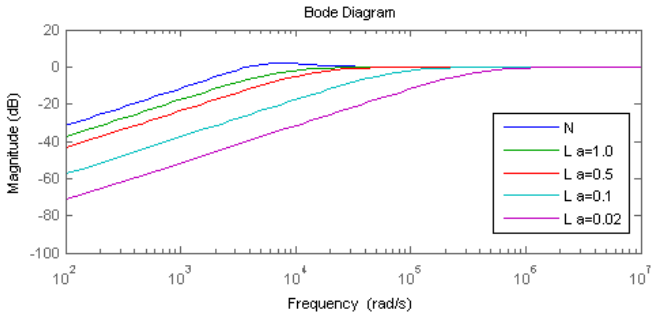

Figure 5.4: Current loops, feed-forward: |N(s)| and |L(s)| with different values of α: α=1.0, α=0.5 α=0.1, and α=0.02

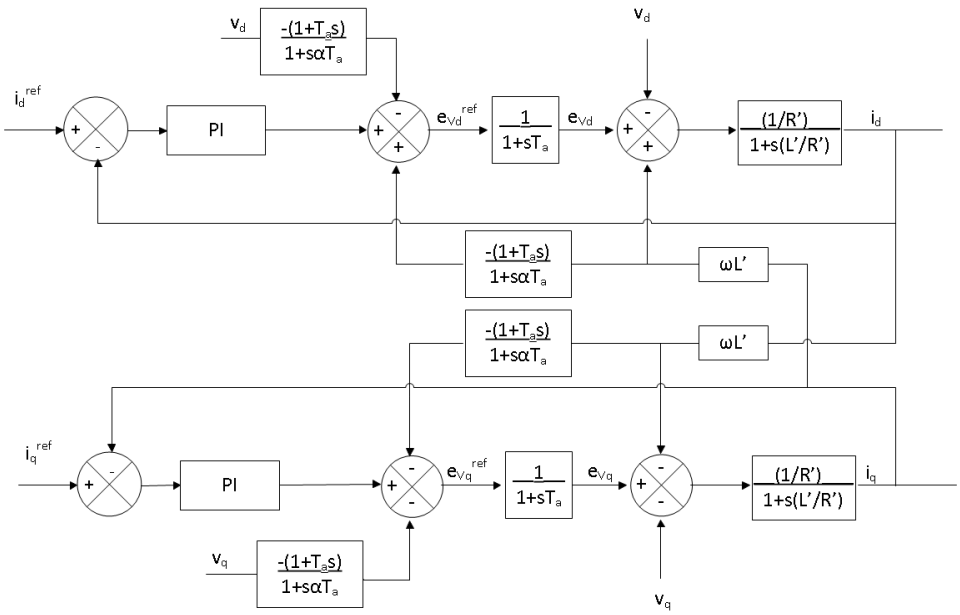

Figure 5.5: Block digram for the current control loops

5.2.2 Active and Reactive Power Control Loops

The first block in the power control loops is a PI controller generating a current reference. The current reference is fed into the closed current loop. Equation 2.3 for active power and Equation 2.4 for reactive power are used to generate a power value from the current value and this power value is used as feedback signal. Each part of the control loops is described below.

The PI Controller The transfer function for the PI controller is given as:

$$H_{CP}(s) = K_{pP}\frac{1+T_{iP}s}{T_{iP}s} \tag{5.36}$$

where K_{pP} is the proportional gain and T_{iP} is the integral time constant.

The Closed Loop Current Controller The PI controller generates a current reference. The closed loop current controller is used to find the resulting current value. The transfer function is given as:

$$H_{c,CL}(s) = \frac{1}{1+2T_a s} \tag{5.37}$$

where T_a is the time delay in the converter. The case in the simulation model with $N = 38$ gives $T_a = 1.32 \cdot 10^{-4}$.

The Calculation of Power Based on the current value given from the closed loop current controller, the power value can be calculated with a gain block. Using that:

$$P = \frac{3}{2}v_d i_d \tag{5.38}$$

$$Q = \frac{3}{2}v_d i_q \tag{5.39}$$

the gain will be given as $\frac{3}{2}v_d$ for both active and reactive power. Hence the transfer function is given as:

$$H_{pow}(s) = \frac{3}{2}v_d \tag{5.40}$$

In the general case v_d is a parameter, and the gain will not be constant. In this case v_d is d component of the stiff grid voltage. As the stiff grid defines the angle of the rotating dq reference system and always has voltage with magnitude 1.0 pu, v_d will be constantly equal 1.0.

Tuning of the Power Control Loops

The resulting open loop transfer function for the power control loops is:

$$H_{P,OL}(s) = H_{CP}(s)H_{c,CL}(s)H_{pow}(s) = K_{pP}\frac{1+T_{iP}s}{T_{iP}s}\frac{1}{1+2T_a s}\frac{3}{2}v_d \tag{5.41}$$

A PI controller for system with transfer function:

$$\frac{K}{1+Ts} \tag{5.42}$$

should have the parameters $K_p = \frac{1}{K}T\omega_c$ and $T_i = T$ where ω_c is the desired bandwidth [7]. In this case $T = 2T_a$ and $K = \frac{3}{2}v_d$.

Accordingly $K_{pP} = \frac{1}{\frac{3}{2}v_d}2T_a\omega_c = \frac{4T_a}{3v_d}\omega_c$ and $T_{iP} = 2T_a$. Using that $v_d = 1.0$ gives $K_{pP} = \frac{4T_a}{3}\omega_c$. When using a cascaded structure, the inner loop should always be faster than the outer loop. In Figure 5.3 it can be seen that the crossover frequency for the current control loops approximately $\frac{1}{2T_a}$. The bandwidth for the outer loops is chosen to be an order of magnitude smaller, that is $\omega_c = \frac{1}{20T_a}$. This gives a proportional gain of $K_{pP} = \frac{4T_a}{3}\frac{1}{20T_a} = \frac{1}{15} = 0.067$.

Insertion into the open loop transfer function gives:

$$H_{P,OL}(s)\frac{1}{15}\frac{1+2T_as}{2T_as}\frac{1}{1+2T_as}\frac{3}{2} = \frac{1}{20T_as} = \frac{1}{20T_as} \tag{5.43}$$

The bode plot for the open loop transfer function is shown in Figure 5.6.

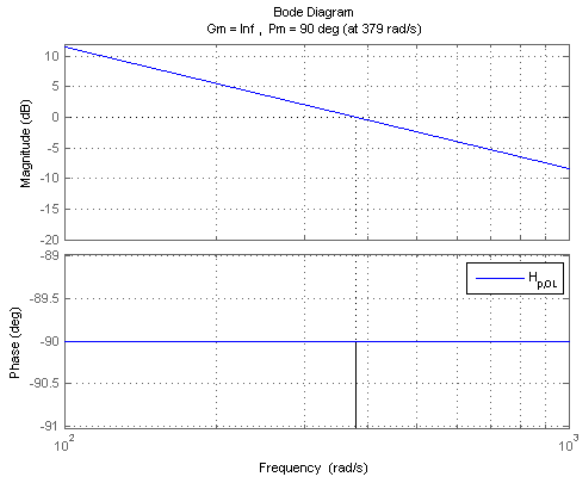

Figure 5.6: The bode plot for the open power loops

The Active Power Control Block Diagram

Due to the similarity of the block diagrams for active and reactive power, only the diagram for active power is shown here. Active power has the same relationship to i_d as reactive power has to i_q. The two control loops have the same structures and parameters as long as the control loops for i_d and i_q have the same structures and parameters. Where the active power control loop has the closed current loop in the d axis, the reactive power will have the closed current loop in the q axis.

The block diagram for the active power control loop is shown in Figure 5.7.

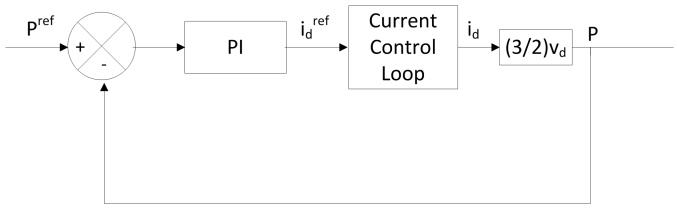

Figure 5.7: Block diagram for the active power control loop

5.2.3 RMS Value Control Loop

The first block in the rms value control loop is a PI controller generating a current reference for i_q. The current reference is fed into the closed current loop. Equation 5.23 is used to calculate a value for e_{Vq} based on the current value from the closed current loop. The rms voltage value is calculated by Equation 2.5 and is used as feedback signal. Each part of the control loop is described below.

The PI Controller The transfer function for the PI controller is given as:

$$H_{CV}(s) = K_{pV}\frac{1 + T_{iV}s}{T_{iV}s} \tag{5.44}$$

where K_{pV} is the proportional gain and T_{iV} is the integral time constant.

The Closed Loop Current Controller The PI controller generates a current reference. The closed loop current controller is used to find the resulting current value. The transfer function is given as:

$$H_{c,CL}(s) = \frac{1}{1 + 2T_a s} \tag{5.45}$$

where T_a is the time delay in the converter. The case in the simulation model with $N = 38$ gives $T_a = 1.32 \cdot 10^{-4}$.

The Calculation of Q Axis Voltage Based on the current value given from the closed loop current controller, the voltage value e_{Vq} can be calculated using Equation 5.23:

$$e_{\mathrm{Vq}} = \frac{1}{s}\left(\frac{i_q}{-4C^{\mathrm{MV}}} - \omega e_{\mathrm{Vd}}\right) \tag{5.46}$$

ωe_{Vd} will be regarded as a disturbance and a feed-forward is used to suppress the effect of this disturbance.

The transfer function for the voltage calculation is:

$$H_{volt}(s) = \frac{-1}{4C^{\mathrm{MW}}s} \tag{5.47}$$

The capacitance per cell in the simulation model is found in Appendix B as 8867 μF. C^{MW} is given as:

$$C^{\mathrm{MW}} = \frac{C_{\mathrm{cell}}}{N} = \frac{8867\mu\mathrm{F}}{38} = 223.3\mu\mathrm{H} = 1.11 \cdot 10^{-4}\mathrm{pu} \tag{5.48}$$

The Calculation of RMS Value The rms value is calculated using Equation 2.5:

$$E_{\mathrm{rms}} = \sqrt{\frac{e_{Vd}^2 + e_{Vq}^2}{2}} \tag{5.49}$$

This function is not linear and will be regarded as a constant gain in the tuning process.

The transfer function used in the tuning process will be:

$$H_{rms}(s) = K_{\mathrm{RMS}} \tag{5.50}$$

where $K_{\mathrm{RMS}} \geq 0$ is the constant modelling the function used to calculate the rms value. The tuning will only be valid where the value of $H_{rms}(s)$ is close to the value assumed in the tuning process. Here the value of K_{RMS} will be assumed to be $\frac{1}{\sqrt{2}}$ pu as this is the pu value of the rms voltage.

Tuning of the RMS Value Control Loop

The resulting open loop transfer function for the rms value control loop is:

$$H_{V,OL} = H_{CV}(s)H_{c,CL}(s)H_{volt}(s)H_{rms}(s) = K_{pV}\frac{1+T_{iV}s}{T_{iV}s}\frac{1}{1+2T_as}\frac{-1}{4C^{\mathrm{MW}}s}K_{\mathrm{RMS}} \tag{5.51}$$

The loop can be tuned with symmetric optimum. The integral time is found as $T_{iV} = 4 \cdot 2T_a = 8T_a$ and the proportional gain is $K_{pV} = \frac{4C^{\mathrm{MV}}}{2(-K_{\mathrm{RMS}})2T_a} = \frac{-C^{\mathrm{MV}}}{K_{\mathrm{RMS}}T_a}$. The resulting transfer function is:

$$H_{V,OL} = \frac{-C^{\mathrm{MV}}}{K_{\mathrm{RMS}}T_a}\frac{1+8T_as}{8T_as}\frac{1}{1+2T_as}\frac{-1}{4C^{\mathrm{MW}}s}K_{\mathrm{RMS}} = \frac{1+8T_as}{32T_a^2s^2(1+2T_as)} \tag{5.52}$$

The bode plot for the open loop transfer function is shown in Figure 5.8. The phase margin is only 36.9°, but as the symmetric optimum is used to tune this loop, the phase margin is already maximized.

Calculation of the Feed-forward Transfer Function

The disturbance $-\omega e_{\mathrm{Vd}}$ is cancelled by adding a feed-forward signal between the PI controller and the closed current loop.

The blocks between the feed-forward summation point and the disturbance summation point are the closed current loop and a gain. Considering Figure 2.2

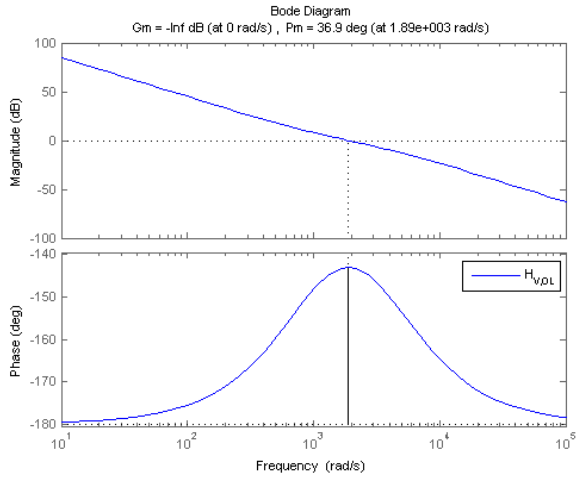

Figure 5.8: The bode plot for the open rms value loop

$H_{u1}(s) = H_{c,CL}(s)\frac{-1}{4C^{\mathrm{MV}}} = \frac{-1}{4C^{\mathrm{MV}}(1+2T_a s)}$. The ideal feed-forward transfer function is:

$$H_{fi}(s) = -\frac{1}{H_{u1}(s)} = 4C^{\mathrm{MV}}(1+2T_a s) \tag{5.53}$$

To avoid an unlimited differentiation effect, the feed-forward transfer function is manipulated and a denominator is included:

$$H_f(s) = \frac{4C^{\mathrm{MV}}(1+2T_a s)}{1+\alpha 2T_a s} \tag{5.54}$$

where $\alpha < 1$. The static feed-forward, $H_f(0) = 4C^{\mathrm{MV}}$, equals the ideal static feed-forward.

The value of α must be determined. The regulation ratio, N(s), is calculated as described in section 2.3.2:

$$N(s) = \frac{1}{1+HV,OL} = \frac{1}{1+\frac{1+8T_a s}{32T_a^2 s^2(1+2T_a s)}} = \frac{32T_a^2 s^2(1+2T_a s)}{32T_a^2 s^2(1+2T_a s)+1+8T_a s} \tag{5.55}$$

The feed-forward ratio, L(s), is given as:

$$L(S) = H_f(s)H_{u1}(s)+1 = \frac{4C^{\mathrm{MV}}(1+2T_a s)}{1+\alpha 2T_a s}\frac{-1}{4C^{\mathrm{MV}}(1+2T_a s)}+1 = \frac{-1}{1+\alpha 2T_a s}+1 = \frac{\alpha 2T_a s}{1+\alpha 2T_a s} \tag{5.56}$$

|N(s)| and |L(s)| with different values for α are plotted in Figure 5.9. The Figure indicates that for instance $\alpha = 0.1$ would give an improvement for the system.

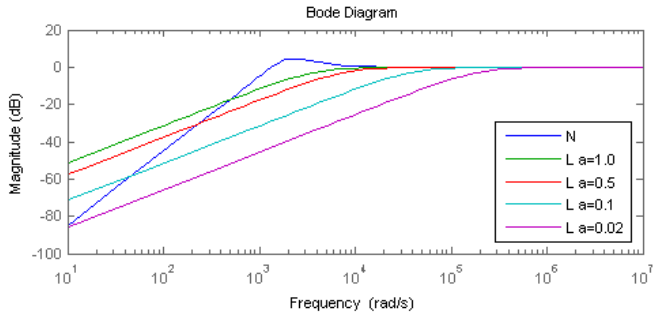

Figure 5.9: Rms value loop, feed-forward:|N(s)| and |L(s)| with different values of α: α=1.0, α=0.5 α=0.1, and α=0.02

The RMS Value Control Block Diagram

The block diagram for the rms value control loop is shown in Figure 5.10.

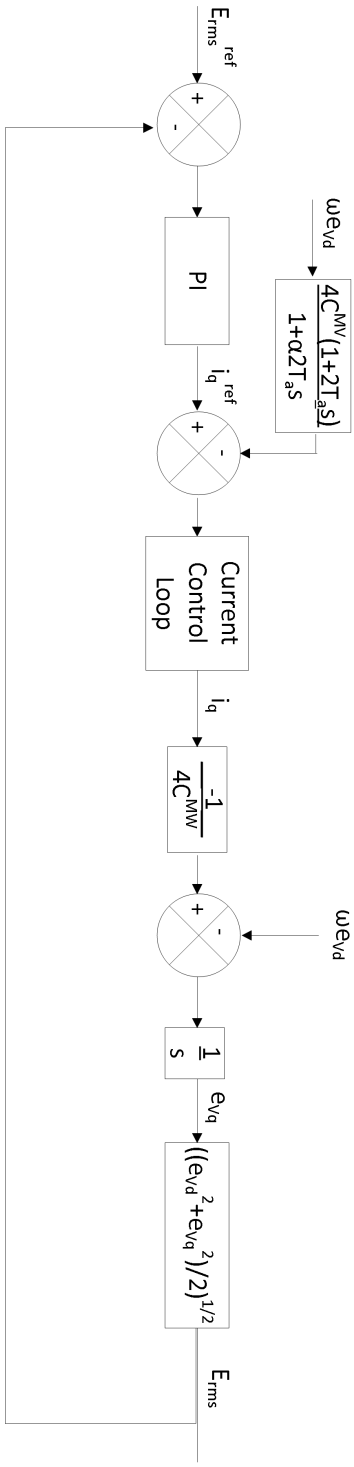

Figure 5.10: Block diagram for the rms value control loop

Chapter 6

Simulation Results on Modulation and Voltage Range

All simulations described in Chapter 6 are performed with open loop control system.

6.1 Voltage Range

The available range of voltage at the converter terminal is illustrated in Figure 6.1 and the values are given in Table C.1 in Appendix C. The voltage range was investigated by connecting the converter to the case circuit and controlling the voltage reference using open loop control. e_{Vq}^{ref} was set to zero and e_{Vd}^{ref} was adjusted while the rms value of the voltage at the converter terminal was measured. In Figure 6.1 the line to line rms voltage is divided by the DC voltage, i.e. 600 kV

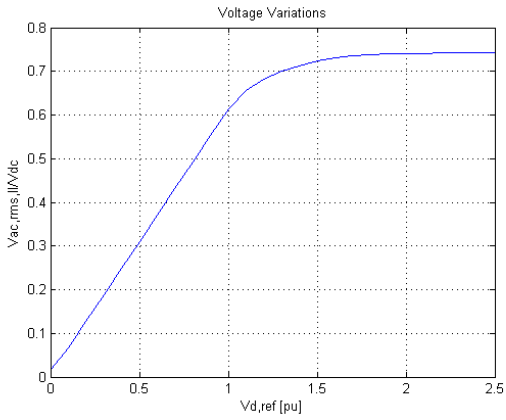

Figure 6.1: Converter terminal line voltage (rms) divided by the DC voltage as a function of m

as given in Appendix B.

It can be seen that the plot is linear with $e_{Vd}^{ref} \leq 1$ and that it flattens in the over-modulation range. The values in the upper part of the linear range fit very well with the theoretical values calculated in section 3.1.2, but are in general slightly higher. The rms voltage when $e_{Vd}^{ref} = 1.2$ is quite a bit larger than the value calculated with curve fitting in section 3.1.1. The reason for this could be that the rms value in PSCAD is calculated considering components from every frequency, while in the curve fitting only the fundamental frequency component was taken into account.

In section 3.1.2 the upper limit for over-modulation was found as $\frac{\sqrt{6}}{\pi}U_D = 0.78U_D$. The highest simulation value is $0.74\,U_D$. This indicates that the simulation model is unable to utilize the entire theoretical potential. The curve fitting value for $m = 1.2$ is $0.66\,U_D$. When considering Figure 6.1, it can be seen that this value is too low. A reason for this could be the low number of submodules used in the semi-analytical analysis.

6.2 Modulation Indexes and Resulting Voltage Curves

Figures 6.2, 6.3, 6.4, and 6.5 show the rms voltage and the three phase voltages at the converter terminal with different modulation indexes.

Table 6.1 compares the values from Table 3.2, the value from curve fitting in Figure 3.11, and the results seen in Figures 6.2 - 6.5. The modulation in the fundamental frequency is indicated as m_1, while m_3 is the third harmonic distortion of the reference voltage.

Figure 6.2 shows the voltages with modulation index 0.8. Table 6.1 indicates that the simulation voltage is closer to the theoretical value than the one gained from curve fitting, but as in section 6.1, the two different ways of calculating the rms voltage must be taken into account.

Figure 6.3 shows the voltages with modulation index 1.0. The three voltage values for this modulation index in Table 6.1 are quite similar.

Figure 6.4 shows the voltages with modulation index 1.2. It can be seen that the converter is in the over-modulation range as there are flat sections where the curves peak. This gives increased harmonic content, which could be the reason

Table 6.1: Voltage values from calculations and simulations

m_1	m_3	Theoretical voltage [kV]	Voltage value from curve fitting [kV]	Simulation voltage [kV]
0.8	0	293.94	284.75	294.2
1.0	0	367.42	363.75	366.2
1.2	0	-	394.98	405.4
1.155	0.1667	-	394.98	421.4

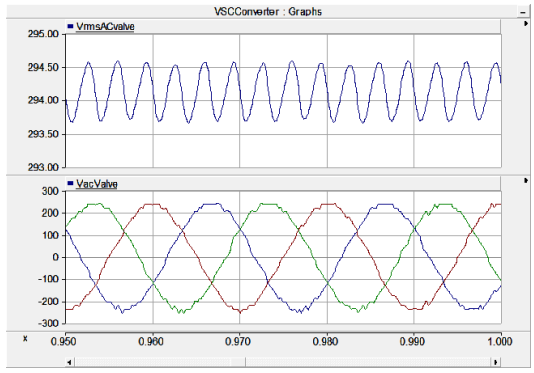

Figure 6.2: The rms voltage and the three phase voltages [kV] at the converter terminal with $m = 0.8$.

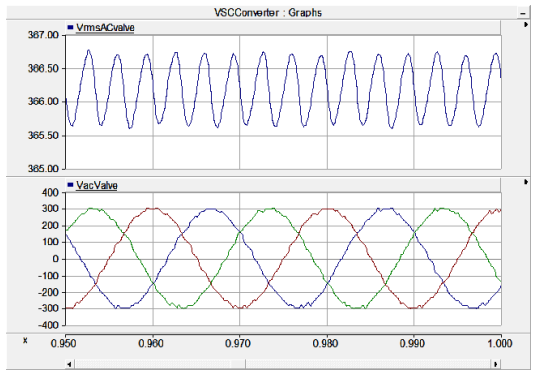

Figure 6.3: The rms voltage and the three phase voltages [kV] at the converter terminal with $m = 1.0$.

for the deviation between the two voltage values in Table 6.1 for this modulation index.

Figure 6.5 shows the voltages with modulation index 1.155 in the fundamental frequency and $\frac{1}{6}$ third harmonic. This corresponds to the case shown in Figures 3.10 and 3.11. The simulation result gives a much higher voltage than the curve fitting value indicated. The reason for this is that the curve fitting was done on a phase voltage, while the third harmonic distortion is only eliminated in the line voltage.

Comparing the three phase voltages in Figures 6.4 and 6.5 it can be seen that the corresponding line voltages will have different shapes and that the line voltages gained from Figure 6.5 will have the lowest harmonic content. Based on the theory explained in section 3.2, the case in Figure 6.5 is the one that gives largest rms voltage combined with lowest harmonic content.

To evaluate the quality of the sine wave approximations for the different modulation indexes, the Total Harmonic Distortion (THD) for the line to line voltages

Table 6.2: Total harmonic distortion

m_1	m_3	THD [%]
0.8	0	2.3
1.0	0	2.0
1.2	0	3.6
1.155	0.1667	1.7

is measured. The results are shown in Table 6.2.

The harmonic spectrum for the first 16 harmonics was analysed for every case. The given percentage value is the magnitude of the harmonic relative to the magnitude of the fundamental frequency component.

For $m = 0.8$ the dominating harmonics were the third (0.04 %), the fifth (0.09

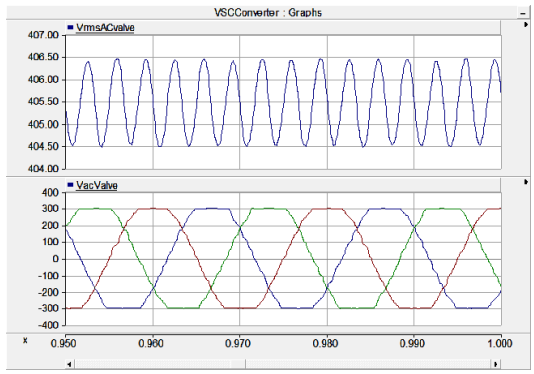

Figure 6.4: The rms voltage and the three phase voltages [kV] at the converter terminal with $m = 1.2$.

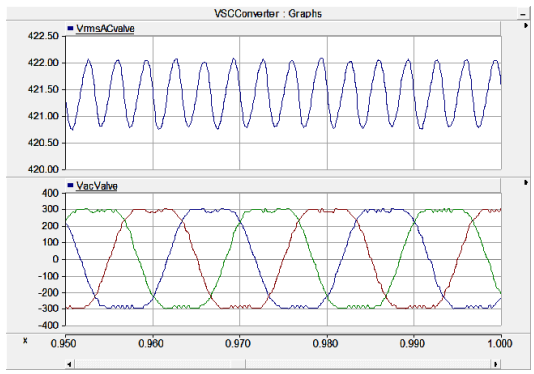

Figure 6.5: The rms voltage and the three phase voltages [kV] at the converter terminal with $m = 1.155$ and $\frac{1}{6}$ third harmonic.

%), the ninth (0.08 %), the eleventh (0.10 %), and thirteenth (0.06 %).

With $m = 1.0$ the third (0.04 %), the fifth (0.04 %), the seventh (0.07 %), the ninth (0.05 %), and the eleventh (0.05 %) were the dominating harmonics.

For $m = 1.2$ the dominating harmonics were the third (0.03 %), the fifth (3.17 %), the seventh (0.60 %), the eleventh (0.58 %), and the thirteenth (0.07 %).

With $m = 1.155$ and $\frac{1}{6}$ third harmonic distortion the third (0.03 %), the fifth (0.12 %), the seventh (0.12 %), the ninth (0.05 %), the eleventh (0.19 %), and the thirteenth (0.19 %) were the dominating harmonics.

The fifth harmonic content in the line voltage from $m = 1.2$ stands out as the largest harmonic component. The THD is also highest in this simulation case. The simulation case with third harmonic distortion resulted in the lowest THD for the line voltage and is therefore considered a successful solution for increasing the terminal voltage of the converter.

Chapter 7

Simulation Results on Power

All simulations described in Chapter 7 are performed with open loop control system.

7.1 Power Range

Table 7.1 compares the simulation results and calculated values for rms voltage, active power, reactive power, and apparent power at the converter terminal. In the table $\sqrt{{e_{Vd}^{ref}}^2 + {e_{Vd}^{ref}}^2}$ equals the modulation index, m, and σ is the angle between the grid voltage vector and the reference voltage given by $\sigma = \arctan(\frac{e_{Vq}^{ref}}{e_{Vd}^{ref}})$. δ is the angle between E and V. The simulation values and theoretical values for E from Table 3.2 are compared. The theoretical value is given as the analytical value in the linear region and the curve fitting result in the over-modulation region.

Equation 4.21 and 4.22 are used to find the corresponding power when the simulation values of the voltage E and angle δ are known. Apparent power is calculated from the active and reactive power, given by Equation 4.30. All deviations are calculated relative to the theoretical values.

The transformer in the simulation model has a Y Δ configuration and therefore introduces a 30° phase shift. This affects the angle measurement. In Table 7.1 δ_{meas} is the angle measured in the simulations. In the transformer in the simulation model the low voltage side is Δ connected and lags with 30°. The measurement of δ_{meas} is done between the converter terminal and the high voltage side of the transformer. The transformer phase shift is not included in the deviations of the power equations in Chapter 4. Therefore the angle of the low voltage side, adjusted for the transformer effects, is the angle that corresponds to the one used in the equations. As E leads V and the high voltage side leads the low voltage side, the correct angle δ used in the equations is found by adding 30° to δ_{meas}.

The reference voltages e_{Vd}^{ref} and e_{Vq}^{ref} are defined relative to a grid voltage vector. The angle of this vector, θ, is calculated by the Phase Locked Loop (PLL) block. In the simulations described in sections 7.1 and 7.2.1 the reference voltage for the PLL is the voltage between the filter and the transformer. The voltage at this point is

.

Table 7.1: Simulation values and calculated values of voltage and power at the converter terminal

e_{Vd}^{ref}	e_{Vq}^{ref}	m	σ	δ_{meas}	Measured values					Theoretical values					Deviations [%]			
					δ	E_{rms} [kV]	P [MW]	Q [MVAr]	S [MVA]	E_{rms} [kV]	P [MW]	Q [MVAr]	S [MVA]	E_{rms}	P	Q	S
0.8	0	0.8	0°	−79°	−49°	295.8	-1778.2	803.5	1951.3	293.94	-1781.2	791.5	1949.1	-0.63	0.17	-1.52	-0.11
0	0.8	0.8	90°	176°	206°	285.6	-967.8	4228.0	4337.4	293.94	-976.2	4234.6	4345.6	2.84	0.86	0.16	0.19
-0.8	0	0.8	180°	138°	168°	282.3	529.9	4319.9	4352.3	293.94	495.5	4331.2	4359.5	3.96	-6.93	0.26	0.17
0	-0.8	0.8	−90°	60°	90°	283.9	2294.1	2142.0	3138.6	293.94	2284.0	2135.6	3126.9	3.42	-0.44	-0.30	-0,37
1	0	1	0°	−84°	−54°	368.9	-2364.7	1922.0	3047.3	367.42	-2376.1	1908.6	3047.7	-0.40	0.48	-0.70	0.01
0	1	1	90°	166°	196°	355.2	-738.8	6093.7	6138.3	367.42	-746.6	6100.5	6146.0	3.33	1.05	0.11	0.13
-1	0	1	180°	142°	172°	352.2	432.9	6090.7	6106.1	367.42	428.7	6095.5	6110.5	4.14	-0.98	0.08	0.07
0	-1	1	−90°	70°	100°	351.6	2812.6	3746.8	4685.0	367.42	2792.7	3768.3	4690.3	4.31	-0.71	0.57	0.11
1.2	0	1.2	0°	−87°	−57°	408.8	-2684.0	2647.0	3769.7	394.98	-2726.6	2691.6	3831.4	-3.50	1.56	1.66	1.61
0	1.2	1.2	90°	161°	191°	392.8	-511.0	7135.0	7153.3	394.98	-556.4	7202.5	7223.9	0.55	8.16	0.94	0.98
-1.2	0	1.2	180°	145°	175°	389.7	339.0	7095.0	7103.1	394.98	314.6	7153.6	7160.5	1.34	-7.74	0.82	0.80
0	-1.2	1.2	−90°	75°	105°	388.4	3035.5	4752.0	5638.8	394.98	3030.2	4808.8	5683.9	1.67	-0.17	1.18	0.79

affected by the transformer current, as the voltage drop across the transformer defines the difference between the stiff grid voltage and this voltage. Therefore the voltage used in the PLL and hence the reference angle, is dependent on the transformer current. To achieve a control system independent of the transformer current, the PLL was moved and the simulations presented in section 7.2.3 are done with the stiff grid voltage as the PLL voltage. This modification should not change the results regarding angle δ, but it greatly affects the relationship between the angles σ and δ.

All deviation between simulation values and theoretical values in Table 7.1 are smaller than 10 %. This is seen as a satisfactory result.

The measured voltage is highest with $\sigma = 0°$, and for the two modulation indexes with analytically computed theoretical voltage values, i.e. m=0.8 and m=1.0, this angle gives the smallest voltage deviation.

For active power the largest deviations are found with $m = 0.8$ and $\sigma = 90°$, and $m = 1.2$ and $\sigma = 90°$ and $\sigma = 180°$. These deviations are found in the angle range where the active power crosses zero, and hence the active power magnitude is quite low. Where the theoretical value is small in magnitude, the deviation in percentage becomes extra large.

All deviations for reactive power and apparent power are small.

7.1.1 Simulations with Modulation Index equal 1.0

Multiple simulations are run with $m = 1$. The results are shown in Table C.2 in Appendix C. The notation is the same as for Table 7.1. To visualize how the values change with angle δ, the results are plotted.

The voltages in Table C.2 are illustrated in Figure 7.1. Active, reactive, and apparent power are presented in Figures 7.2, 7.3, and 7.4. Some trends can be seen:

The simulation results for rms value of the terminal voltage is highest for $\delta = 306°$ and lowest for $\delta = 152°$. The theoretical voltage value with $m = 1.0$ is 367.42 kV. The measured voltage is higher than this value for $\sigma = 0°$, $\delta = 306°$ with 0.4 %. The lowest measured voltage is 5.5 % lower than the theoretical value.

From Figure 7.1 it seems that the voltage is depending on angle δ. Three possible reasons for this are suggested. The first one is that there are inaccuracies in the PLL. If the reference angle is incorrect, the voltage will not become exactly what the voltage references indicate. However, this reason would not explain the dependence on angle δ, and the deviations from the theoretical value are considered too large to make this explanation plausible.

The second possible reason is that the voltage used in the PLL not is the voltage in the stiff grid, but the voltage between the filter and the transformer. The current depending reference could affect the references given by the control system and hence the generated voltage. This option was investigated by running simulations with the stiff grid voltage as the PLL voltage. The results are shown in Table C.3 in Appendix C. It can be seen that the voltage also with this reference angle is depending on angle δ. The combinations of angle δ values and voltage values are quite similar and the voltage value range is approximately the same. This theory is therefore dismissed.

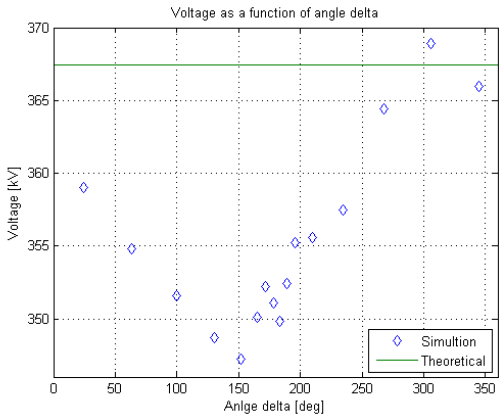

Figure 7.1: The rms value of the terminal voltage [kV] as a function of angle δ with $m = 1$

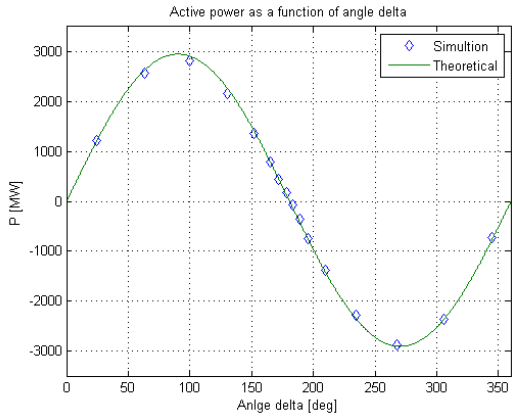

Figure 7.2: Active power at the converter terminal [MW] as a function of angle δ with $m = 1$

The third possible reason is that the converter can be modelled as a voltage source behind an impedance. In that case the terminal voltage would depend on both the magnitude and the angle of the current. When comparing Figure 7.1 with Figures 7.7 and 7.8, this is regarded as a possible solution. If this is the case, the modelling of the converter could be considered more like a model of a synchronous generator. Out of the three possible explanations, this is considered the far most likely.

The simulation results for active power follow the theoretical curve very closely. The relative deviations in Table 7.1 were found to be largest in the angle range $168 \leq \delta \leq 191$. It can be seen that this is an area where the active power is low,

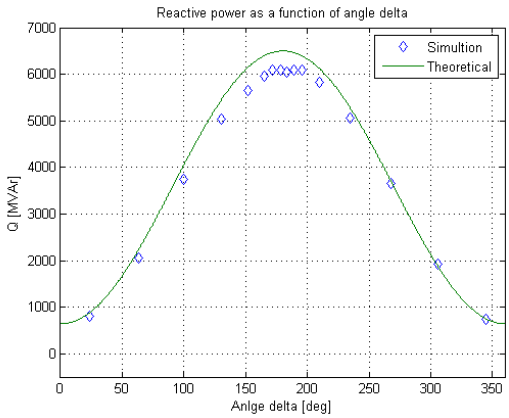

Figure 7.3: Reactive power at the converter terminal [MVAr] as a function of angle δ with $m = 1$

giving high percentage values for the relative deviations. However, the deviations in Table 7.1 were small with $m = 1.0$. This is consistent with Figure 7.2.

For low values of reactive power, the simulation results are very close to the theoretical values. At high values the simulation results are lower than the theoretical values. This is not the same result as in Table 7.1. The reason for this is that the theoretical reactive power curve in Figure 7.3 is made with the theoretical terminal voltage value, while the theoretical power values in Table 7.1 are given for the measured terminal voltages. The value of reactive power calculated by Equation 4.22 is strongly affected by the terminal voltage value. As the voltage values shown in Figure 7.1 are lower than the theoretical ones in the angle range with large deviations in reactive power, this could explain why the simulation values for reactive power are lower.

The simulation values for apparent power are close to the theoretical values for angle δ values close to zero. In this area the magnitude of active power is quite large, and the simulation values for reactive power follow the theoretical curve. In the area close to $\delta = 180°$ the deviations are larger. For this angle range the magnitude of active power is low, so the magnitude of reactive power is dominating the value of apparent power. Again the low terminal voltage is affecting the simulation values. This can be seen from Equation 4.30.

7.2 Transformer Effects

The transformer introduces non-linear effects due to its magnetizing inductance. This affects the power flow in the network. As the magnetizing inductance is not included in the theoretical model, this could be a reason for deviations between simulation values and theoretical values.

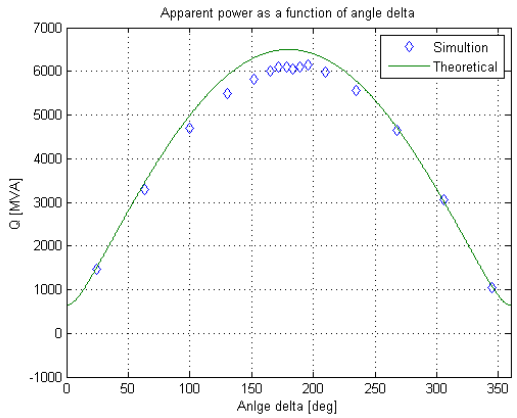

Figure 7.4: Apparent power at the converter terminal [MVA] as a function of angle δ with $m = 1$

7.2.1 Measurements and Calculations of Reactive Power

The non-linear effects of the transformer are investigated in Table 7.2 and 7.3. In Table 7.2 the voltage, active power, and reactive power on both sides of the transformer are shown together with the difference between the values. It can be seen that the voltage on the low voltage side is very low for some cases, especially for $\sigma = 90°$ and $\sigma = 180°$. This corresponds to a large difference in reactive power. The difference in active power is generally low.

The currents in Table 7.2 are calculated in pu and the angle is relative to the stiff grid. This means that an angle of 0° gives a current in phase with the voltage on the high voltage side going from the low voltage side to the high voltage side, that is from the converter to the grid. It can be seen that the current is leading the grid voltage as the angle between current and voltage, ϕ, is between 0° and 180°. This corresponds to a negative value for the reactive power at the high voltage side of the converter.

With $\sigma = 0°$, and $m = 1.0$ and $m = 1.2$ the reactive power at the two sides of the converter has opposite signs. This is because the current is lagging the voltage at the low voltage side. It can therefore be concluded that the voltage on the low voltage side lags the voltage on the high voltage side in these cases, also when the transformer phase shift is disregarded.

To investigate the change in reactive power across the transformer, equations for apparent power are used. The change in active power and the corresponding resistance are disregarded due to their order of magnitude. The transformer is regarded as pure inductance in the calculation, which means that all magnetizing effects are disregarded. Let LV indicates low voltage side while HV indicates high voltage side.

$$\vec{S} = \vec{V}\vec{i}^{*} = P + jQ \tag{7.1}$$

Table 7.2: Voltage, active power, and reactive power on both sides of the transformer

						Low voltage side			High voltage side			Difference		
e_{Vd}^{ref}	e_{Vq}^{ref}	m	σ	δ_{meas}	δ	Current [pu], ϕ	Voltage [pu]	P [MW]	Q [MVAr]	Voltage [pu]	P [MW]	Q [MVAr]	ΔVoltage [pu]	ΔP [MW]	ΔQ [MVAr]
0.8	0	0.8	0°	−79°	−49°	3.30 <155°	0.91	-1791.3	-181.6	1.00	-1793.3	-841.2	-0.09	2.0	659.6
0	0.8	0.8	90°	176°	206°	7.60 <103°	0.31	-1036.4	-970.5	1.00	-1046.8	-4438.8	-0.69	10.4	3468.8
-0.8	0	0.8	180°	138°	168°	7.72 <84°	0.25	459.4	-1036.0	1.00	448.7	-4609.2	-0.75	10.7	3573.2
0	-0.8	0.8	270°	60°	90°	5.53 <47°	0.70	2257.6	-605.1	1.00	2252.1	-2439.3	-0.30	5.5	1834.2
1.0	0	1.0	0°	−84°	−54°	4.13 <165°	0.98	-2387.2	379.1	1.00	-2391.9	-652.5	-0.02	4.7	1031.6
0	1.0	1.0	90°	166°	196°	8.65 <99°	0.20	-829.9	-632.4	1.00	-844.8	-5118.9	-0.80	14.9	4486.5
-1.0	0	1.0	180°	142°	172°	8.68 <86°	0.15	341.9	-679.9	1.00	327.4	-5196.1	-0.85	14.5	4516.2
0	-1.0	1.0	270°	70°	100°	6.67 <47°	0.69	2758.4	-242.8	1.00	2749.5	-2905.3	-0.31	8.9	2662.5
1.2	0	1.2	0°	−87°	−57°	4.64 <168°	1.00	-2711.8	705.7	1.00	-2717.8	-591.6	0	6.0	1297.3
0	1.2	1.2	90°	161°	191°	9.16 <97°	0.14	-611.0	-423.0	1.00	-628.0	-5463.0	-0.86	17.0	5040.0
-1.2	0	1.2	180°	145°	175°	9.16 <88°	0.10	238.8	-456.5	1.00	222.8	-5493.4	-0.90	16.0	4982.9
0	-1.2	1.2	270°	75°	105°	7.30 <48°	0.68	2970.6	-36.8	1.00	2959.2	-3232.1	-0.32	11.4	3195.3

.

$$\vec{S_{LV}} - \vec{S_{HV}} = \vec{V_{LV}}\vec{i}^* - \vec{V_{HV}}\vec{i}^* = (\vec{V_{LV}} - \vec{V_{HV}})\vec{i}^* \tag{7.2}$$

$$\vec{V_{LV}} - \vec{V_{HV}} = jX\vec{i} \tag{7.3}$$

Inserting Equation 7.3 into Equation 7.2:

$$\vec{S_{LV}} - \vec{S_{HV}} = jX\vec{i}\vec{i}^* = jX|\vec{i}|^2 \tag{7.4}$$

Using that V_{HV}=1.0 and as the stiff grid voltage is purely real, Equation 7.1 can be applied:

$$\vec{S_{LV}} - \vec{S_{HV}} = jX|\vec{i}|^2 = jX|S_{HV}|^2 \tag{7.5}$$

where X=0.1 pu is the transformer leakage inductance.

Accordingly the change in reactive power across the transformer is 10 % of the square of the apparent power at the high voltage side. A different approach could be:

$$\vec{S_{LV}} - \vec{S_{HV}} = (\vec{V_{LV}} - \vec{V_{HV}})\vec{i}^* = (\vec{V_{LV}} - \vec{V_{HV}})(\frac{\vec{V_{LV}} - \vec{V_{HV}}}{jX})^* = j\frac{|\vec{V_{LV}} - \vec{V_{HV}}|^2}{X} \tag{7.6}$$

But as this method requires calculation of the real and imaginary part of the low voltage side voltage, the approach in Equation 7.5 is preferred.

In Table 7.3 the changes in reactive power across the transformer are calculated and the results are compared with the measured values form Table 7.2. The relative deviations are calculated with the measured value as the reference. The deviations are in general very small. The deviation for the second last calculation is somewhat higher. The reason for this is unknown.

Table 7.3: Calculated and measured change in reactive power across the transformer

P_{HV} [MW]	Q_{HV} [MVAr]	P_{HV} [pu]	Q_{HV} [pu]	XS^2_{HV} [pu]	XS^2_{HV} [MVAr]	ΔQ [MVAr]	$\Delta Q - XS^2_{HV}$ [MVAr]	$\frac{\Delta Q - XS^2_{HV}}{\Delta Q}$ [%]
-1793.3	-841.2	-2.99	-1.40	10.90	653.92	659.6	5.68	0.86 %
-1046.8	-4438.8	-1.74	-7.40	57.77	3 466.46	3468.8	2.34	0.07 %
448.7	-4609.2	0.75	-7.68	59.57	3 574.34	3573.2	-1.14	-0.03 %
2252.1	-2439.3	3.75	-4.07	30.62	1 837.02	1834.2	-2.82	-0.15 %
-2391.9	-652.5	-3.99	-1.09	17.07	1 024.49	1031.6	7.11	0.69 %
-844.8	-5118.9	-1.41	-8.53	74.77	4 486.14	4486.5	0.36	0.01 %
327.4	-5196.1	0.55	-8.66	75.30	4 517.77	4516.2	-1.57	-0.03 %
2749.5	-2905.3	4.58	-4.84	44.45	2 666.75	2662.5	-4.25	-0.16 %
-2717.8	-591.6	-4.53	-0.99	21.49	1 289.40	1297.3	7.90	0.61 %
-628	-5463	-1.05	-9.11	84.00	5 039.79	5040	0.21	0.00 %
222.8	-5493.4	0.37	-9.16	83.96	5 037.85	4982.9	-54.95	-1.10 %
2959.2	-3232.1	4.93	-5.39	53.34	3 200.56	3195.3	-5.26	-0.16 %

7.2.2 No-Load Test

A no-load test was done to identify the magnetizing inductance of the transformer. The reactive power was found to be 0.00500 pu when the voltage was 1.0 pu. This gives a magnetizing inductance of 200 pu. This equals 95.5 H on the low voltage side and 169.8 H on the high voltage side.

Based on Greenwood [35] this is a slightly high inductance value. A typical current value at a no-load test for this type of transformer should be 0.6 % giving an inductance of 167 pu. This corresponds to 79.6 H on the low voltage side and 141.5 H on the high voltage side.

The reactive power consumed by this inductance can be calculated, assuming that the voltage across the inductance is 1.0 pu:

$$Q = \frac{(1.0)^2}{200} = 0.005\text{pu} = 3\text{MVAr} \tag{7.7}$$

This value is very small compared to the values in Table 7.3. It is therefore considered acceptable to ignore the magnetizing effects.

7.2.3 Substituting the Transformer with an Inductance

To ensure that the model used in the theoretical analysis describes the simulation in a proper manner, the effect of the transformer on the load flow was investigated. The load flow with the transformer substituted with an equivalent inductance was compared with the original simulation model to validate the theoretical model. The results are shown in Table C.4 in Appendix C. It can be seen that the results are almost identical. Before this simulation was done, the reference for angle σ was changed in the simulation model by moving the PLL. This should only affect the relationship between the two angles σ and δ and not affect any other simulation values.

The simulation results for active and reactive power at the converter terminal and the stiff grid are shown in Figures 7.5 and 7.6 together with the theoretical power curves.

It can be seen that the simulation results for the active power in Figure 7.5 are consistent with the theoretical values.

Also in Figure 7.6 it can be seen how low voltage at the converter terminal affects the reactive power. However, the simulation values at both points fit quite well with the theoretical curves.

To investigate the load flow further, the current in each of the eight simulation cases was calculated. The results based on voltage and power values from Table C.4 are shown in Table 7.4. The voltage drop across the connection was divided by the impedance to get the current in the second and third column. Using that:

$$\vec{I} = \frac{\vec{E} - \vec{V}}{R + jX} \tag{7.8}$$

The active and reactive power at the converter terminal (CT) was used to calculate the current in the fourth and fifth column. And the active and reactive

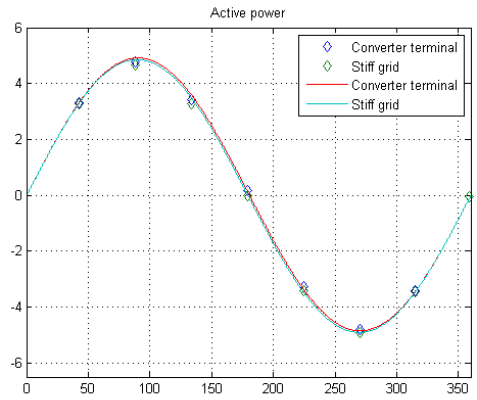

Figure 7.5: Active power [pu] at the converter terminal and the stiff grid, simulation results and theoretical curves, as functions of δ

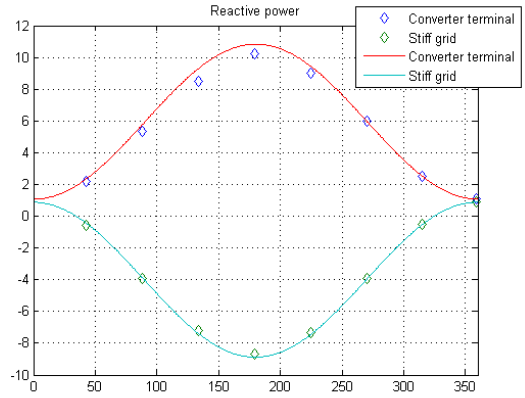

Figure 7.6: Reactive power [pu] at the converter terminal and the stiff grid, simulation results and theoretical curves, as functions of δ

power at the stiff grid (SG) was used in the same way in sixth and seventh column. Using that:

$$\vec{S} = \vec{U}\vec{I}^* = P + jQ \tag{7.9}$$

$$\vec{I} = \left(\frac{P + jQ}{\vec{U}}\right)^* \tag{7.10}$$

where $\vec{U}$ is the measured voltage.

Comparing Table 7.4 and Table C.4 shows that the current lags the voltage at every angle at the converter terminal. This gives positive values for reactive power. For $\sigma < 180°$ the lag is more than 90° giving negative active power values.

At the stiff grid, the current leads the voltage for every case, except for $\sigma = 0°$, giving negative reactive power. For $\sigma > 180°$ the current leads less than 90°, giving positive values for active power.

The magnitude of the current is proportional to the apparent power at the stiff grid as the voltage is constant at this point. The current is largest with $\sigma = 180°$ and smallest with $\sigma = 0°$. Pairs of current values with equal distance from these two point are quite similar in magnitude.

There are very small deviations in the magnitude of the current, |I|, with the two calculation methods. The differences in angle ϕ values are a bit larger, the largest difference is 2.07°. The reason for the differences is assumed to be inaccuracies.

Figure 7.7 shows how the calculated values for current magnitude in Table 7.4 fits with the theoretical curve. "Calculated1" is the value based on voltage values while "calculated2" and "calculated3" are the values based on power values. It can be seen that the values are very similar for smaller current magnitudes, but for larger magnitudes the theoretical values are slightly higher. This is related to the angle δ dependency of the terminal voltage seen in Figure 7.1.

Figure 7.8 shows the theoretical and the calculated angle ϕ values. "Calculated1" is the value based on voltage values while "calculated2" and "calculated3" are the values based on power values. It can be seen that the simulation values fit very well theoretical ones.

Table 7.4: Calculated current values

	Voltage values		Power values CT		Power values SG	
Case	|I| [pu]	ϕ [deg]	|I| [pu]	ϕ [deg]	|I| [pu]	ϕ [deg]
1	0.88	-95.19	0.89	-93.12	0.88	-93.25
2	3.49	171.30	3.48	171.46	3.48	171.24
3	6.31	141.00	6.28	141.14	6.29	141.33
4	8.10	114.90	8.05	115.05	8.08	115.04
5	8.72	89.80	8.67	89.90	8.71	90.13
6	7.92	65.65	7.97	66.03	7.93	65.50
7	6.08	39.46	6.06	39.71	6.08	39.87
8	3.29	9.42	3.31	9.79	3.32	10.23

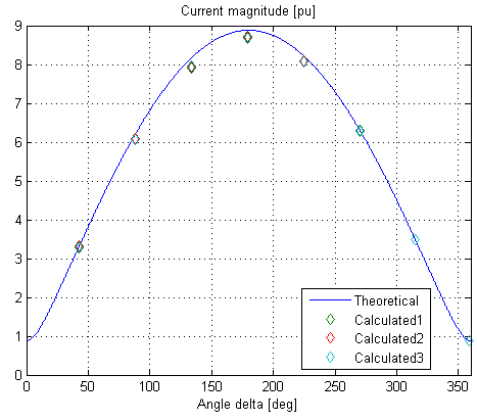

Figure 7.7: Current magnitude [pu], theoretical value and values from Table 7.4, as functions of δ

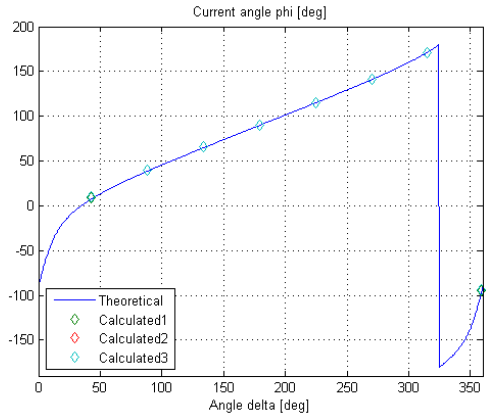

Figure 7.8: Current angle ϕ [deg], theoretical value and values from Table 7.4, as functions of δ

Chapter 8

Implementation of the Control System into PSCAD

All values of parameters implemented in the control system in PSCAD are given in Appendix D.

8.1 Inner Loops: Current Control Loops

First, only the current loops were implemented to ensure that the inner control loops operated satisfactory.

The current control loops in PSCAD are shown in Figure 8.1.

Figure 8.2a shows the simulation where the reference for i_d is changed from 0 pu to -1.0 pu. The upper plot show i_d^{ref} and i_d. i_d uses approximately 0.3 seconds to adjust when the reference is changed. The second plot shows i_q^{ref} and i_q. Even as i_q^{ref} is constant, i_q is changed due to the change in i_d^{ref}. This is because of the

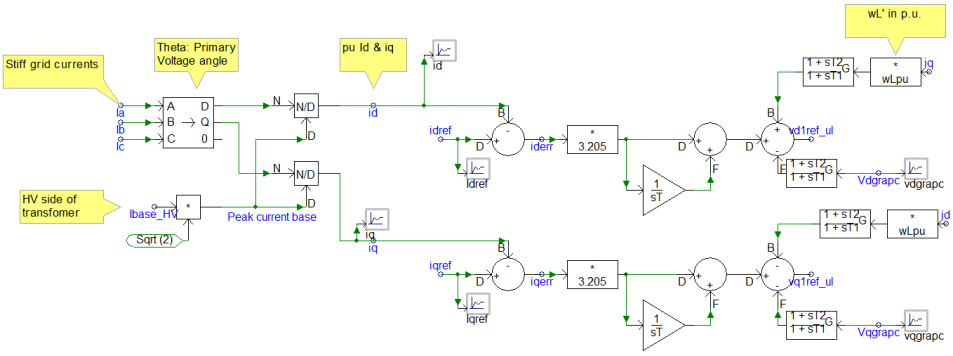

Figure 8.1: The current control loops in PSCAD

cross coupling between the control loops. i_q uses longer time than i_d to return to the reference, approximately one second. The third plot shows the errors between the current values and the reference values for the currents. It can be seen that the errors go towards zero. The last plot shows the reference voltages sent to the lower level control system, corresponding to $e_{\mathrm{Vd}}^{\mathrm{ref}}$ and $e_{\mathrm{Vq}}^{\mathrm{ref}}$ in Figure 5.5.

Figure 8.2b shows the simulation where the reference for i_d is changed from 0 pu to 0.2 pu and the reference for i_q is changed from 0 pu to 0.6 pu. i_d uses about 1.0 second to adjust to the new reference while i_q uses 0.4 seconds.

Figure 8.3 show the three phases of the voltage at the converter terminal for the case in Figure 8.2b. It can be seen that the voltage is close to sinusoidal and increases quickly after the reference change.

8.2 Outer Loops

8.2.1 Limits

When the outer loops were implemented, certain limits were used to ensure stable operation. The voltage orders to the converter were limited to ± 1.15 pu as simulations earlier had shown that 1.2 pu is close to the upper voltage stability limit.

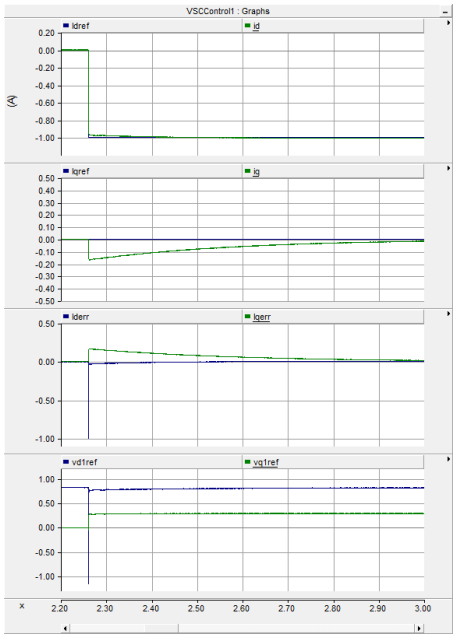

(a) i_d^{ref} is changed from 0 pu to -1.0 pu

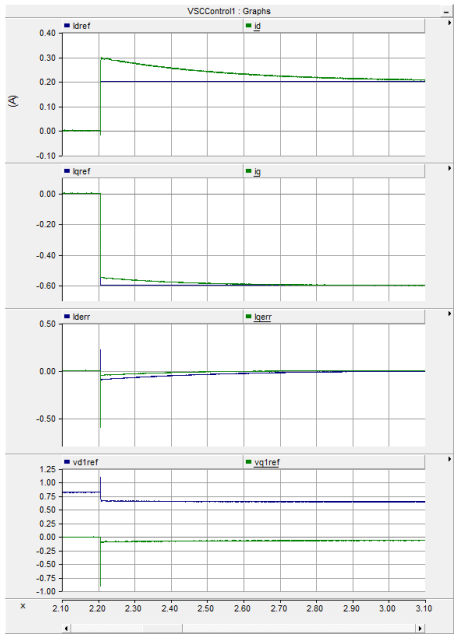

(b) i_d^{ref} is changed from 0 pu to 0.2 pu and i_q^{ref} is changed from 0 pu to 0.6 pu

Figure 8.2: Simulations with current control: Top: i_d^{ref} and i_d, second: i_q^{ref} and i_q, third: $i_d^{\mathrm{err}} = i_d^{\mathrm{ref}} - i_d$ and $i_q^{\mathrm{err}} = i_q^{\mathrm{ref}} - i_q$, bottom: $e_{\mathrm{Vd}}^{\mathrm{ref}}$ and $e_{\mathrm{Vq}}^{\mathrm{ref}}$.

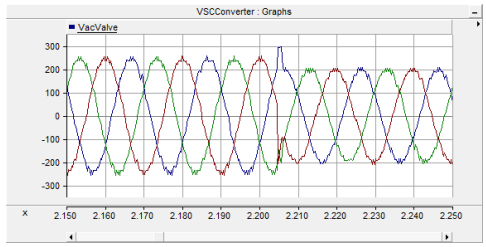

Figure 8.3: The three phases of the voltage [kV] at the converter terminal corresponding to Figure 8.2b

Simulations had also shown that the upper value for apparent power within the stable angle range was close to 6 pu. Based on this, the current references were limited to 4 pu. The limits on the apparent power limited the possible combinations of active and reactive power compared to the plots shown in section 4.4. It is also observed that the voltage wave shape at the converter terminal is damaged when the voltage is lower than 0.2 pu. The resulting PQ range is shown in Figure 8.4.

The limits set in the simulation model are more useful to prove how much power the simulation model of the converter can deliver, than to show realistic limitations for an actual converter. In an actual converter, current limitations will determine the upper level for apparent power output [32]. For a short period of time, the current can be increased above the normal limit, but to avoid overheating, the apparent power should normally be kept for instance no more than 10 % above

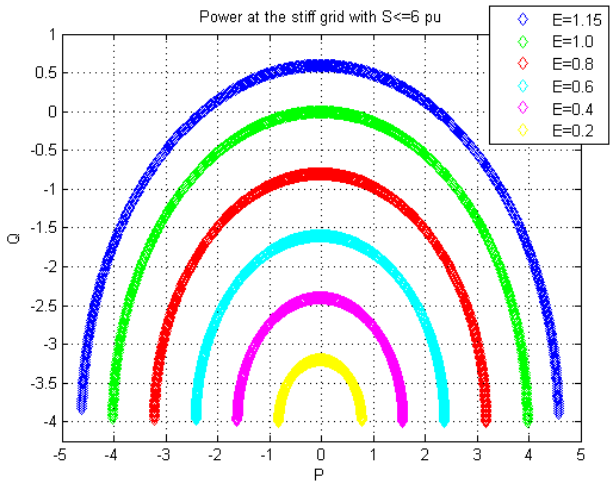

Figure 8.4: The PQ [pu] range of the implemented control system for different terminal voltages [pu]

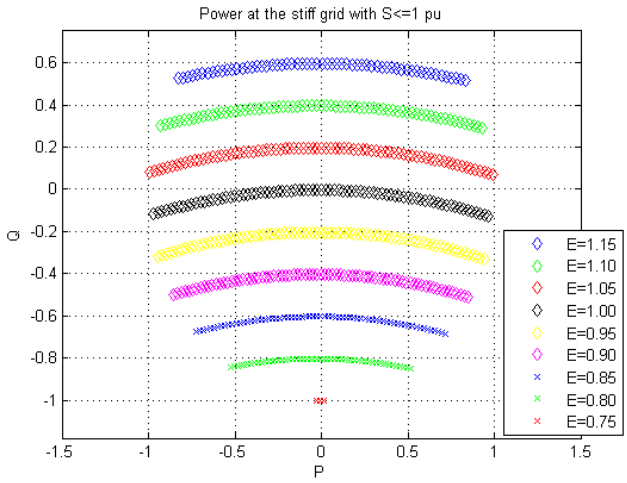

Figure 8.5: The PQ [pu] range with maximum apparent power equal 1.0 pu for different terminal voltages [pu]

rated power. To show the consequence of such a limitation, a plot of possible combinations of active and reactive power at different converter terminal voltage levels with maximal apparent power equal 1.0 pu is made. The plot is shown in Figure 8.5.

Comparing Figure 8.4 and Figure 8.5, it can be seen that the current limitations have great impact on the characteristics of the converter. It can also be seen that low converter terminal voltages correspond to large negative values of i_q, which results in large negative reactive power values at the grid. When the apparent power is limited to 1.0 pu, the lowest possible terminal voltage is 0.75 pu at the point where active power is zero and reactive power is -1.0 pu. A terminal voltage lower than 0.75 pu will give apparent power larger than 1.0 pu for every angle δ. In addition, it can be seen that the maximal range in Figure 8.5 would have been a circle with centre at the origin and radius 1.0 if there had been no upper limit on the converter voltage.

8.2.2 Active Power and Reactive Power Control

The control loops for active and reactive power were implemented as described in section 5.2. To avoid time delays in the feedback loop, the active and reactive power were calculated using voltage and current values instead of power measurements. Resettable integrators were used in the PI controllers. A logic signal was used to reset the integrators when the converter was blocked after start-up and when direct current control was used. The active power control loop in PSCAD is shown in Figure 8.6, while the reactive power loop is shown in Figure 8.7.

Figure 8.8 shows the simulation where Q_{ref} was kept equal to -1.0 pu and P_{ref}

was changed from 0 pu to 1.0 pu. The upper plot of Figure 8.8a shows that the active power uses about 0.01 seconds to adjust to the new reference. The reactive power is affected by the reference change and uses about the same time to return to its reference value. The largest deviation from the reference in this period is 0.06 pu. The rms value at the converter terminal is increased from 0.77 pu to 0.80 pu. This takes about 0.01 seconds.

In Figure 8.8b it can be seen that i_d^{ref} increases gradually and that i_d follows almost perfectly. This is not the case with the q axis currents: i_q^{ref} drops 0.11 pu when the reference is changed and uses about 1.0 second to return to its former value. i_q has a small increase lasting about 0.02 seconds before it returns to the reference value from before the change. This peak fits very well with the peak in reactive power. While i_q^{ref} is lower than in steady-state and i_q has taken the steady-state value, there is a quite large error in the q axis current controller. The q axis voltage reference uses about 0.01 seconds to change to a new value. The d axis voltage reference is affected by the reference change in about the same period of time before it returns to its former value.

In this simulation case the active power and reactive power controllers worked satisfactory.

Figure 8.9 shows a more extreme situation. At the same instant P_{ref} is changed from 1.0 pu to -3.0 pu and Q_{ref} changed from -1.0 pu to -4.0 pu. The upper plots of Figure 8.9a show that both active power and reactive power use about 0.01 seconds to adjust to the new references. The rms value at the converter terminal is decreased from 0.80 pu to 0.70 pu. This takes about 0.02 seconds.

The same trend that was seen with the q axis currents in Figure 8.8b is observed in Figure 8.9b: The currents i_d and i_q take on new values rapidly, here in about 0.01

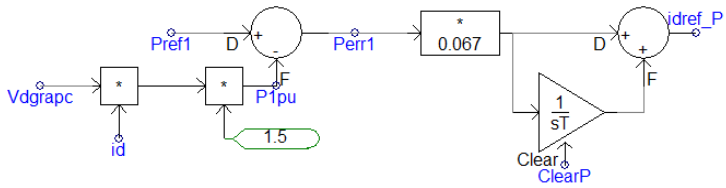

Figure 8.6: The active power control loop in PSCAD

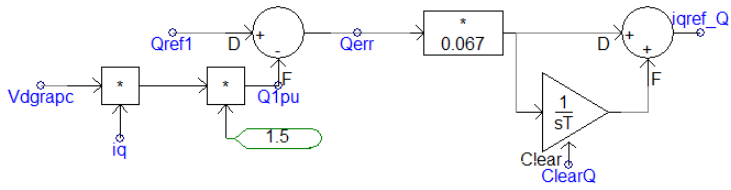

Figure 8.7: The reactive power control loop in PSCAD

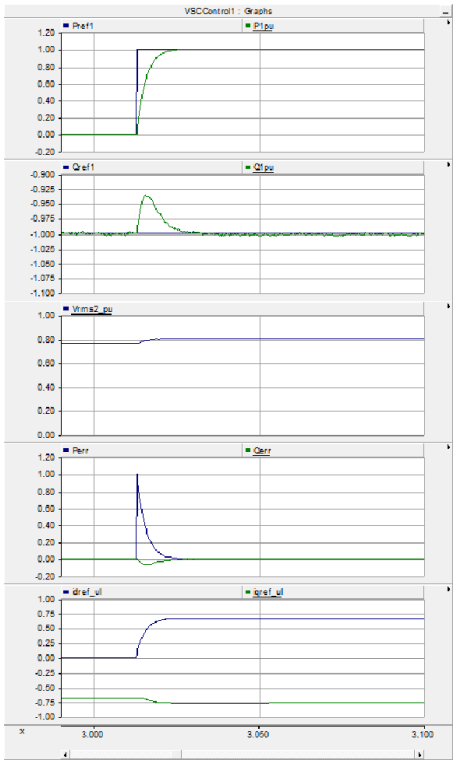

(a) Power control: Top: P_{ref} and P, second: Q_{ref} and Q, third: E_{rms}, forth: $P_{\text{err}} = P_{\text{ref}} - P$ and $Q_{\text{err}} = Q_{\text{ref}} - Q$, bottom: the unlimited current references $i_{\text{d,ref\_ul}}$ and $i_{\text{q,ref\_ul}}$

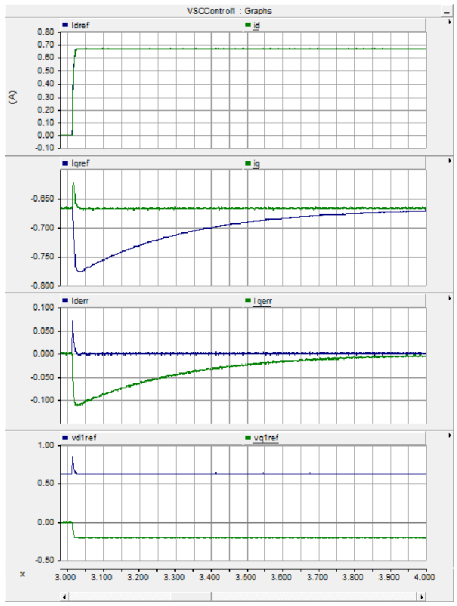

(b) Resulting currents: Top: i_d^{ref} and i_d, second: i_q^{ref} and i_q, third: $i_d^{\text{err}} = i_d^{\text{ref}} - i_d$ and $i_q^{\text{err}} = i_q^{\text{ref}} - i_q$, bottom: $e_{\text{Vd}}^{\text{ref}}$ and $e_{\text{Vq}}^{\text{ref}}$.

Figure 8.8: Simulation 1 with active power and reactive power control: Q_{ref} is kept constant at -1.0 pu while P_{ref} is changed from 0 pu to 1.0 pu. Note that the time resolution differs in the two graphs.

seconds, and the values are kept approximately constant after that. The current references however, use about 1.0 second to adjust. Both i_d and i_d^{ref} drop at the reference change, but i_d^{ref} takes a value that is approximately 0.3 pu lower than i_d and uses time to increase. Also i_q and i_q^{ref} drop, but i_q^{ref} takes a value that is 0.4 pu larger than i_q and then gradually decreases. The voltage references use about 0.02 seconds to adjust to new and constant values.

Figure 8.10 show the three phases of the voltage at the converter terminal for the case in Figure 8.9. It can be seen that the voltage uses about 0.01 seconds to achieve a sinusoidal wave shape. This is considered acceptable.

Also in this more extreme case, the active power and reactive power controllers worked satisfactory. It is therefore concluded that the implementation of the control system for active and reactive power is successful.

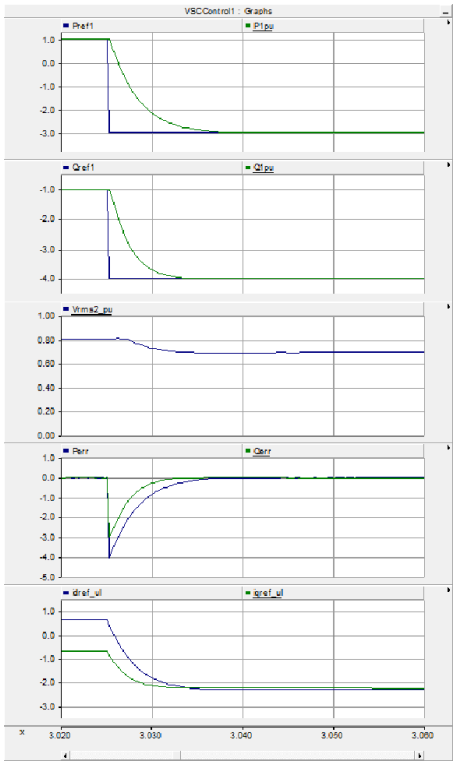

(a) Power control: Top: P_{ref} and P, second: Q_{ref} and Q, third: E_{rms}, forth: $P_{\text{err}} = P_{\text{ref}} - P$ and $Q_{\text{err}} = Q_{\text{ref}} - Q$, bottom: the unlimited current references $i_{\text{d,ref\_ul}}$ and $i_{\text{q,ref\_ul}}$

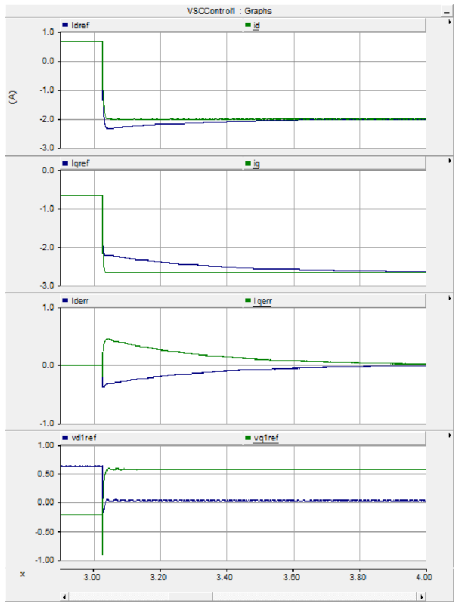

(b) Resulting currents: Top: i_d^{ref} and i_d, second: i_q^{ref} and i_q, third: $i_d^{\text{err}} = i_d^{\text{ref}} - i_d$ and $i_q^{\text{err}} = i_q^{\text{ref}} - i_q$, bottom: $e_{\text{Vd}}^{\text{ref}}$ and $e_{\text{Vq}}^{\text{ref}}$.

Figure 8.9: Simulation 2 with active power and reactive power control: P_{ref} is changed from 1.0 pu to -3.0 pu and Q_{ref} is changed from -1.0 pu to -4.0 pu at the same instant. Note that the time resolution differs in the two graphs.

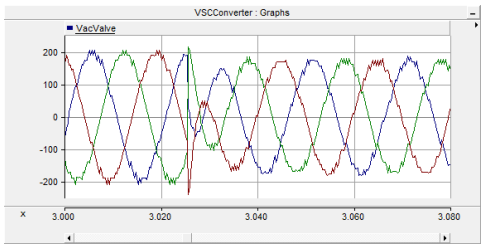

Figure 8.10: The three phases of the voltage [kV] at the converter terminal corresponding to Figure 8.9

8.2.3 Active Power and RMS Value Control

When the rms value controller was implemented in PSCAD, two changes were made compared to the structure described in section 5.2. The first change was a change of sign in the controller gain as the reference direction in the control system is opposite to the one in the equations. The second change was that the feedback signal was implemented as a calculated value, not the measurement of the rms voltage. The reason for this is that the rms voltage is the direct result of the voltage reference given to the converter. To use a measurement of the reference as a feedback would give an oscillatory system, due to a lack of time delay. The converter terminal voltage was therefore calculated, using that:

$$E = V + iZ \tag{8.1}$$

where $Z = R + jZ$.

Calculation in the dq domain gives:

$$E_d + jE_q = V_d + (i_d + ji_q)(R + jZ) \tag{8.2}$$

as $V_q = 0$.

This gives:

$$E_d = V_d + Ri_d - Zi_q \quad E_q = Zi_d + Ri_q \tag{8.3}$$

Figure 8.11 shows the the rms value control loop in PSCAD (Figure 8.11a) with the calculation of the feedback signal (Figure 8.11b).

Figure 8.12 shows the simulation where P_{ref} was kept equal to 1.0 pu and $E_{\text{rms}}^{\text{ref}}$ was changed from 1.0 pu to 0.8 pu. The upper plot of Figure 8.12a shows that there is a small increase in the active power when the reference is changed. The largest deviation from the reference is 0.07 pu and the deviation lasts for about 0.02 seconds. The voltage uses less than 0.02 seconds to adjust to the new reference. The reactive power decreases from 0.08 pu to -1.30 pu in 0.02 seconds.

In Figure 8.12b it can be seen that i_q^{ref} decreases gradually and that i_q follows almost perfectly. A new and stable value is found after approximately 0.02 seconds.

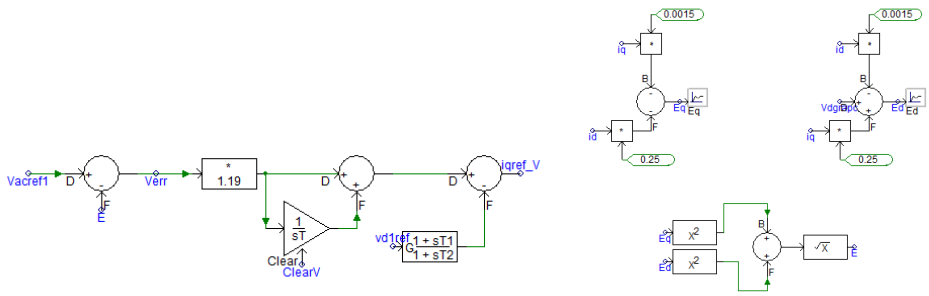

Figure 8.11: The rms value control loop in PSCAD

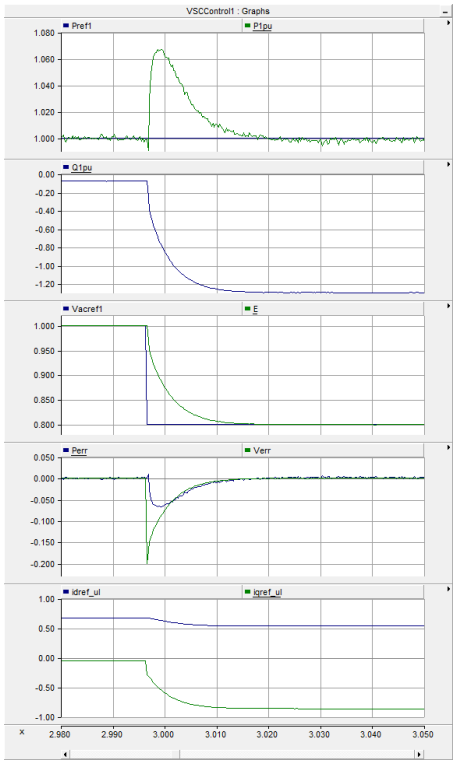

(a) Active power and rms value control: Top: P_{ref} and P, second: Q, third: $E^{\text{ref}}_{\text{rms}}$ and E_{rms}, forth: $P_{\text{err}} = P_{\text{ref}} - P$ and $E^{\text{err}}_{\text{rms}} = E^{\text{ref}}_{\text{rms}} - E_{\text{rms}}$, bottom: the unlimited current references $i_{\text{d,ref\_ul}}$ and $i_{\text{q,ref\_ul}}$

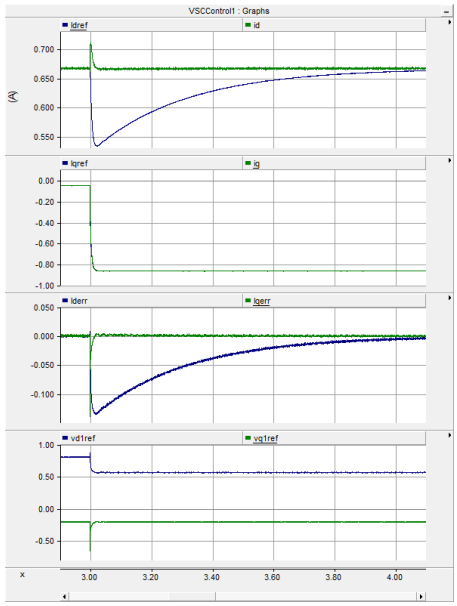

(b) Resulting currents: Top: i^{ref}_d and i_d, second: i^{ref}_q and i_q, third: $i^{\text{err}}_d = i^{\text{ref}}_d - i_d$ and $i^{\text{err}}_q = i^{\text{ref}}_q - i_q$, bottom: $e^{\text{ref}}_{\text{Vd}}$ and $e^{\text{ref}}_{\text{Vq}}$.

Figure 8.12: Simulation 1 with active power and rms value control: P_{ref} is kept constant at 1.0 pu while $E^{\text{ref}}_{\text{rms}}$ is changed from 1.0 pu to 0.8 pu. Note that the time resolution differs in the two graphs.

i^{ref}_d drops 0.14 pu when the reference is changed and uses about 1.0 second to return to its former value. i_d has a small increase lasting about 0.02 seconds before it returns to the reference value from before the change. This corresponds very well to the lapse of the active power. While i^{ref}_d is lower than in steady-state and i_d has taken the steady-state value, there is a quite large error in the d axis current controller. The q axis voltage reference is affected by the reference change in about 0.01 second, while the d axis voltage finds a new value after about the same period of time.

In this simulation case the active power and rms value controllers worked satisfactory.

Figure 8.13 shows a more extreme situation. At the same instant P_{ref} is changed from 1.0 pu to -4.0 pu and $E^{\text{ref}}_{\text{rms}}$ changed from 0.4 pu to 1.1 pu. The upper plots

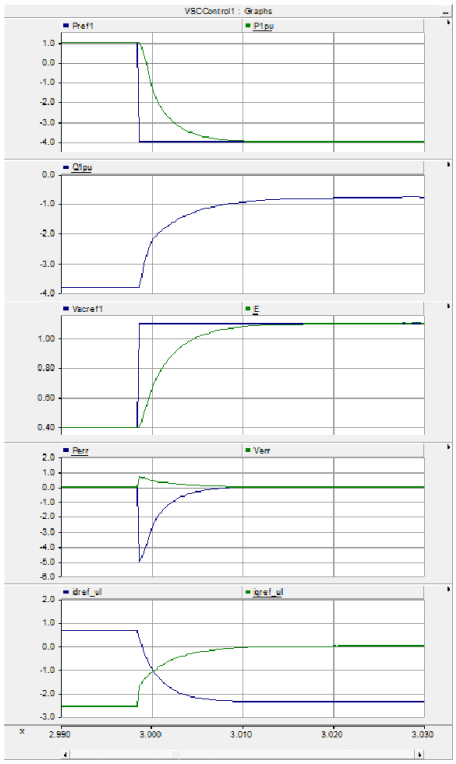

(a) Active power and rms value control: Top: P_{ref} and P, second: Q, third: $E_{\text{rms}}^{\text{ref}}$ and E_{rms}, forth: $P_{\text{err}} = P_{\text{ref}} - P$ and $E_{\text{rms}}^{\text{err}} = E_{\text{rms}}^{\text{ref}} - E_{\text{rms}}$, bottom: the unlimited current references $i_{\text{d,ref\_ul}}$ and $i_{\text{q,ref\_ul}}$

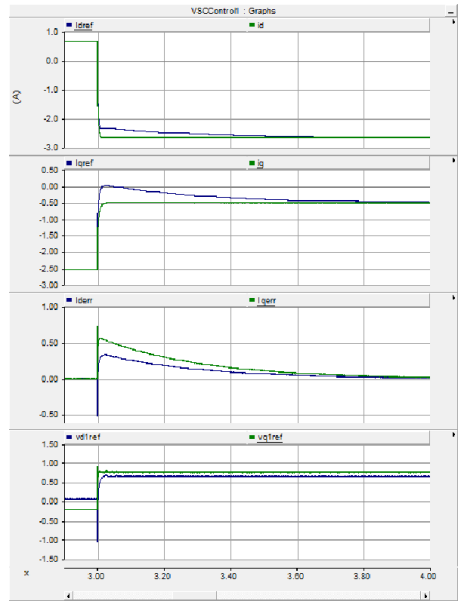

(b) Resulting currents: Top: i_d^{ref} and i_d, second: i_q^{ref} and i_q, third: $i_d^{\text{err}} = i_d^{\text{ref}} - i_d$ and $i_q^{\text{err}} = i_q^{\text{ref}} - i_q$, bottom: $e_{\text{Vd}}^{\text{ref}}$ and $e_{\text{Vq}}^{\text{ref}}$.

Figure 8.13: Simulation 2 with active power and rms value control: P_{ref} is changed from 1.0 pu to -4.0 pu and $E_{\text{rms}}^{\text{ref}}$ is changed from 0.4 pu to 1.1 pu. Note that the time resolution differs in the two graphs.

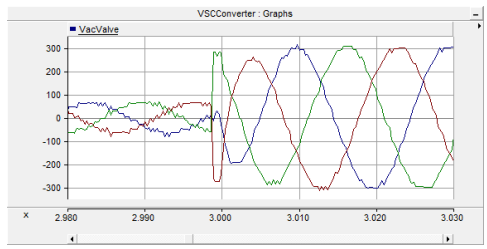

Figure 8.14: The three phases of the voltage [kV] at the converter terminal corresponding to Figure 8.13

of Figure 8.13a show that both active power and rms value use slightly more than 0.01 seconds to adjust to the new references. The reactive power increases from -3.80 pu to -0.78 pu. This takes about 0.02 seconds.

The same trend that was seen with the currents in Figure 8.9b is observed in Figure 8.13b: The currents i_d and i_q take on new values rapidly, here in about 0.01 seconds, and the values are kept approximately constant after that. The current references however, use about 1.0 second to adjust.

Both i_d and i_d^{ref} drop at the reference change, but i_d^{ref} takes a value that is approximately 0.3 pu higher than i_d and uses time to decrease. i_q and i_q^{ref} increase, and i_q^{ref} takes a value that is 0.5 pu higher than i_q and then gradually decreases. The voltage references use about 0.02 seconds to adjust to new and constant values.

Figure 8.14 show the three phases of the voltage at the converter terminal for the case in Figure 8.13. It can be seen that the voltage uses less than 0.01 seconds to achieve a sinusoidal wave shape. This is considered acceptable.

Also in this more extreme case, the active power and rms value controllers worked satisfactory. It is therefore concluded that the implementation of the control system for active power and rms value is successful.

Even though the tuning of the rms value control loop was operation point dependent, the controller has proved effective for a large range of values. Only voltages between 0.75 pu and 1.15 pu are relevant with realistic current limits. The simulations show that this is absolutely manageable. The bode plot for the loop showed a somewhat smaller phase margin that what is desired. However, the testing described here showed no sign of stability problems.

The successful implementation of this control loop combination demonstrates that it is possible to control parameters at different locations in the network using a decoupled control system and PI controllers. Usually all control actions in a control system are influencing the same point in the network. The possibility of controlling two different points shows the powerfulness of the PI controller. This feature can be desirable in real life applications, if not for the conventional operation, at least as an additional control possibility.

Remark on the Lapses of the Current References

The q axis current reference in Figure 8.8 and the d axis current reference in Figure 8.12 have quite equal lapses after the reference change in the outer controller of the other axis loop. In Figure 8.9 and Figure 8.13 both outer loop references were changed, and it is therefore not possible to determine which of the changes that caused the effects in current loops. It is likely, however, based on Figure 8.8 and Figure 8.12 that the effect occurs in the opposite axis from the change. Hence it may be related to some sort of decoupling problem in the control system. The particular about the effect is that the current signal itself is not affected, only the reference. Accordingly no problems or instabilities are created due to this behaviour. It is therefore rather regarded as a curiosity, than a problem.

8.2.4 Chancing the Control Mode in the Q Axis

The control mode can be changed during the simulation run. To enable this, an additional signal was added to the logic signal used for resettable integrator. This would ensure that the value of the error signal while the control loop is passive would not affect the output when the control loop is activated.

Examples of the possibilities are shown in Figure 8.15. It can be seen that the active power is very much affected by the reference change, but the effect lasts shortly and the active power returns to the reference.

This possibility shows that the control system is very successfully decoupled. Even if there is a small disturbance in the active power at the reference change, all values return to the references quite rapidly. The change of control mode represents no danger for the stability of the control system. Even if this feature is not very applicable in real life applications, it shows a strength of the control system, both concerning decoupling and robustness.

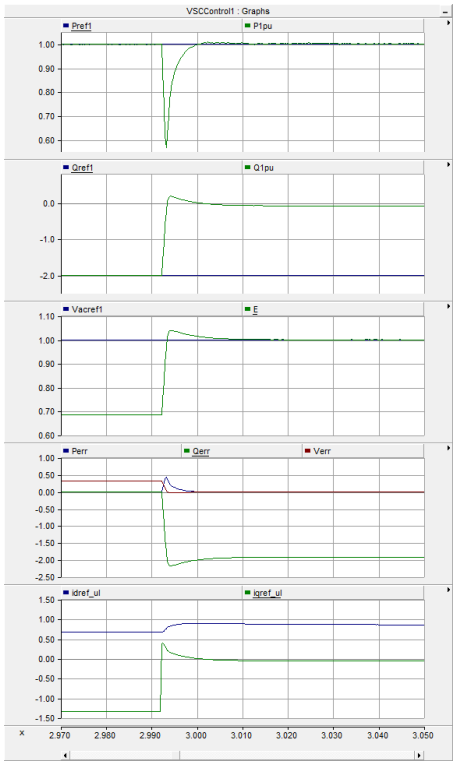

(a) Change from reactive power control ($Q_{\text{ref}} = -2.0$ pu) to rms value control ($E^{\text{ref}}_{\text{rms}} = 1.0$ pu)

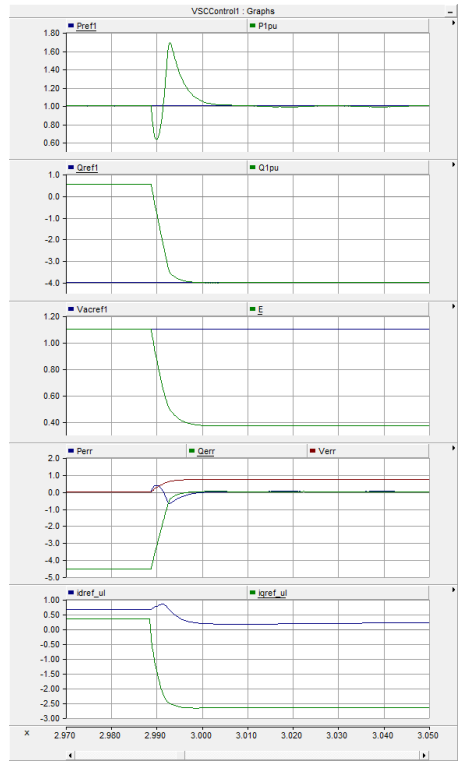

(b) Change from voltage control ($E^{\text{ref}}_{\text{rms}} = 1.1$ pu) to reactive power control ($Q_{\text{ref}} = -4.0$ pu)

Figure 8.15: Simulations with change of q axis reference: Top: P_{ref}=1.0 pu and P, second: Q_{ref} and Q, third: $E^{\text{ref}}_{\text{rms}}$ and E_{rms}, forth: $P_{\text{err}} = P_{\text{ref}} - P$, $Q_{\text{err}} = Q_{\text{ref}} - Q$, and $E^{\text{err}}_{\text{rms}} = E^{\text{ref}}_{\text{rms}} - E_{\text{rms}}$, bottom: the unlimited current references $i_{\text{d,ref\_ul}}$ and $i_{\text{q,ref\_ul}}$

Chapter 9

Discussion

9.1 Voltage Investigations

The investigation of available voltage range showed that the relationship between modulation index and terminal voltage was as expected. Hence, the simulation model works in the manner one would expect based on power electronic equations.

The comparison of distinct voltage values was more challenging. In the theoretical calculations in Chapter 3, the rms line voltage in the fundamental frequency was chosen as the basis for comparison. The calculation was done based on the phase voltages. The rms voltage calculated by the multimeter block in PSCAD is based on all harmonic components. Unless there is no harmonic distortion, this will give a value higher than the basis for comparison from Chapter 3. The simulations in Chapter 7 revealed that the measured rms voltage is depending on angle δ, and this is an additional element of uncertainty in the comparison.

The THD calculation showed that the harmonic content in the simulation voltages was low. Hence the rms value based on all harmonics is quite similar to the rms value containing only first harmonic. The fact that the results from the curve fitting gave lower rms values than the simulations is probably partly due to the difference in calculation method. The low number of submodules used in the insertion curves resulted in higher harmonic content and accordingly larger difference the semi-analytical results and the simulation results. For future analysis, a better and more comparable basis should be chosen.

For the case with third harmonic distortion, the phase voltage is an unfortunate parameter, as only the line voltage is able to cancel out the third harmonic content. The curve fitting performed in Chapter 3 therefore gives an unsatisfactory basis for comparison. It was seen in the simulation in Chapter 6 that this modulation combination gave a much higher rms voltage than predicted in Chapter 3.

Adding third harmonic distortion to the reference voltage proved to be a better option than expected. The resulting rms voltage was high, and this modulation case also gave the lowest THD. This could be an argument for further optimizing of the reference voltage wave fed into the lower level control system of the con-

verter. Reduced harmonic content would lead to reduced need for filtering and hence the inductance between the converter and the grid could be reduced. As seen in Chapter 4, this would give increased power delivered to the grid.

It could be argued that more information about a voltage than the peak or rms value should be available when comparing two different modulation possibilities. A parameter used to describe the share of first harmonic content compared to other harmonics, would make it possible to develop a much more qualitative comparison. If a new basis for comparison was to be developed, it should focus on line voltage as this gives a much more correct picture of the third harmonic distortion. In the simulation model a comparison basis independent of angle δ should be chosen. If the approach used in the semi-analytical method proves unsuitable for this type analysis, a new and more sophisticated approach should be developed. The number of submodules used in the theoretical evaluations compared to the simulation model should be reconsidered.

9.2 Power Investigations

The power relationships were derived using general formulas, but only visualized and tested with case specific values. This gives limited knowledge about the consequences of other network conditions. The optimization of inductance value gave some insight in the consequence of reduced inductance, which showed a large increase in both active and reactive power. As long as the transformer is connected between the converter and the grid, there is a limit for the possible inductance reduction. Investigations on the filter were not performed. As the simulation model was based on a stiff grid connection, this was the only case visited in the theoretical part. Connecting the converter to a weak grid would require further investigations. The considerations in Chapter 4 were done without considering the resulting current values and whether these are realistic. The calculations were also done for a wide range of voltage and angle values outside the stable operation range. This was not done to suggest possible operation states, but rather to identify the present relations.

In a grid context it is beneficial that the converter can deliver reactive power, as this can be regarded as voltage support in the grid. This is possible for certain combinations of converter terminal voltages and gird angles. The converter terminal voltage should be kept higher than the grid voltage, while the grid angle must be close to zero.

The active power at the stiff gird and the converter terminal were found to have very similar values. This is because of the low filter resistance. A larger filter resistance would shift the power curves relative to angle δ, and the stable operation area would be reduced. The difference in reactive power at the two locations is due to the inductance value in the filter and the transformer. A large amount of reactive power is consumed between the two points when the current is high.

The optimization process showed the importance of the ratio between the inductance and the resistance. This ratio defines the stable operation range in addition to the location of maximum reactive power. Both the impedance expressions for

power maximization were proportional to the resistance. The inductance resistance ratio cannot easily be changed in a real life network, but the knowledge of its importance is still relevant. The angles defining the stability limits were found to be different for the two power equations and also different from the classical range $[-90°, 90°]$. This is because of the resistance in the case circuit. Only the positive maximum for reactive power is found in the stable operation area. The possible consumption of reactive power is hence limited by the stability limit. This is beneficial in a grid context.

The optimizations of the inductance value showed that the optimal case for the power transfer is tiny inductance values for most grid angels. This resulted in very high power values. The feasibility of this type of operation is not considered. Large power values result in very large current values. The result is therefore considered less relevant for real life applications.

The simulations in Chapter 7 showed that the converter terminal voltage was depending on the grid angle. In the modelling the converter was regarded as an ideal voltage source, and the result was therefore surprising. A suggested explanation is that the converter could be modelled as a voltage source behind an impedance, but further investigations are needed to verify this. The consequence of reduced terminal voltage was reduced reactive and apparent power, and hence the simulation results fitted poorer with the theoretical curves. When this effect was compensated, the simulation results fitted very well with the theoretical curves. As the reason for this effect is not fully revealed, it is difficult to predict whether it would also be the case for real life converters. If it is, the theoretical model should be changed to better represent the actual conditions. With a proper model, it might even be possible to compensate the effect.

It was seen that the effect of the magnetizing power was very small compared to other power values, and it was therefore possible to disregard this effect. As the magnetizing is an important part of a transformer, this is perhaps not a perfect model. The magnetizing inductance was also found to be slightly lower than recommended in literature. If the simulation model is modified, it might be considered to increase the magnetizing effect by reducing the size of the magnetizing inductance.

9.3 Control System

The control system was based on the mathematical model in the dq reference frame. This gives a possibility to tune the controllers with process specific parameters and to calculate feed-forward loops as the disturbances are known. Only the tuning process of the rms value loop was affected by operation point sensitive parameters. This is a large benefit for the stable operation range for the controllers.

The tuning of the current loops was done using modulus optimum. This ensures fast inner loops, which is important in a cascaded structure. The power loops were tuned using that the crossover frequency should be one order of magnitude smaller in the outer loop than in the inner loop. The fastness of these loops is hence depending on the fastness of the current loops. The rms value control loop

was tuned using symmetric optimum, which gives maximized phase margin and robustness against disturbances. The bode plot showed that even when this tuning technique was used, the phase margin was slightly smaller than what is desirable. A different tuning objective could therefore have been critical for the stability of this control loop.

The current and power control loops were implemented as described in the in Chapter 5. The rms value control loop was implemented with opposite controller gain sign. This is related to the fact that the angles σ and δ rotate in opposite directions in the simulation model. The feedback signal for the rms value control loop was also changed. Instead of using the measured converter terminal voltage, a calculated voltage based on the stiff grid voltage, and current and impedance values was used. This corresponds to including a time delay in the feedback. With this calculation both the feedback signal for active power and for rms voltage were taken from the same location and hence affected by the same time delay. After these changes were performed, all five control loops functioned quite well in simulations.

The fact that the combination of the active power control and rms value control is possible, demonstrates that it is possible to control parameters at two different locations in the network. The standard control method is to control parameters at only one location. The possibility of controlling parameters at two different locations is an interesting feature, also for real life applications. It can introduce flexibility in the control system and open for additional control possibilities. This was probably possible due to the appropriateness of the PI controller. It shows that this controller type is able to handle different control system structures when properly tuned.

Some strange effects were seen on the current references when the reference of the opposite axis outer loop was changed. This effect only affected the current references, not the currents, and therefore not the operation of the converter. The reason for this effect is assumed to be some sort of decoupling problem, but as the effect has no practical importance, it was not further investigated. In the implementation process it was observed that the feedback signals in the outer loops came faster back to the reference values after a reference change than the feedback signals in the inner loops. These two observations might be related.

The testing of the control system showed the importance of signal limiters. If the current references were unlimited and the errors in the outer loops large, there would be a large error in the current loops. This would result in over-modulation and in some cases even unstable operation. It also proved very important to avoid wind-up in the control system. Especially when the control mode was changed during the run, the error that arise when the loop is passive, should have no influence on the loop behaviour when the loop becomes activated. The current magnitude limit is the single factor determining the apparent power available at the stiff grid. With realistic current limitations, the apparent power would have been reduced a quite a lot compared to what the simulations showed. The large limit values were used to test what the converter model was able to handle, more than to test realistic operation for a real life converter. Also the simulations shown were done with changes much larger than what would be possible in a real power system. This was

done to test the control system in a worst case situation. If the control system is stable for such large reference changes, it would also be stable with smaller changes. By handling the large changes in references, the control system proved to be robust and independent of operation point.

Two concerns were raised regarding the rms value control loop in Chapter 5. The first was that the tuning was operation point dependent. The second was that the phase margin was not as high as desired. Simulations showed that the control loop was stable for a large range of values. This suggests that the controller is able to operate successfully in spite of the two mentioned concerns.

The fact that it was possible to change the control mode for the outer q axis control loop during a simulation demonstrated the successful decoupling in the control system. Even if the d axis signal, active power, was affected by the change, it quickly found back to its reference value and the control system stayed stable. This is rather a test of the robustness of the control system, than a useful application.

Conclusion

Many properties of the MMC have been illustrated and explained. Theoretical evaluations and simulation results have been compared to examine the similarity. It is desired that the simulation model reflects the properties of a real life converter, to make the analysis valid also in that context.

It was verified that the converter had a classical modulation curve with a linear relationship between modulation index and voltage until over-modulation is reached. In the over-modulation range the voltage curve flattens as no more voltage can be generated from the converter. Qualitative comparisons of theoretically developed voltage wave shapes with simulation results based on different modulation indexes was successful, but quantitative comparisons proved challenging for a number of reasons. The modulation with third harmonic distortion showed very advantageous properties in the simulations, with both high rms voltage and low THD.

In general, the power output from the simulation model of the converter fitted well with the results from calculations. Both equations and simulations show that large amounts of reactive power are consumed between the converter and the grid. This is disadvantageous as reactive power delivered to the grid gives voltage support. There was a small reduction in active power between the converter and the grid due to the filter resistance. The consequence of this was that the angle range defining stable operation was slightly reduced as the stability limitation was given by the angle stability limit for power systems. The ratio between the inductance and the resistance was found to have large influence on the characteristics of the network. The theoretical analysis was done disregarding the magnetizing effect in the transformer. Simulations verified that this was an appropriate approximation. In the simulations the converter terminal voltage proved to be depending on the grid angle. This was not in accordance with the model that was assumed in the theoretical analysis. The changes in terminal voltage affected the values of reactive and apparent power.

A mathematical model for the MMC was described and used as basis for the development of the control system. The control system was made with a cascaded structure in the dq reference frame. The inner loops controlling the currents were tuned with modulus optimum to ensure fastness. For the outer loops there were two different control possibilities: active and reactive power control or active power and rms value control. The structure and parameters of the two power loops were

found to be equal. They were tuned using that the crossover frequency should be one order of magnitude smaller for the outer than the inner loop. The rms value control loop was tuned with symmetric optimum as phase margin maximization was necessary with this transfer function structure. Only the tuning of the rms value control loop was affected by operation sensitive parameters. The tuning of the four other loops is valid for every operation point. The control loops were successfully implemented into the simulation model, and the feedback signals were able to follow the reference values in a large range of operation points. While the values for active and reactive power were controlled at the stiff grid, the rms value was controlled at the converter terminal. The fact that this implementation shows good simulation performance, demonstrates that it is possible to control two parameters located differently in the process. This shows the powerfulness of the PI controller. It was also proved possible to change between the two control modes. For this to be realizable the decoupling of the control system must be very good. The successful control mode change also demonstrates that the implemented control system is quite robust.

Many of the properties of the MMC have been clarified, regarding voltage range, power relationships and control system. Yet, there are unanswered questions, for instance; how to optimize the reference voltage wave shape, what will happen if the converter is connected to a grid that is not stiff, and how can the terminal voltage experienced in simulations be modelled properly. Such questions are important to address in the future, as the MMC technology is on its way into the real life power systems.

Further Work

Further work can be divided into three parts, mirroring the three topics stated in the Introduction.

Regarding the terminal voltage and modulation, a more knowledge-based method for choosing the reference voltage wave shape should be developed. This requires development of a new comparison basis that contains information about both peak or rms value and harmonic content. If possible, the measurement of the parameters should be independent of angle δ in the simulation model. This new information should be used to optimize the voltage wave shape at the converter terminal. When the voltage wave shape is improved, the need for filtering should be discussed. A reduction of the filter parameters would be beneficial for the power flow from the converter to the grid.

If a real life converter is to be implemented in the grid, it will most likely not be connect to a stiff grid. This actualizes the need for investigating the network properties with different parameters. The investigation should be done both analytically and in simulations. The reason for the variations in the terminal voltage should be revealed. If the effect is considered likely to appear in real life converters, a new theoretical model must be developed to take the effect into account. In this way a method for compensating the effect can be determined. If it turns out that the effect only appears in the simulation model, the model should be changed.

As the simulation model now has a functioning control system, there are no limitations to the simulations that can be run. These simulations could identify the consequences connecting a MMC to a real power grid. Simulation cases should include different fault situations in the AC grid and for instance inspect if the converter control system is fast enough to support the grid voltage. Simulations with the converter connected to a weak grid should also be run. The converter behaviour in many different operation cases relevant for power systems can be tested.

References

[1] Statnett. *Skagerrak 4*. 2012. URL: http://www.statnett.no/no/Prosjekter/Skagerrak-4/.

[2] ABB. *Skagerrak HVDC Interconnections*. 2012. URL: http://www.abb.com/industries/ap/db0003db004333/448a5eca0d6e15d3c12578310031e3a7.aspx.

[3] Siemens. *2010 Trans Bay Cable Project, USA*. 2012. URL: http://www.energy.siemens.com/hq/en/power-transmission/hvdc/hvdc-plus/references.htm#content=2010%20Trans%20Bay%20Cable%20Project%2C%20USA.

[4] A. Lesnicar and R. Marquardt. "An Innovative Modular Multilevel Converter Topology Suitable for a Wide Power Range". In: *IEEE Power Tech Conference, Bologna, Italy*. 2003.

[5] E. Abildgaard. *HVDC Transmission Systems Based on the Use of Modular Multilevel Converters (MMCs)*. Specialization Project. Norwegian University of Science and Technology, Department of Electrical Engineering, 2011.

[6] P. Kundur. *Power System Stability and Control*. Tata McGraw-Hill Publishing Company Limited, 2006.

[7] J. G. Balchen, T. Andresen, and B. A. Foss. *Reguleringsteknikk*. 5th edition. Institutt for teknisk kybernetikk, NTNU, 2003.

[8] J. W. Umland and M. Safiuddin. "Magnitude and Symmetric Optimum Criterion for the Design of Linear Control Systems: What Is It and How Does It Compare with the Others?" In: *IEEE TRANSACTIONS ON INDUSTRY APPLICATIONS* 26.3 (1990).

[9] C. Bajracharya. "Control of VSC-HVDC for Wind Power". MA thesis. Norwegian University of Science and Technology, Department of Electrical Power Engineering, 2008.

[10] S. Norrga. "VSC HVDC - Past , Present and Future". Presentation at the 14th European Conference on Power Electronics and Applications, EPE'11. 2011.

[11] K. Friedrich. "Modern HVDC PLUS Application of VSC in Modular Multilevel Converter Topology". In: *IEEE International Symposium on Industrial Electronics (ISIE)*. 2010.

[12] S. Cole and R. Belmans. "Transmission of Bulk Power: The History and Applications of Voltage-Source Converter High-Voltage Direct Current Systems". In: *IEEE Ind. Electron. Mag* (2009), p. 6.

[13] B. Jacobson et al. "VSC-HVDC Transmission with Cascaded Two-Level Converters". In: *CIGRÉ B4-110*. 2010.

[14] C.C. Davidson and D.R. Trainer. "Innovative Concepts for Hybrid Multi-Level Converters for HVDC Power Transmission". In: *9th IET International Conference on AC and DC Power Transmission (ACDC 2010)*. 2010.

[15] Alstom Grid. *Multi-Terminal HVDC System for Large Offshore Wind Park Grid Integration*. 2010. URL: http://www.alstom.com/WorkArea/DownloadAsset.aspx?id=8589941168.

[16] ABB. *Differences Between HVDC Light and Classic HVDC*. 2011. URL: http://www.abb.com/industries/ap/db0003db004333/b8a81e7c435f37bac125755800373a31.aspx.

[17] U. N. Gnanarathna, A. M. Gole, and R. P. Jayasinghe. "Efficient Modeling of Modular Multilevel HVDC Converters (MMC) on Electromagnetic Transient Simulation Programs". In: *IEEE TRANSACTIONS ON POWER DELIVERY* 26.1 (2011), pp. 316–324.

[18] A.M. Cross, D.R. Trainer, and R.W. Crookes. "Chain-Link Based HVDC Voltage Source Converter Using Current Injection". In: *9th IET International Conference on AC and DC Power Transmission (ACDC 2010)*. 2010, p. 5.

[19] ABB. *HVDC Reference Projects, Jinping - Sunan*. 2011. URL: http://www.abb.com/industries/ap/db0003db004333/545527721af2bf14c12578690049fea4.aspx.

[20] Siemens. *HVDC PLUS - References*. 2011. URL: http://www.energy.siemens.com/fi/en/power-transmission/hvdc/hvdc-plus/references.htm.

[21] Siemens. *HV Direct Current Transmission System (HVDC)*. 2011. URL: http://www.energy.siemens.com/fi/en/power-transmission/hvdc/.

[22] ABB. *Ultra High Voltage DC Systems*. 2011. URL: http://www.abb.com/industries/db0003db004333/542b81305d650581c12574a9002560fd.aspx.

[23] ABB. *HVDC Light*. 2011. URL: http://www.abb.com/industries/us/9AAC30300394.aspx.

[24] A. Nabae, I. Takahashi, and H. Akagi. "A New Neutral-Point-Clamped PWM Inverter". In: *IEEE TRANSACTIONS ON INDUSTRY APPLICATIONS* lA-17.5 (1981), pp. 518–523.

[25] N. S. Choi, J.G. Cho, and G. H. Cho. "A General Circuit Topology of Multilevel Inverter". In: *Proc. IEEE 22nd Power Electron. Sepc. Conf., PESC'91*. 1991.

[26] A. Schiop and P. Scortaru. "Simulink Model of Flying Capacitor Multilevel Inverter". In: *Optimization of Electrical and Electronic Equipment, 2008. OPTIM 2008. 11th International Conference on*. 2008, pp. 203–208.

[27] V. Blasko and V. Kaura. "A New Mathematical Model and Control of a Three-Phase AC-DC Voltage Source Converter". In: *IEEE TRANSACTIONS ON POWER ELECTRONICS* 12.1 (1997), pp. 116–123.

[28] J. C. Garcia. *Multi-Terminal HVDC VSC PSCAD Model Components and Systems to Support the 3- and 5 Terminal Studies in Sweden and Norway*. Tech. rep. Manitoba HVDC Research Centre, 2011.

[29] N. Mohan, T. M. Undeland, and W. P. Robbins. *Power Electronics - Converters, Applications and Design*. Third Edition. John Wiely and Sons, Inc., 2003.

[30] J. A. Houldsworth and D. A. Grant. "The Use of Harmonic Distortion to Increase the Output Voltage of a Three-Phase PWM Inverter". In: *IEEE Transactions On Industry Applications* IA-20.5 (1984), pp. 1224–1228.

[31] J. Machowski, J. W. Bialek, and J. R. Bumby. *Power System Dynamics, Stability and Control*. 2nd edition. Wiley, 2008.

[32] L. Zhang, H.-P. Nee, and L. Harnefors. "Analysis of Stability Limitations of a VSC-HVDC Link Using Power-Synchronization Control". In: *IEEE TRANSACTIONS ON POWER SYSTEMS* 26.3 (2011), pp. 1326–1337.

[33] V. Blasko and V. Kaura. "A New Mathematical Model and Control of a Three-Phase AC-DC Voltage Source Converter". In: *IEEE Transactions on Power Electroncs* 12.1 (1997), pp. 116–123.

[34] A. Antonopoulos, L. Angquist, and H.-P. Nee. "On Dynamics and Voltage Control of the Modular Multilevel Converter". In: *13th European Conference on Power Electronics and Applications, 2009. EPE '09.*

[35] A. Greenwood. *Electrical Transients in Power Systems*. Wiley, 1991.

[36] O. Egeland and J. T. Gravdahl. *Modeling and Simulation for Automatic Control*. Marine Cybernetics AS, 2002.

Appendices

Appendix A

Park's Transformations

A.1 Voltage Invariant Transformation

The transformation from the *abc* to th dq0 system is done using the rotation matrix T [6]. 0 is the zero-sequence coordinate. This coordinate is included to make the transformation unique [31].

$$\begin{bmatrix} v_d \\ v_q \\ v_0 \end{bmatrix} = T \begin{bmatrix} v_a \\ v_b \\ v_c \end{bmatrix} = \frac{2}{3} \begin{bmatrix} \cos(\theta) & \cos(\theta - \frac{2\Pi}{3}) & \cos(\theta + \frac{2\Pi}{3}) \\ \sin(\theta) & \sin(\theta - \frac{2\Pi}{3}) & \sin(\theta + \frac{2\Pi}{3}) \\ \frac{1}{2} & \frac{1}{2} & \frac{1}{2} \end{bmatrix} \begin{bmatrix} v_a \\ v_b \\ v_c \end{bmatrix} \tag{A.1}$$

The inverse transformation is done using T^{-1}:

$$\begin{bmatrix} v_a \\ v_b \\ v_c \end{bmatrix} = T^{-1} \begin{bmatrix} v_d \\ v_q \\ v_0 \end{bmatrix} = \begin{bmatrix} \cos(\theta) & \sin(\theta) & 1 \\ \cos(\theta - \frac{2\Pi}{3}) & \sin(\theta - \frac{2\Pi}{3}) & 1 \\ \cos(\theta + \frac{2\Pi}{3}) & \sin(\theta + \frac{2\Pi}{3}) & 1 \end{bmatrix} \begin{bmatrix} v_d \\ v_q \\ v_0 \end{bmatrix} \tag{A.2}$$

The transforms in Equations A.1 and A.2 are valid for both current and voltage.

$$TT^{-1} = I \tag{A.3}$$

Where I is the identity matrix.

A.2 Active and Reactive Power

Three-phase real and reactive power are given as:

$$P = 3|V||I|\cos(\phi) \tag{A.4}$$

$$Q = 3|V||I|\sin(\phi) \tag{A.5}$$

where ϕ is the angle between the current and the voltage. Only the component of the current that is in phase with the voltage contributes to the real power.

If $\phi = 0°$ so that every voltage and current are in phase, the active power is given by:

$$P = v_a i_a + v_b i_b + v_c i_c = \begin{bmatrix} v_a & v_b & v_c \end{bmatrix} \begin{bmatrix} i_a \\ i_b \\ i_c \end{bmatrix} \tag{A.6}$$

$$\begin{bmatrix} v_a & v_b & v_c \end{bmatrix} = [[T^{-1}] \begin{bmatrix} v_d \\ v_q \\ v_0 \end{bmatrix}]^T = \begin{bmatrix} v_d & v_q & v_0 \end{bmatrix} [T^{-1}]^T \tag{A.7}$$

This gives:

$$P = \begin{bmatrix} v_a & v_b & v_c \end{bmatrix} \begin{bmatrix} i_a \\ i_b \\ i_c \end{bmatrix} = \begin{bmatrix} v_d & v_q & v_0 \end{bmatrix} [T^{-1}]^T [T^{-1}] \begin{bmatrix} i_d \\ i_q \\ i_0 \end{bmatrix} = \begin{bmatrix} v_d & v_q & v_0 \end{bmatrix} \begin{bmatrix} \frac{3}{2} & 0 & 0 \\ 0 & \frac{3}{2} & 0 \\ 0 & 0 & 3 \end{bmatrix} \begin{bmatrix} i_d \\ i_q \\ i_0 \end{bmatrix} \tag{A.8}$$

$$P = \frac{3}{2}(v_d i_d + v_q i_q + 2 v_0 i_0) \tag{A.9}$$

In the symmetrical case $v_0 = i_0 = 0$. Equation A.9 shows how active power is calculated from aligned components.

If $\phi = 90°$ so that active power equals zero, then the reactive power is given as:

$$Q = \begin{bmatrix} v_a & v_b & v_c \end{bmatrix} \begin{bmatrix} i_a \\ i_b \\ i_c \end{bmatrix} \tag{A.10}$$

$$\begin{bmatrix} v_a & v_b & v_c \end{bmatrix} = \begin{bmatrix} v_d & v_q & v_0 \end{bmatrix} [T^{-1}]^T = \begin{bmatrix} v_d & v_q & v_0 \end{bmatrix} \begin{bmatrix} \cos(\theta) & \cos(\theta - \frac{2\Pi}{3}) & \cos(\theta + \frac{2\Pi}{3}) \\ \sin(\theta) & \sin(\theta - \frac{2\Pi}{3} & \sin(\theta + \frac{2\Pi}{3}) \\ 1 & 1 & 1 \end{bmatrix} \tag{A.11}$$

As the current lags the voltage, the angular distance to the d axis is increased with $\frac{\pi}{2}$.

$$\begin{bmatrix} i_a \\ i_b \\ i_c \end{bmatrix} = \begin{bmatrix} \cos(\theta + \frac{\Pi}{2}) & \sin(\theta + \frac{\Pi}{2}) & 1 \\ \cos(\theta - \frac{2\Pi}{3} + \frac{\Pi}{2}) & \sin(\theta - \frac{2\Pi}{3} + \frac{\Pi}{2}) & 1 \\ \cos(\theta + \frac{2\Pi}{3} + \frac{\Pi}{2}) & \sin(\theta + \frac{2\Pi}{3} + \frac{\Pi}{2}) & 1 \end{bmatrix} \begin{bmatrix} i_d \\ i_q \\ i_0 \end{bmatrix} \tag{A.12}$$

$$Q = \begin{bmatrix} v_d & v_q & v_0 \end{bmatrix} \begin{bmatrix} \cos(\theta) & \cos(\theta - \frac{2\Pi}{3}) & \cos(\theta + \frac{2\Pi}{3}) \\ \sin(\theta) & \sin(\theta - \frac{2\Pi}{3}) & \sin(\theta + \frac{2\Pi}{3}) \\ 1 & 1 & 1 \end{bmatrix} \begin{bmatrix} \cos(\theta + \frac{\Pi}{2}) & \sin(\theta + \frac{\Pi}{2}) & 1 \\ \cos(\theta - \frac{\Pi}{6}) & \sin(\theta - \frac{\Pi}{6}) & 1 \\ \cos(\theta + \frac{7\Pi}{6}) & \sin(\theta + \frac{7\Pi}{6}) & 1 \end{bmatrix} \begin{bmatrix} i_d \\ i_q \\ i_0 \end{bmatrix} \quad \text{(A.13)}$$

$$Q = \begin{bmatrix} v_d & v_q & v_0 \end{bmatrix} \begin{bmatrix} 0 & \frac{3}{2} & 0 \\ -\frac{3}{2} & 0 & 0 \\ 0 & 0 & 3 \end{bmatrix} \begin{bmatrix} i_d \\ i_q \\ i_0 \end{bmatrix} = \frac{3}{2}(v_d i_q - v_q i_d + 2 v_0 i_0) \quad \text{(A.14)}$$

Also here $v_0 = i_0 = 0$ in the symmetrical case. Equation A.14 shows how reactive power is calculated from oppositely directed components.

The grid voltage vector is defined to be along the d axis. With this alignment $v_q = 0$, and Equations A.9 and A.14 simplifies into:

$$P = \frac{3}{2} v_d i_d \quad \text{(A.15)}$$

$$Q = \frac{3}{2} v_d i_q \quad \text{(A.16)}$$

Equations A.15 and A.16 show that the active and reactive power can be controlled independently, by controlling the grid current.

A.3 Voltage Drop Across an Inductance

The voltage drop across an inductance includes the derivative of the current and this complicates the transformation. v_a, v_b, and v_c are the voltage drops in each phase and i_a, i_b,and i_c are the currents through the inductor, L, in each phase. Theory on differentiations of rotation matrices must be used [36].

$$\begin{bmatrix} v_a \\ v_b \\ v_c \end{bmatrix} = L \begin{bmatrix} \frac{\mathrm{di_a}}{\mathrm{dt}} \\ \frac{\mathrm{di_b}}{\mathrm{dt}} \\ \frac{\mathrm{di_c}}{\mathrm{dt}} \end{bmatrix} \quad \text{(A.17)}$$

$$\begin{bmatrix} v_d \\ v_q \\ v_0 \end{bmatrix} = T \begin{bmatrix} v_a \\ v_b \\ v_c \end{bmatrix} = LT \begin{bmatrix} \frac{\mathrm{di_a}}{\mathrm{dt}} \\ \frac{\mathrm{di_b}}{\mathrm{dt}} \\ \frac{\mathrm{di_c}}{\mathrm{dt}} \end{bmatrix} \quad \text{(A.18)}$$

$$\begin{bmatrix} \frac{\mathrm{di_a}}{\mathrm{dt}} \\ \frac{\mathrm{di_b}}{\mathrm{dt}} \\ \frac{\mathrm{di_c}}{\mathrm{dt}} \end{bmatrix} = \frac{\mathrm{d}}{\mathrm{dt}} \left(T^{-1} \begin{bmatrix} i_d \\ i_q \\ i_0 \end{bmatrix} \right) = T^{-1} \frac{\mathrm{d}}{\mathrm{dt}}(T) T^{-1} \begin{bmatrix} i_d \\ i_q \\ i_0 \end{bmatrix} + T^{-1} \frac{\mathrm{d}}{\mathrm{dt}} \begin{bmatrix} i_d \\ i_q \\ i_0 \end{bmatrix} \quad \text{(A.19)}$$

$$\begin{bmatrix} v_d \\ v_q \\ v_0 \end{bmatrix} = LT\left(T^{-1}\frac{\mathrm{d}}{\mathrm{dt}}(T)T^{-1}\begin{bmatrix} i_d \\ i_q \\ i_0 \end{bmatrix} + T^{-1}\frac{\mathrm{d}}{\mathrm{dt}}\begin{bmatrix} i_d \\ i_q \\ i_0 \end{bmatrix}\right) \tag{A.20}$$

$$\begin{bmatrix} v_d \\ v_q \\ v_0 \end{bmatrix} = L\left(\frac{\mathrm{d}}{\mathrm{dt}}(T)T^{-1}\begin{bmatrix} i_d \\ i_q \\ i_0 \end{bmatrix} + \begin{bmatrix} \frac{\mathrm{d}i_d}{\mathrm{dt}} \\ \frac{\mathrm{d}i_q}{\mathrm{dt}} \\ \frac{\mathrm{d}i_0}{\mathrm{dt}} \end{bmatrix}\right) \tag{A.21}$$

$$\frac{\mathrm{d}}{\mathrm{dt}}T = \frac{\mathrm{d}}{\mathrm{dt}}\frac{2}{3}\begin{bmatrix} \cos(\theta) & \cos(\theta-\frac{2\Pi}{3}) & \cos(\theta+\frac{2\Pi}{3}) \\ \sin(\theta) & \sin(\theta-\frac{2\Pi}{3}) & \sin(\theta+\frac{2\Pi}{3}) \\ \frac{1}{2} & \frac{1}{2} & \frac{1}{2} \end{bmatrix} = \frac{2}{3}\begin{bmatrix} -\sin(\theta) & -\sin(\theta-\frac{2\Pi}{3}) & -\sin(\theta+\frac{2\Pi}{3}) \\ \cos(\theta) & \cos(\theta-\frac{2\Pi}{3}) & \cos(\theta+\frac{2\Pi}{3}) \\ 0 & 0 & 0 \end{bmatrix}\frac{\mathrm{d}\theta}{\mathrm{dt}} \tag{A.22}$$

$$\frac{\mathrm{d}}{\mathrm{dt}}(T)T^{-1} = \frac{2}{3}\frac{\mathrm{d}\theta}{\mathrm{dt}}\begin{bmatrix} -\sin(\theta) & -\sin(\theta-\frac{2\Pi}{3}) & -\sin(\theta+\frac{2\Pi}{3}) \\ \cos(\theta) & \cos(\theta-\frac{2\Pi}{3}) & \cos(\theta+\frac{2\Pi}{3}) \\ 0 & 0 & 0 \end{bmatrix}\begin{bmatrix} \cos(\theta) & \sin(\theta) & 1 \\ \cos(\theta-\frac{2\Pi}{3}) & \sin(\theta-\frac{2\Pi}{3}) & 1 \\ \cos(\theta+\frac{2\Pi}{3}) & \sin(\theta+\frac{2\Pi}{3}) & 1 \end{bmatrix} \tag{A.23}$$

Where $\frac{\mathrm{d}\theta}{\mathrm{dt}} = \omega$.

$$\frac{\mathrm{d}}{\mathrm{dt}}(T)T^{-1} = \frac{2\omega}{3}\begin{bmatrix} 0 & -\frac{3}{2} & 0 \\ \frac{3}{2} & 0 & 0 \\ 0 & 0 & 0 \end{bmatrix} = \begin{bmatrix} 0 & -\omega & 0 \\ \omega & 0 & 0 \\ 0 & 0 & 0 \end{bmatrix} \tag{A.24}$$

$$\begin{bmatrix} v_d \\ v_q \\ v_0 \end{bmatrix} = L\begin{bmatrix} 0 & -\omega & 0 \\ \omega & 0 & 0 \\ 0 & 0 & 0 \end{bmatrix}\begin{bmatrix} i_d \\ i_q \\ i_0 \end{bmatrix} + L\begin{bmatrix} \frac{\mathrm{d}i_d}{\mathrm{dt}} \\ \frac{\mathrm{d}i_q}{\mathrm{dt}} \\ \frac{\mathrm{d}i_0}{\mathrm{dt}} \end{bmatrix} = L\begin{bmatrix} \frac{\mathrm{d}i_d}{\mathrm{dt}} - \omega i_q \\ \frac{\mathrm{d}i_q}{\mathrm{dt}} + \omega i_d \\ \frac{\mathrm{d}i_0}{\mathrm{dt}} \end{bmatrix} \tag{A.25}$$

A.4 Relation to the RMS Value

The phase voltages can be expressed as:

$$v_a = \sqrt{2}V_{\mathrm{rms}}\cos(\omega t) \tag{A.26}$$

$$v_b = \sqrt{2}V_{\mathrm{rms}}\cos(\omega t - \frac{2\pi}{3}) \tag{A.27}$$

$$v_c = \sqrt{2}V_{\mathrm{rms}}\cos(\omega t - \frac{4\pi}{3}) \tag{A.28}$$

$$\begin{bmatrix} v_d \\ v_q \\ v_0 \end{bmatrix} = \frac{2}{3} \begin{bmatrix} \cos(\theta) & \cos(\theta - \frac{2\Pi}{3}) & \cos(\theta + \frac{2\Pi}{3}) \\ \sin(\theta) & \sin(\theta - \frac{2\Pi}{3}) & \sin(\theta + \frac{2\Pi}{3}) \\ \frac{1}{2} & \frac{1}{2} & \frac{1}{2} \end{bmatrix} \begin{bmatrix} \sqrt{2}V_{\text{rms}} \cos(\omega t) \\ \sqrt{2}V_{\text{rms}} \cos(\omega t - \frac{2\pi}{3}) \\ \sqrt{2}V_{\text{rms}} \cos(\omega t + \frac{2\pi}{3}) \end{bmatrix} \tag{A.29}$$

$$\begin{bmatrix} v_d \\ v_q \\ v_0 \end{bmatrix} = \frac{2}{3}\sqrt{2}V_{\text{rms}} \begin{bmatrix} \frac{3}{2}\cos(\theta - \omega t) \\ \frac{3}{2}\sin(\theta - \omega t) \\ 0 \end{bmatrix} = \sqrt{2}V_{\text{rms}} \begin{bmatrix} \cos(\theta - \omega t) \\ \sin(\theta - \omega t) \\ 0 \end{bmatrix} \tag{A.30}$$

It can be seen that:

$$\sqrt{v_d^2 + v_q^2} = \sqrt{2}V_{\text{rms}} \tag{A.31}$$

The d axis is defined to be along the grid voltage vector giving $\theta = \omega t$. With this alignment $v_d = \sqrt{2}V_{\text{rms}}$ and $v_q = 0$.

Appendix B

Case Circuit and Simulation Model Parameters

Rated power	600 MVA
Stiff grid voltage (line to line, rms)	400 kV
Transformer ratio	400:300
Transformer leakage inductance (L_t)	0.1 pu
Filter inductance (L_f)	0.07162 H = 0.15 pu
Filter resistance (R_f)	0.225 Ω = 0.0015 pu
DC voltage (U_D)	600kV
Submodules per multivalve (N)	38
Multivalve inductance (L_{MW})	0.01432 H = 0.030 pu
Cell capacitance (C_{cell})	8867 μF=0.00423 pu

Appendix C

Simulation Results

Table C.1: Modulation index and resulting rms voltage at the converter terminal

e_{Vd}^{ref}	E_{rms} [kV]	$\frac{E_{rms}}{U_D}$
0	9.6	0.0160
0.1	40.6	0.0677
0.2	76.7	0.1278
0.3	113.0	0.1883
0.4	149.5	0.2492
0.5	185.9	0.3098
0.6	222.5	0.3708
0.7	259.1	0.4318
0.8	295.6	0.4927
0.9	332.2	0.5537
1.0	368.7	0.6145
1.1	393.1	0.6552
1.2	408.7	0.6812
1.3	419.8	0.6997
1.4	428.0	0.7133
1.5	433.9	0.7232
1.6	437.9	0.7298
1.7	441.3	0.7355
1.8	442.7	0.7378
1.9	444.0	0.7400
2.0	444.6	0.7410
2.1	444.8	0.7413
2.2	444.9	0.7415
2.3	445.1	0.7418
2.4	445.2	0.7420
2.5	445.3	0.7422

Table C.2: Simulation results with $m = 1$, values at the converter terminal

e_{Vd}^{ref}	e_{Vq}^{ref}	m	σ	δ_{meas}	δ	E_{rms} [kV]	P [MW]	Q [MVAr]	S [MVA]
1.0	0	1.0	0°	−84°	−54°	368.9	-2364.7	1922.0	3047.3
0.92	0.38	1.0	22°	−122°	−92°	364.4	-2870.7	3662.5	4653.5
0.7	0.7	1.0	45°	−155°	−125°	357.5	-2286.2	5066.4	5558.3
0.38	0.92	1.0	68°	180°	210°	355.6	-1385.0	5828.9	5991.2
0	1.0	1.0	90°	166°	196°	355.2	-738.8	6093.7	6138.3
-0.38	0.92	1.0	112°	159°	189°	352.4	-354.9	6100.3	6110.6
-0.7	0.7	1.0	135°	153°	183°	349.8	-77.8	6055.4	6055.9
-0.92	0.38	1.0	158°	148°	178°	351.1	170.9	6087.0	6089.4
-1.0	0	1.0	180°	142°	172°	352.2	432.9	6090.7	6106.1
-0.92	-0.38	1.0	−158°	135°	165°	350.1	789.9	5957.2	6009.3
-0.7	-0.7	1.0	−135°	122°	152°	347.2	1359.0	5650.1	5811.2
-0.38	-0.92	1.0	−112°	100°	130°	348.7	2166.3	5037.7	5483.7
0	-1.0	1.0	−90°	70°	100°	351.6	2812.6	3746.8	4685.0
0.38	-0.92	1.0	−68°	33°	63°	354.8	2560.1	2053.3	3281.8
0.7	-0.7	1.0	−45°	−6°	24°	359.0	1211.1	813.2	1458.8
0.92	-0.38	1.0	−22°	−45°	−15°	366.0	-729.7	745.5	1043.2

Table C.3: Rms value of the terminal voltage with $m = 1.0$ and the PLL voltage at the stiff grid giving $\delta \approx -\sigma$

e_{Vd}^{ref}	e_{Vq}^{ref}	m	σ	E_{rms} [kV]
1.0	0	1.0	0°	366.2
0.92	0.38	1.0	22°	366.4
0.7	0.7	1.0	45°	365.4
0.38	0.92	1.0	68°	366.7
0	1.0	1.0	90°	366.1
-0.38	0.92	1.0	112°	361.6
-0.7	0.7	1.0	135°	356.1
-0.92	0.38	1.0	158°	354.2
-1.0	0	1.0	180°	353.0
-0.92	-0.38	1.0	−158°	349.2
-0.7	-0.7	1.0	−135°	346.8
-0.38	-0.92	1.0	−112°	349.4
0	-1.0	1.0	−90°	352.8
0.38	-0.92	1.0	−68°	354.5
0.7	-0.7	1.0	−45°	356.2
0.92	-0.38	1.0	−22°	361.4

Table C.4: Load flow results with transformer and equivalent inductance

e_{Vd}^{ref}	e_{Vd}^{ref}	m	σ	Case	δ	Converter terminal			Stiff grid		
						V [pu]	P [pu]	Q [pu]	V [pu]	P [pu]	Q [pu]
1.0	0	1.0	0°	Transformer	−1°	1.22	-0.04	1.08	1.00	-0.05	0.88
				Inductance	−1°	1.22	-0.04	1.08	1.00	-0.05	0.88
0.7	0.7	1.0	45°	Transformer	−45°	1.22	-3.41	2.52	1.00	-3.44	-0.53
				Inductance	−45°	1.22	-3.41	2.52	1.00	-3.44	-0.53
0	1.0	1.0	90°	Transformer	270°	1.22	-4.81	5.97	1.00	-4.91	-3.93
				Inductance	270°	1.22	-4.81	5.97	1.00	-4.91	-3.93
-0.7	0.7	1.0	135°	Transformer	225°	1.19	-3.27	9.01	1.00	-3.42	-7.32
				Inductance	225°	1.19	-3.27	9.01	1.00	-3.42	-7.32
-1.0	0	1.0	180°	Transformer	179°	1.18	0.16	10.23	1.00	-0.02	-8.71
				Inductance	179°	1.18	0.16	10.23	1.00	-0.02	-8.71
-0.7	-0.7	1.0	225°	Transformer	134°	1.15	3.44	8.50	1.00	3.29	-7.22
				Inductance	134°	1.16	3.44	8.49	1.00	3.29	-7.22
0	-1	1.0	270°	Transformer	88°	1.18	4.76	5.34	1.00	4.67	-3.90
				Inductance	88°	1.18	4.76	5.34	1.00	4.67	-3.90
0.7	-0.7	1.0	315°	Transformer	43°	1.19	3.30	2.16	1.00	3.27	-0.59
				Inductance	43°	1.19	3.30	2.16	1.00	3.27	-0.59

Appendix D

Values Implemented in the Control System

Current loops

PI controller: $K_p \frac{1+T_i s}{T_i s}$
$K_p = \frac{\tau_{el}}{2T_a \frac{1}{R'}} = 3.205$
$T_i = \tau_{el} = 0.3067$
Feed-forward: Lead lag block: $G \frac{1+sT_1}{1+sT_2}$
$G = -1$
$T_1 = T_a = 1.32 \cdot 10^{-4}$
$T_2 = \alpha T_a = 1.32 \cdot 10^{-5}$

Power loops

PI controller: $K_p \frac{1+T_i s}{T_i s}$
$K_p = \frac{1}{15} = 0.067$
$T_i = 2T_a = 2.64 \cdot 10^{-4}$

Rms value loop

PI controller: $K_p \frac{1+T_i s}{T_i s}$
$K_p = \frac{-C^{\mathrm{MV}}}{K_{\mathrm{RMS}} T_a} = \frac{-1.11 \cdot 10^{-4}}{\frac{1}{\sqrt{2}} 1.32 \cdot 10^{-4}} = 1.19$
$T_i = 8T_a = 1.056 \cdot 10^{-3}$
Feed-forward: Lead lag block: $G \frac{1+sT_1}{1+sT_2}$
$G = 4C^{\mathrm{MV}} = 4.46 \cdot 10^{-4}$
$T_1 = 2T_a = 2.64 \cdot 10^{-4}$
$T_2 = \alpha 2T_a = 2.64 \cdot 10^{-5}$

Appendix E

Paper Presented at Technoport RERC Research 2012, April 16-18, Trondheim

Parts of this thesis were presented at Technoport RERC Research 2012.

Available online at www.sciencedirect.com
ScienceDirect
Energy Procedia 00 (2012) 1–10
Energy Procedia
www.elsevier.com/locate/procedia

Technoport RERC Research 2012

Modelling and Control of the Modular Multilevel Converter (MMC)

Elisabeth N. Abildgaard[a], Marta Molinas[a]

[a]*Department of Electrical Power Engineering, Norwegian University of Science and Technology, O.S. Bragstads plass 2E, 7491 Trondheim, Norway*

Abstract

The Modular Multilevel Converter (MMC) represents an emerging topology with a scalable technology making high voltage and power capability possible. The MMC is built up by identical, but individually controllable submodules. Therefore the converter can act as a controllable voltage source, with a large number of available discrete voltage steps. This characteristic complicates the modelling both mathematically and computational. A mathematical model of the MMC is presented with the aim to develop a converter control system and the model is converted into the dq reference frame. Block diagrams for control of active power and AC voltage magnitude are shown.

Keywords: Modular Multilevel Converter (MMC), HVDC transmission, Voltage Source Converter (VSC), Converter Control, Mathematical modelling

1. Introduction

With new renewable energy production, HVDC is more applicable than ever. More stochastic energy production calls for solutions that can transport power from areas with high generation to areas with lower generation. Offshore wind farms far from the coast require HVDC transmission to the shore and compact and reliable converter technology with large power capability. Connecting the converter to a DC grid should be feasible and the converter should be able to handle fault situations. To gain compactness, the need for filters should be minimized. The emerging topology, the Modular Multilevel Converter (MMC) might address these aims.

1.1. HVDC Converter Technologies

LCC. The thyristors based Load Commutated Converters (LCCs) were introduced during the 1970s. LCC is still the converter that can be built with highest power rating and hence is the best solution for bulk power transmission. Another advantage of LCC is the low losses, typically 0.7 % per converter [1]. The largest

☆

Email address: abildgaa@stud.ntnu.no (Elisabeth N. Abildgaard)
URL: http://www.ntnu.edu/ (Elisabeth N. Abildgaard)

disadvantage is that both the inverter and the rectifier absorb a varying amount of reactive power from the grid, and accordingly adjustable reactive compensation is needed [2]. The LCC will also need an AC voltage source at each terminal to be able to succeed with commutation. In order to minimize the harmonic content, the standard LCC design is made with two 6-pulse bridges in parallel on the AC side and in series on the DC side. The two bridges are phase shifted 30 degrees on the AC side, using transformers [3].

VSC. Classical Voltage Source Converter (VSC) utilizing Insulated Gate Bipolar Transistors (IGBTs) for HVDC applications was introduced in 1997 by the ABB concept HVDC Light [4]. Classical VSC for HVDC applications is based on two-level or three-level converters [4]. With this concept it is not possible to adjust the voltage magnitude at AC terminals, but the voltage can be either $\pm V$ with two-level or $\pm V$ or zero voltage with three-level VSC [2]. Pulse Width Modulation (PWM) is used to approximate the desired voltage waveform and the difference between the desired and implemented waveform is an unwanted distortion which has to be filtered [2]. Because IGBTs have limited voltage blocking capability, they need to be connected in series in two-level and three-level VSCs [4]. In order to limit the voltage across each semiconductor, series connected IGBTs must be switched absolutely simultaneously. This requires sophisticated gate drive circuits to enforce voltage sharing under all conditions [5].

Comparison of LCC and VSC. With VSCs, both active power flow and reactive power flow can be controlled, independently [2], and accordingly no reactive compensation is needed. A VSC station is therefore more compact than a LCC station as the harmonic filters are smaller and no switch yards and capacitor banks are needed [4]. Other advantages with the VSC is that the converter can be connected to weak systems and even to networks lacking generation [4], and as no phase shift is needed, the VSC can use ordinary transformers. A disadvantage is that the VSC has larger losses than LCC, typically 1.7 % per converter [1]. Using LCC, the current direction is fixed and power reversal is done by changing the voltage polarity. With VSCs power reversal is done by changing of the current direction. This makes the VSC technology more suitable for a DC grid application [3]. Cross-linked polyethylene (XLPE) cables can be used with VSCs, but cannot handle the stress from a polarity change. XLPE cables are advantageous as they are less costly, lighter, and smaller in diameter than traditional mass impregnated cables [6]. The power reversal with VSCs can be done gradually because the full range of active power is available, even zero active power can be combined with a positive or negative reactive power. Because both active and reactive power can obtain positive and negative values, the converter is said operate in all four quadrants of the PQ plane [7]. LCCs normally have a minimum active power output 5% below rated power [8]. This makes VSC more favourable for power transmission with varying power e.g. power generated from a wind farm. But an advantage with LCC HVDC is that DC pole to pole short circuit faults can be cleared in the converter station. This is not the case with classical VSC HVDC where in most cases the fault currents must be suppressed by opening the AC breaker feeding the converter [5].

MMC. In 2010 the first Siemens HVDC PLUS system was commissioned, a multilevel VSC technology called MMC [2]. At the same time, ABB updated their HVDC Light product to make use of approximately the same technology [4]. MMCs are built up by a number of identical, but individually controllable submodules. The submodules in the MMC can either be two-level half-bridge converters, each capable of producing +V or zero voltage, or two-level full-bridge converters, producing $\pm V$ or zero voltage [5]. This means that the converter acts as a controllable voltage source with a high number of possible discrete voltage steps. The multilevel topology prevents generation of any major harmonic content [4].

The MMC is a scalable technology. The voltage level determines the number of submodules needed, and the technology can be used up to the highest transmission voltages [9]. The configuration is without series connection of semiconductor switches, and hence problems with simultaneous switching are irrelevant. Losses are lower than for two-level and three-level VSCs, about 1 % per converter [4]. The low losses are obtained by low switching frequency in each submodule and low voltage across each switch [9]. However, as the submodules are switched at different points in time, the effective switching frequency of the converter is high, giving a low harmonic distortion [4].

A MMC with two-level half-bridge submodules requires twice the number of IGBTs of to a two-level VSC of the same rating. For a MMC with two-level full-bridge submodules, the need for IGBTs is twice

as high as with half-bridge submodules [5]. The MMC has no DC link capacitance, but one capacitor in each submodule and these capacitors require both large voltage capacity and large capacitance. The result of many semiconductor switches and capacitors with high ratings is a heavy and bulky circuit, giving a converter that is less compact than the classical VSC, but still more compact than the LCC [5].

The MMC with two-level half-bridges cannot block fault currents during a DC pole to pole fault. With two-level full-bridge submodules the MMC is capable of suppressing the fault current and therefore no AC breaker opening is needed [5]. It can be discussed whether this advantage is large enough to defend the increased number of semiconductors. As both vendors delivering MMC solutions uses two-level half-bridges [2, 4], only this solution will be described in the following.

An advantage with MMCs compared to classical VSC is that the $\frac{dv}{dt}$ on the AC side is reduced as the voltage steps at the terminals are smaller. This enables the use of transformers with lower insulation requirement [10]. Compared to LCC the MMC uses ordinary transformers, no phase shift is needed.

Planned installations in 2011 shows that LCC HVDC can be built with 7200 MW and ±800 kV, while MMC projects are planned with 1000 MW and ±320 kV [11, 12].

Other Converter Technologies. A number of other possible converter topologies has been purposed, such as other multilevel converters and the hybrid converters. Among the most important multilevel topologies are the neutral-point clamped converter [13], the diode-clamped multilevel converter [14], and flying capacitor multilevel converter [15], in addition to the MMC. Hybrid converters can be constructed by combining the advantages of classical VSC and MMC [5]. The aim is to achieve a better output signal than with classical VSC combined with using fewer semiconductor devices than with MMCs. Small MMCs can be used as active filters or wave shaping circuits. Connections can be done in different manners. The MMC is the only one of these topologies applied in commissioned HVDC projects.

1.2. Outline

This paper first describes the operation principle of the MMC. Further the mathematical modelling is shown. Subsequently an approach for simulation of MMCs in an electromagnetic transient (EMT) simulation program is presented. This approach is applicable even for MMCs with a large number of submodules. Finally a control system of the MMC is discussed. This section includes block diagrams for current controllers, active power, and AC voltage magnitude control.

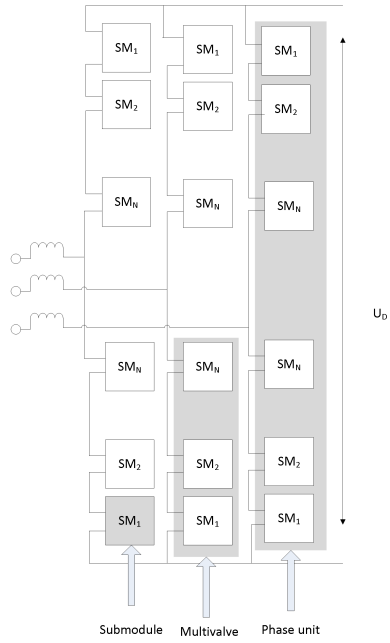

Fig. 1. The MMC Structure

2. The Operation Principle of the MMC

In a three phase MMC, each of the phase units consists of two multivalves, and each multivalve consists of N submodules connected in series (Fig. 1) [9]. With a DC voltage of ±320 kV N=38 is typically required [4]. The half-bridge submodule consists of two valves (T_1 and T_2) and a capacitor (Fig. 2). The valves are made up of an IGBT and a freewheeling diode in antiparallel. In normal operation, only one of the valves is switched on at a given instant in time. Depending on the current direction the capacitor can charge or discharge [9].

When only one IBGT is switched on, either that IGBT or the freewheeling diode in the same valve will conduct, depending on the current direction, and for this reason it makes sense to define a valve as on, indicating that either the IGBT or the diode is conducting [9].

Three possible switching states can be defined [4]:

- In the ON or *inserted* state T_1 is on, and T_2 is off. The submodule output voltage, V_{SM}, equals the capacitor voltage, V_C, and the capacitor charges if the multivalve current is positive and discharges otherwise.
- In the OFF or *bypassed* state T_2 is on, and T_1 is off. The submodule output voltage, V_{SM}, is zero and the capacitor voltage is constant, i.e. the capacitor will not charge nor discharge.
- In the *blocked* state, both valves are off, and the current can only conduct through the freewheeling diodes. The capacitor will charge if the current is positive, but ideally it cannot discharge.

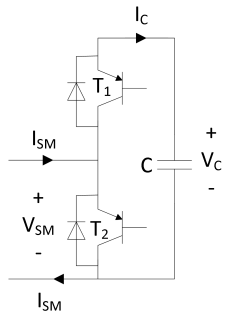

Fig. 2. The Submodule Circuit

The blocking voltage in each phase unit is twice the DC voltage. This can be explained from the situation when all the submodules in the upper multivalve are bypassed, giving a phase voltage equal to the DC voltage. The lower multivalve must be able to block the voltage across itself, i.e. the DC voltage. The result is that each switch must be able to block the DC voltage, U_D, divided by the number of submodules in each multivalve, N, giving $V_{block} = \frac{U_D}{N}$. The capacitors in the lower multivalve will also share the DC voltage and must be dimensioned in the same way as the IGBTs. Considering the same case and a negative I_{SM} relative to Fig. 2, each IGBT in the upper valve must be able to block the voltage across the capacitor in the same submodule. This is one of the reasons why capacitor voltage balancing is important. Both the upper and the lower multivalves should always have half the DC link voltage as average value in order to get a phase output with zero DC offset. The multivalves may take any amplitude between zero and the DC voltage. The sum of inserted submodules in a phase is constant, so inserting a submodule on one multivalve is done simultaneously as bypassing one in the other multivalve of the same phase.

3. Mathematical Modelling of the MMC

Using thyristors, the only controllable parameter is the firing angle, and therefore modelling of the LCC is quite straight forward. For VSC schemes using series connected IGBTs, all the series connected switches are either conducting or blocking. This is utilized in the modelling by defining the share of time the switches are on, the duty ratio [16]. This method cannot be applied for MMCs as some submodules in the multivalve are inserted while others are bypassed. The selection of which submodule to insert or bypass is made on basis of measurements of the capacitor voltages [9]. The capacitor voltages must be kept in a narrow band and this is done through the submodule selection algorithm, using the knowledge of whether a capacitor will charge or discharge given the present current direction.

The following circuit model is developed assuming infinite switching frequency in the converter and infinitive number of submodules per multivalve. These assumptions are made in order to enable the development of a continuous model [17].

Using Kirchhoff's current law in Fig. 3:

$$i_U + i_L = i_v \tag{1}$$

$$i_U = I_{s1} + i_{diff} \tag{2}$$

$$i_L = I_{s2} - i_{diff} \tag{3}$$

Table 1. The Parameters

U_D	DC pole to pole voltage
U_V	Output AC voltage
U_{CU}^{Σ}	Sum of capacitor voltages, upper multivalve
U_{CL}^{Σ}	Sum of capacitor voltages, lower multivalve
$e_V = \frac{n_L U_{CL}^{\Sigma} - n_U U_{CU}^{\Sigma}}{2}$	Inner alternating voltage
i_U	Current in the upper multivalve
i_L	Current in the lower multivalve
$i_V = i_U + i_L$	Output AC current
$i_{diff} = \frac{i_U - i_L}{2}$	Circulating current
n_U	Insertion index, upper multivalve, on interval [0,1]
n_L	Insertion index, lower multivalve, on interval [0,1]

Inserting equations (2) and (3) into equation (1) gives:

$$i_v = I_{s1} + i_{diff} + I_{s2} - i_{diff} = I_{s1} + I_{s2} \tag{4}$$

The difference between the two multivalve currents is:

$$i_U - i_L = I_{s1} + i_{diff} - (I_{s2} - i_{diff}) = I_{s1} - I_{s2} + 2i_{diff} \tag{5}$$

If the converter consists of N submodules per multivalve, and $n_m = 0$ means that all the N submodules are bypassed, while $n_m = 1$ means that all N submodules are inserted, then the available voltage in a multivalve m, i.e. sum of all the inserted capacitor voltages, is given as:

$$U_{Cm} = n_m U_{Cm}^{\Sigma} \tag{6}$$

where u_{Cm}^{Σ} is the total capacitor voltage in the multivalve and m=U,L.

The sum of the two insertion indexes should be kept equal to 1, as an insertion in one multivalve corresponds to a bypassing in the other multivalve in the phase, expressed mathematically as:

$$n_U + n_L = 1 \tag{7}$$

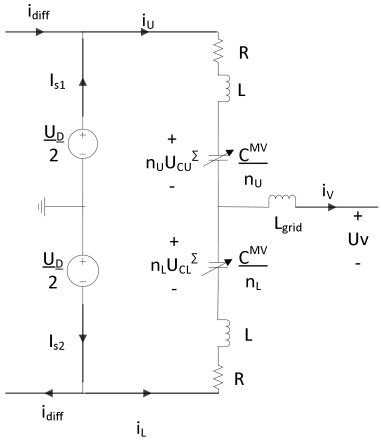

Fig. 3. Continuous Equivalent of a Phase Leg

Using Kirchhoff's voltage law in Fig. 3:

$$\frac{U_D}{2} - n_U U_{CU}^{\Sigma} - U_V - (Ri_{diff} + L\frac{\mathrm{d}i_{diff}}{\mathrm{d}t}) - L_{grid}\frac{\mathrm{d}i_V}{\mathrm{d}t} = RI_{s1} + L\frac{\mathrm{d}I_{s1}}{\mathrm{d}t} \tag{8}$$

$$-\frac{U_D}{2} + n_L U_{CL}^{\Sigma} - U_V + Ri_{diff} + L\frac{\mathrm{d}i_{diff}}{\mathrm{d}t} - L_{grid}\frac{\mathrm{d}i_V}{\mathrm{d}t} = RI_{s2} + L\frac{\mathrm{d}I_{s2}}{\mathrm{d}t} \tag{9}$$

Assuming that:

$$I_{s1} = I_{s2} \tag{10}$$

Combining this assumption with the fact that $U_V = U_V$ in equations (8) and (9) gives:

$$U_D - n_U U_{CU}^{\Sigma} - n_L U_{CL}^{\Sigma} = 2(Ri_{diff} + L\frac{\mathrm{d}i_{diff}}{\mathrm{d}t}) \tag{11}$$

In the perfectly balanced case $U_{CU}^{\Sigma} = U_{CL}^{\Sigma} = U_D$. This shows that the circulating current is a result of not perfectly balanced multivalve voltages. If the deviation from U_D is zero, the steady state value of i_{diff} will also be zero.

Using the assumption in equation (10) on equation (4) gives :

$$I_{s1} = I_{s2} = \frac{i_v}{2} \tag{12}$$

And using the assumption on equation (5) gives:

$$i_{diff} = \frac{i_U - i_L}{2} \tag{13}$$

Using that $\frac{U_D}{2} = \frac{U_D}{2}$ in equations (8) and (9) gives:

$$R(i_U + i_L) + L\frac{\mathrm{d}(i_U + i_L)}{\mathrm{d}t} + 2L_{grid}\frac{\mathrm{d}i_V}{\mathrm{d}t} + 2U_V = n_L U_{CL}^{\Sigma} - n_U U_{CU}^{\Sigma} \tag{14}$$

L' can be defined as:

$$L' = \frac{L}{2} + L_{grid} \tag{15}$$

Inserting from equation (1):

$$U_V = \frac{1}{2}(n_L U_{CL}^{\Sigma} - n_U U_{CU}^{\Sigma}) - \frac{R}{2}i_V - L'\frac{\mathrm{d}i_V}{\mathrm{d}t} \tag{16}$$

This shows that the output voltage, U_V, is only dependent on the output current, i_V, and the difference between the two multivalve voltages $n_U U_{CU}^{\Sigma}$ and $n_L U_{CL}^{\Sigma}$ [17]. The difference between $n_U U_{CU}^{\Sigma}$ and $n_L U_{CL}^{\Sigma}$ can be considered as an inner alternating voltage. This voltage will be denoted e_V:

$$e_V = \frac{1}{2}(n_L U_{CL}^{\Sigma} - n_U U_{CU}^{\Sigma}) \tag{17}$$

$$U_V = e_V - \frac{R}{2}i_V - L'\frac{\mathrm{d}i_V}{\mathrm{d}t} \tag{18}$$

Equation (16) can be rewritten in the dq reference frame and the Laplace domain as:

$$v_d = e_{Vd} - (\frac{R}{2} + sL')i_d - \omega L' i_q \tag{19}$$

$$v_q = e_{Vq} - (\frac{R}{2} + sL')i_q + \omega L' i_q \tag{20}$$

4. Simulation Model of the MMC in an EMT Simulation Program

The challenge when developing a simulation model of the MMC is the large number of switches. In simulation models of LCCs and VSCs with series connected IBGTs, only two switches per phase and bridge are needed, leading to a model with few nodes. When modelling the switching operation properly, an admittance matrix with size equal to the number of nodes in the network must be inverted every time a switch operates [9]. This requires large computational efforts when every MMC submodule consists of three nodes. At the same time, if a model is to be valid during abnormal operation, every level down to each valve must be modelled independently. Gnanarathna et al. [9] describes a model where all the levels are included, and hence it is invariably valid, but by using a Thévenin equivalent, the sizes of the admittance matrixes that need to be inverted are drastically reduced. This is made possible by dividing the solution into two parts; the valve operation and capacitor balancing control is solved separately. Each multivalve is expressed as a

specially designed Thévenin equivalent. This implementation requires reduced computational effort, but is mathematically exactly equivalent to conducting a traditional simulation.

The Thévenin equivalent is deduced using the trapezoidal integration method. V_C is the voltage across the capacitor and I_C the current through it (Fig. 2).

$$V_C(t) = \int_0^t \frac{1}{C} I_C \, dt \approx V_C(t - \Delta T) + \frac{1}{C}\left(\frac{I_C(t - \Delta T) + I_C(t)}{2}\right)\Delta T \tag{21}$$

Defining R_C and V_{CEQ}:

$$R_C = \frac{\Delta T}{2C} \tag{22}$$

$$V_{CEQ}(t - \Delta T) = \frac{\Delta T}{2C} I_C(t - \Delta T) + V_c(t - \Delta T) \tag{23}$$

Gives:

$$V_C(t) = R_C I_C(t) + V_{CEQ}(t - \Delta T) \tag{24}$$

The valves can be treated as two-state resistive devices with low resistance when switched on and high resistance in the off state. The values of resistors R_1, for valve 1, and R_2, for valve 2 in Fig. 4, depend on the switch state of the valves and are either R_{ON} or R_{OFF}.

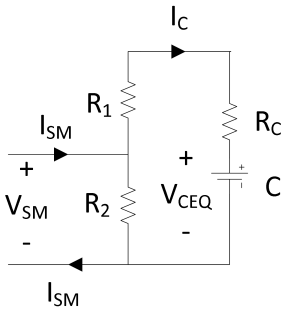

Fig. 4. Submodule Thévenin Equivalent

The Thévenin equivalent is developed using Kirchhoff's voltage law:

$$V_{SM} = I_C(R_1 + R_C) + V_{CEQ} \tag{25}$$

$$V_{SM} = R_2(I_{SM} - I_C) \tag{26}$$

Equation (26) gives:

$$I_C = \frac{R_2 I_{SM} - V_{SM}}{R_2} \tag{27}$$

Inserting equation (27) into equation (25) gives:

$$V_{SM}(t) = I_{SM}(t)\frac{R_2(R_1 + R_C)}{R_2 + R_1 + R_C} + V_{CEQ}(t - \Delta T)\frac{R_2}{R_2 + R_1 + R_C} \tag{28}$$

Defining $R_{SMEQ}(t)$ and $V_{SMEQ}(t - \Delta T)$:

$$R_{SMEQ}(t) = \frac{R_2(R_1 + R_C)}{R_2 + R_1 + R_C} \tag{29}$$

$$V_{SMEQ}(t - \Delta T) = V_{CEQ}(t - \Delta T)\frac{R_2}{R_2 + R_1 + R_C} \tag{30}$$

Insertion into equation (28) gives:

$$V_{SM}(t) = I_{SM}(t) R_{SMEQ}(t) + V_{SMEQ}(t - \Delta T) \tag{31}$$

This calculation only requires values from the last time step, the resistance values and the submodule current, which is the same current for all submodules in the multivalve. The voltage across the multivalve is given as:

$$V_{MV}(t) = \sum_{i=1}^{N} V_{SM_i}(t) = I_{MV}(t) \sum_{i=1}^{N} R_{SMEQ_i}(t) + \sum_{i=1}^{N} V_{SMEQ_i}(t - \Delta T) = I_{MV} R_{EQ} + V_{EQ}(t - \Delta T) \tag{32}$$

where N is the number of submodules in the multivalve, I_{MV} is the current through the multivalve, R_{EQ} is the equivalent multivalve resistance, and V_{EQ} is the equivalent voltage source.

The Thévenin equivalent is shown in Fig. 5 . Going into the equivalent is FP, the firing pulses, one for each valve. These are necessary for determining the value of R_1 and R_2. The capacitor voltage, V_C, for each submodule goes out of the Thévenin equivalent and is made available for the capacitor voltage balancing controller. V_C is found by combining equations (24) and (27). The firing pulses are determined based on the capacitor voltage values.

In contrast to averaged models, this model is capable of representing the exact behaviour of the converter during abnormal operation, e.g. control system failure and module failure.

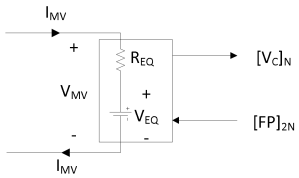

Fig. 5. The Multivalve Thévenin Equivalent

5. Control of the MMC

The control of the LCC is done by controlling the firing angles. In a DC link, one converter controls the DC voltage while the other controls the DC current. Transformer tap changers can be used to obtain the desired combination of voltage and current [7]. With VSCs it's possible to control both the delay angle and the voltage magnitude, the first influencing the active power and the latter influencing the reactive power [7]. The voltage magnitude is manipulated with the modulation index. The control of the VSC is normally done in a dq reference frame with one active power control loop and one reactive power control loop. The active power control loop can control either active power or DC voltage, while the reactive power loop can control the reactive power or the AC voltage magnitude [7]. The possibilities of the MMC control system is generally equal to those of the two-level and three-level VSCs: Both can successfully be implemented in a dq reference frame controlling two out of the four parameters mentioned above. However, as the mathematical modelling is quite different, the blocks representing the converter system will differ. In addition, the MMC will need a capacitor voltage controller, keeping the capacitor voltages as equal and as close to the reference value as possible.

The dq reference frame controllers use a cascaded structure with a fast inner current loop and an outer loop controlling active power and reactive power or the AC voltage magnitude. Equations (19) and (20) will be used to develop the controllers.

The Current Control Loops. Fig. 6 shows the d axis current control loop. It consists of a PI controller, a time delay representing the converter and a block representing the electrical system given by equation (19). From the symmetry of equations (19) and (20) it can be seen that the q axis current control loop will have the same structure and parameters and this loop is therefore not shown here. The PI controller in the control loop can be tuned using modulus optimum [18]. Using modulus optimum, the PI controller's zero should cancel the largest time constant in the system transfer function. In this case that will be the time delay in the block representing the electrical system.

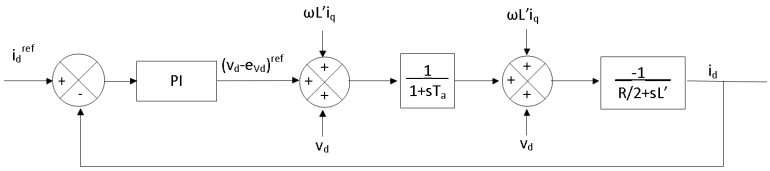

Fig. 6. The D Axis Current Control Loop

The open current loop transfer function is found by multiplying all the block transfers functions:

$$H_{c,OL} = k_c \frac{1 + T_{ic}s}{T_{ic}s} \frac{1}{1 + T_a s} \frac{-1}{\frac{R}{2} + L's} \tag{33}$$

where k_c is the gain in the PI controller, T_{ic} is the integral time constant, T_a is the converter time delay, and R and L' are the electrical system parameters.

Using modulus optimum [18] the parameters of the PI controller are determined as $k_c = \frac{-L'}{2T_a}$ and $T_{ic} = \frac{2L'}{R}$.

The Active and Reactive Power Control Loops. The active power and reactive power controllers use the dq reference frame expressions that are obtained when the grid voltage vector is defined to be aligned with the d axis. With this alignment $v_q = 0$ and active power and reactive power are given as [19]:

$$P = v_d i_d \tag{34}$$

$$Q = v_d i_q \tag{35}$$

From the similarity of these two equations, it can be seen that the active power controller and the reactive power controller will have the same structure and parameters. The reactive power control loop will contain the q axis current control loop. This loop has the same closed loop transfer function as the d axis current control loop. Due to these similarities only the active power control loop is shown here (Fig. 7). It consist of a PI controller, the d axis current control loop, and a gain given by equation (34). Tuning of the PI controller must be done to ensure a sufficiently large phase margin combined with a high crossover frequency. Plotting of the transfer function shows that the gain must be kept under a certain value and that the integral time constant, T_{iP}, must be kept a number of times higher than the time delay in the converter T_a.

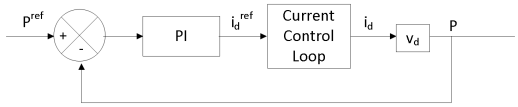

Fig. 7. The Active Power Control Loop

The AC Voltage Magnitude Control Loop. The AC voltage magnitude controller uses the relation between dq quantities and rms values given as:

$$V_{rms} = \sqrt{\frac{v_d^2 + v_q^2}{3}} \tag{36}$$

The controller in Fig. 8 consist of a PI controller, the q axis current control loop, a block representing the electrical system given by equation (20), and a function representing the relationship between dq quantities and phase quantities given by equation (36). The control loop is stable with any parameters in the PI controller.

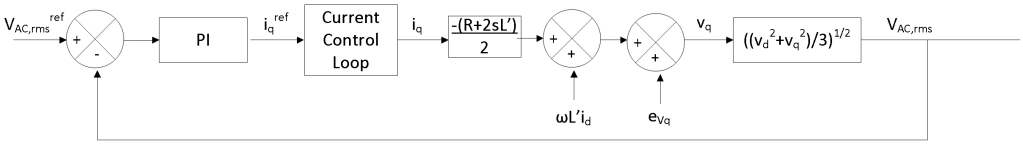

Fig. 8. The AC Voltage Magnitude Control Loop

6. Conclusion

The mathematical and computational modelling of a MMC has been presented. These enable respectively analytical evaluations and simulations, and are therefore important tools when the MMC is introduced in the power system. Due to the complexity of the MMC topology, simulation models turn out to be quite different from classical VSC models. The mathematical modelling also needs to be done differently to account for the fact that some submodules are inserted while others are bypassed. Assumptions were made to enable development of a continuous mathematical model. For the simulation model, a Thévenin equivalent was introduced to obtain a voltage value for each multivalve at every instant. This model must be combined with a capacitor voltage balancing algorithm. The Thévening equivalent is important as it reduces the computational efforts a lot, and hence makes realistic simulations possible. Regarding control, the MMC has the same advantages as two-level and three-level VSCs, d axis and q axis control can be done independently. This can be used to control either DC voltage or active power and either AC voltage magnitude or reactive power. The presented control loops use a cascaded structure with a fast inner current loop and an outer loop controlling active power and reactive power or the AC voltage magnitude. The equations resulted in similar i_d and i_q control loops. The structure and parameters of the active power and reactive power control loops also became quite similar. Tuning of the PI controllers in the current loops can be done using modulus optimum. The PI controllers in the outer control loops must be tuned to achieve a reasonable crossover frequency combined with suitable phase and gain margins. In the future, simulations should be carried out to identify the appropriateness of the controllers.

References

[1] S. Norrga, VSC HVDC - Past , Present and Future, Presentation at the 14th European Conference on Power Electronics and Applications, EPE'11 (2011).
[2] K. Friedrich, Modern HVDC PLUS Application of VSC in Modular Multilevel Converter Topology, in: IEEE International Symposium on Industrial Electronics (ISIE), 2010.
[3] S. Cole, R. Belmans, Transmission of Bulk Power: The History and Applications of Voltage-Source Converter High-Voltage Direct Current Systems, IEEE Ind. Electron. Mag (2009) 6.
[4] B. Jacobson, P. Karlsson, G. Asplund, L. Harnefors, T. Jonsson, VSC-HVDC Transmission with Cascaded Two-Level Converters, in: CIGRÉ B4-110, 2010.
[5] C. Davidson, D. Trainer, Innovative Concepts for Hybrid Multi-Level Converters for HVDC Power Transmission, in: 9th IET International Conference on AC and DC Power Transmission (ACDC 2010), 2010.
[6] Alstom Grid, Multi-Terminal HVDC System for Large Offshore Wind Park Grid Integration, http://www.alstom.com/WorkArea/DownloadAsset.aspx?id=8589941168 (2010).
[7] C. Bajracharya, Control of VSC-HVDC for Wind Power, Master's thesis, Norwegian University of Science and Technology Department of Electrical Power Engineering (2008).
[8] ABB, Differences Between HVDC Light and Classic HVDC, http://www.abb.com/industries/ap/db0003db004333/b8a81e7c435f37bac125755800373a31.aspx (November 2011).
[9] U. N. Gnanarathna, A. M. Gole, R. P. Jayasinghe, Efficient Modeling of Modular Multilevel HVDC Converters (MMC) on Electromagnetic Transient Simulation Programs, IEEE TRANSACTIONS ON POWER DELIVERY 26 (1) (2011) 316–324.
[10] A. Cross, D. Trainer, R. Crookes, Chain-Link Based HVDC Voltage Source Converter Using Current Injection, in: 9th IET International Conference on AC and DC Power Transmission (ACDC 2010), 2010, p. 5.
[11] ABB HVDC Reference Projects, Jinping - Sunan, http://www.abb.com/industries/ap/db0003db004333/545527721af2bf14c12578690049fea4.aspx (November 2011).
[12] Siemens HVDC PLUS - References. http://www.energy.siemens.com/fi/en/power-transmission/hvdc/hvdc-plus/references.htm (November 2011).
[13] A. Nabae, I. Takahashi, H. Akagi, A New Neutral-Point-Clamped PWM Inverter, IEEE TRANSACTIONS ON INDUSTRY APPLICATIONS lA-17 (5) (1981) 518–523.
[14] N. S. Choi, J. Cho, G. H. Cho, A General Circuit Topology of Multilevel Inverter, in: Proc. IEEE 22nd Power Electron. Sepc. Conf., PESC'91, 1991.
[15] A. Schiop, P. Scortaru, Simulink Model of Flying Capacitor Multilevel Inverter, in: 11th International Conference on Optimization of Electrical and Electronic Equipment, OPTIM 2008. 2008, pp. 203–208.
[16] V. Blasko, V. Kaura, A New Mathematical Model and Control of a Three-Phase AC-DC Voltage Source Converter, IEEE TRANSACTIONS ON POWER ELECTRONICS 12 (1) (1997) 116–123.
[17] A. Antonopoulos, L. Angquist, H.-P. Nee, On Dynamics and Voltage Control of the Modular Multilevel Converter, in: 13th European Conference on Power Electronics and Applications, 2009. EPE '09.
[18] J. W. Umland, M. Safiuddin, Magnitude and Symmetric Optimum Criterion for the Design of Linear Control Systems: What Is It and How Does It Compare with the Others?, IEEE TRANSACTIONS ON INDUSTRY APPLICATIONS (1990) 26 (3).
[19] J. Machowski, J. W. Bialek, J. R. Bumby, Power System Dynamics, Stability and Control, 2nd Edition, Wiley, 2008.